

Coupled Soil-Structure Interaction Effects of Symmetric and Asymmetric Buildings In Urban Regions

Submitted in partial fulfillment of the requirements for

the degree of

Doctor of Philosophy

in

Civil and Environmental Engineering

Yigit D Isbilibiroglu

B.S., Civil Engineering, Middle East Technical University

M.S., Civil and Environmental Engineering, Carnegie Mellon University

Carnegie Mellon University
Pittsburgh, PA

September, 2013

To My Wife, Duygu

Abstract

This thesis deals with the response of idealized building clusters during earthquakes, their effect on the ground motion, and how individual buildings interact with the soil and with each other. We simulate the ground motion during the 1994 Northridge earthquake and focus on the coupled response of multiple simplified symmetric and asymmetric building models located within the San Fernando Valley and the Simi Valley. We use the Domain Reduction Method (DRM) in order to perform these simulations efficiently while recurrently modifying the models without having to redo the entire simulation every time. Numerical results show that the soil-structure interaction (SSI) effects vary with the number and dynamic properties of the buildings, their separation, and the impedance with respect to the soil. These effects appear as: (i) an increased spatial variability of the ground motion; and (ii) significant reductions in the buildings' base motion at high frequencies, changes in the higher natural frequencies of the building-foundation systems and variations in the roof displacement, with respect to those of the corresponding rigid-base and single SSI models. Torsional coupling of the asymmetric structures combined with SSI effects are also investigated, and results, in comparison with the symmetric structures, are given.

Acknowledgments

I would like to show my greatest appreciation to my advisor, Professor Jacobo Bielak, for his kindness, patience, encouragement and continual help and advice. I would be always grateful to him for his academic and personal guidance. Also special thanks goes to Joyce Bielak, for all her support to my wife, Duygu, and to me.

Special acknowledgements to the members of my doctoral committee: Prof. David OHallaron, Prof. Irving Oppenheim, and Dr. Enrique Bazan. Also, I am deeply grateful to Dr. Ricardo Taborda who has helped me in every possible way. Ricardo, I do not have enough words to express my deep appreciation for supporting me, both academically and personally.

I am particularly indebted to my dear friends, Haydar Karaoglu and Dorian Restrepo. Haydar, your support from the very first day of my life in Pittsburgh has been invaluable. Also special gratitude to Batuhan Arisoy for being such a wonderful friend and being always supportive at my lowest points. I am also grateful for the continual assistance given by the CEE staff.

I would also like to thank my family for the support they provided me through my entire life. In particular, I must acknowledge my lovely wife and best friend, Duygu, not just for all her love and understanding, but also for giving me the best PhD gift ever—our cute two weeks old daughter, Asya.

Funding for this work was provided by the National Science Foundation (NSF) award: Towards Petascale Simulation of Urban Earthquake Impacts (NSF OCI-0749227). Additional support was provided by the Southern California Earthquake Center (SCEC) through NSF awards: A Petascale Cyberfacility for Physics-Based Seismic Hazard Analysis (SCEC PetaSHA3 Project) (NSF EAR-0949443); and Outward on the Spiral: Petascale Inference in Earthquake System Science (SCEC PetaShake Project) (NSF OCI-0905019). SCEC is funded by NSF Cooperative Agreement EAR-0529922 and U.S. Geological Survey Cooperative Agreement 07HQAG0008. This research was

also possible thanks to an allocation of computing resources by the XSEDE program supported by NSF. The computations were performed on Kraken at the U.S. National Institute for Computational Sciences.

Contents

1	Introduction	1
1.1	Background & Significance	2
1.1.1	Individual Soil-Structure Interaction (SSI) Effects	3
1.1.2	Site-City Interaction (SCI) Effects	6
1.1.3	Torsional Coupling Effects	7
1.2	Research Design & Methods	10
2	Earthquake Simulation Approach	12
2.1	Wave Propagation Model	12
2.1.1	Governing Equations	12
2.1.2	Numerical Discretization	13
2.2	Large-Scale 3D Earthquake Simulator: Hercules	15
2.2.1	Meshing and Stiffness Contribution	16
2.3	Domain Reduction Method (DRM)	17
2.3.1	Formulation	17
2.3.2	Implementation of the DRM into Hercules	18
3	Case Study I : Site-City Interaction Using Torsionally Uncoupled Buildings	24
3.1	Building Models	25
3.2	Earthquake and Regional Simulation	27
3.3	Subregion of Interest and Building Clusters	29

3.3.1	Softened Soil Conditions	31
3.3.2	Computational Effort and Performance	33
3.4	Results and Analysis	34
3.4.1	Regional Response	34
3.4.2	Effects of the Building Clusters on the Ground Motion	38
3.4.3	Structural Behavior of Buildings	44
4	Modeling Torsionally Coupled Buildings	64
4.1	Modified Meshing	65
4.1.1	Nonuniform Distribution of Stiffness in Plan	65
4.1.2	Nonuniform Distribution of Stiffness Along Height	65
4.1.3	Designing Eccentric Structures	66
4.2	Constrained Displacements	70
4.2.1	Most General Constrained Model	70
4.2.2	Shear Buildings	74
5	Case Study II : Site-City Interaction Using Torsionally Coupled Buildings	76
5.1	Building Models	77
5.2	Earthquake and Regional Simulation	80
5.3	Subregion of Interest and Building Clusters	81
5.3.1	Softened Soil Conditions	83
5.3.2	Computational Effort and Performance	84
5.4	Results and Analysis	84
5.4.1	Regional Response	84
5.4.2	Effects of the Building Clusters on the Ground Motion	86
5.4.3	Structural Behavior of Buildings	89
6	Conclusion	107

A	Hollywood Storage Building	116
B	Computational Effort and Performance	
	- Case I	118
C	Computational Effort and Performance	
	- Case II	120
D	Additional Figures for Case II	122

List of Figures

2.1	Schematic representation of the simulation process in Hercules.	16
2.2	Meshing procedure in Hercules.	17
2.3	Summary of two-step DRM.	19
2.4	Vertical cuts of simple simulation domains.	21
2.5	Summary figure that shows the implementation of the DRM into Hercules.	22
3.1	Region of interest in Southern California and fault plane.	28
3.2	Regional simulation domain and detail of the local sub-region.	29
3.3	Schematic representation of the the buildings cluster model.	31
3.4	Shear wave velocity (V_S) and critical damping ratio profiles.	33
3.5	Still-frames of the free-surface horizontal velocity for regional simulation.	35
3.6	Amplitude of the peak free-surface horizontal velocity for the DRM region.	36
3.7	Velocity time series and Fourier amplitudes for the DRM region.	37
3.8	Change in the peak horizontal-magnitude velocity at the free-field level.	40
3.9	Condensed representation of the change in the motion at the free-surface level.	42
3.10	Summary plot for the change in the motion at the free-surface level.	43
3.11	Components of the response of B2-ICB	46
3.12	Variation in the normalized relative roof displacement.	48
3.13	Change in the normalized relative roof displacement of the center building.	51
3.14	Average, maximum and minimum envelopes of the base transfer functions	55

3.15	Average, maximum and minimum envelopes of the roof transfer functions	56
3.16	Comparisons between the base transfer function of the ICB and the CBs.	60
3.17	Comparisons between the roof transfer function of the ICB and the CBs.	61
4.1	Parabolic shear distribution.	67
4.2	Asymmetric building model.	69
4.3	Degrees of freedom at the CM.	71
5.1	Shear building dofs.	78
5.2	Regional simulation domain and detail of the local sub-region.	82
5.3	Shear wave velocity (V_S) and critical damping ratio profiles.	84
5.4	Amplitude of the peak free-surface horizontal velocity for the building clusters location.	85
5.5	Velocity time series and Fourier amplitudes for the building clusters location. . . .	87
5.6	Change in the peak horizontal-magnitude velocity at the free-field level.	90
5.7	Variation in the normalized relative roof displacement for $\Omega = 1$	92
5.8	Variation in the normalized relative roof displacement for $\Omega = 1.3$	94
5.9	Change in the normalized relative roof displacement of the center building due to SCI effects.	96
5.10	Relative roof transfer functions of the fixed-base structures.	99
5.11	Average, maximum and minimum envelopes of the base transfer functions for B1 .	100
5.12	Average, maximum and minimum envelopes of the roof transfer functions for B1 .	101
5.13	Comparisons between the base transfer function of the ICB and the CBs for B1-S1.	103
5.14	Comparisons between the roof transfer function of the ICB and the CBs for B1. . .	104
A.1	Fourier amplitude spectra for the Hollywood Storage Building.	116
A.2	Base transfer functions obtained for the Hollywood Storage Building.	117
D.1	Average, maximum and minimum envelopes of the base transfer functions for B2 .	123

D.2	Average, maximum and minimum envelopes of the base transfer functions for B3	124
D.3	Average, maximum and minimum envelopes of the roof transfer functions for B2	125
D.4	Average, maximum and minimum envelopes of the roof transfer functions for B2	126
D.5	Comparisons between the base transfer function of the ICB and the CBs for B2-S1.	127
D.6	Comparisons between the base transfer function of the ICB and the CBs for B3-S1.	128
D.7	Comparisons between the roof transfer function of the ICB and the CBs for B2-S1.	129
D.8	Comparisons between the roof transfer function of the ICB and the CBs for B3-S1.	130

List of Tables

3.1	Dimensions, frequencies and mechanical properties of buildings.	27
3.2	Description of the different building clusters.	30
3.3	Separation considered for the different spatial distribution of building clusters. . . .	30
5.1	Dimensions, frequencies and mechanical properties of the uniform buildings. . . .	79
5.2	Fundamental translational (f_v) and torsional (f_θ) natural frequencies of each structure type for different Ω s (f_θ/f_v).	80
5.3	Description of the different building eccentricities. \bar{e} is the normalized eccentricity with respect to the radius of gyration of the cross section about the CM (r). $\Omega = f_\theta/f_v$	80
5.4	Description of the different building clusters.	82
5.5	Separation considered for the different spatial distribution of building clusters. . . .	82
B.1	Simulation performance and domain characteristics for case I.	119
C.1	Simulation performance and domain characteristics for case II.	121

CHAPTER 1

Introduction

For a structure founded on rock, the motion experienced by its foundation is practically identical to the motion that would have been recorded in the absence of the building. Any type of interaction between the structure and the soil is insignificant in this case, thus the calculation can be restricted to the structure excited by this specified ground motion. In the case of a soft site, however, two aspects of soil structure interaction arise for the same incident seismic waves from the source. First, the input motion is filtered due to the presence of a stiff foundation on a soft medium. Second, the dynamic characteristics of the flexible building-foundation system are different from the fixed-base one. In addition, inertia developed in the vibrating (flexible) system causes additional displacements of the foundation. These effects comprise the mechanisms of interaction between the structure, the foundation, and the soil, and are called soil-structure interaction (SSI) effects.

The effect of soil-structure interaction is recognized to be important and should not, in general, be neglected. In the last four decades extensive studies have been conducted on the subject of SSI. However, most of the time, these studies considered the flexible-base response of isolated single buildings. Only recently, coupled SSI effects of multiple buildings have started to receive attention. This problem of multiple interactions in dense building regions has become known as site-city interaction (SCI).

On the other hand, structures subjected to translational earthquake excitation undergo lateral as well as torsional motions if their structural plans do not have two axes of mass and/or stiffness

symmetry. Torsional motions can also occur in buildings with structural plans that have two axes of mass and stiffness symmetry if the ground shaking includes a torsional component. As a result of this coupling of lateral and torsional motions, the response of an asymmetric structure would differ from a symmetric structure that has the same uncoupled translational stiffness.

1.1 Background & Significance

During an earthquake, the level of damage done to a structure supported on the soil surface depends mainly on (i) the amplitude, frequency content and duration of shaking, and (ii) the dynamic characteristics of the building-foundation system. From a regional perspective, ground motion characteristics are influenced by the source, path, directivity and basin effects; on the other hand, local site conditions may also have a profound influence for a specific site. These local effects include, but are not limited to, the properties of the overlying soil layers, topography of the region, individual soil-structure interaction (SSI) and collective site-city interaction (SCI) effects. Among these factors, in this study we focus on the SSI and SCI effects, which become more prominent especially in dense urban settings. Apart from playing an active role in modifying the ground motion characteristics, SSI also affects the dynamic characteristics of the building-foundation system. These effects of SSI have been well documented over the last four decades (e.g. [Jennings and Bielak, 1973](#); [Veletsos and Meek, 1974](#)). Today, SSI is believed to be a mature field with a well established theory especially when studying the structures in isolation (without the presence of neighboring structures) and with the assumption of linearity ([Kausel, 2007](#)). On the other hand, the interest on the multiple interactions between the soil and the structures of an urban environment has risen just recently. A little less than two decades ago, [Wirgin and Bard \(1996\)](#) came up with the idea that the presence of the buildings (especially high-rise) whose fundamental frequencies coincide with the frequency of the underlain clay layer, might explain the beats and the long duration in the signals observed in Mexico City during the Michoacan earthquake in 1985. Since then, global interaction between all the buildings in a densely urbanized city and the subsoil has been

investigated with a growing interest especially by means of numerical methods (Lou et al., 2011). A review of the related works is given in the following paragraphs.

1.1.1 Individual Soil-Structure Interaction (SSI) Effects

Soil-structure interaction (SSI) effects are important in earthquake engineering analysis and design because they can significantly reduce—and in some cases increase—the structural response. These effects are due, primarily, to the flexibility added by the soil, the scattering of incident waves by the foundation, and the inertia of the structure, which also generates waves that radiate back into the soil.

The study of SSI dates back to the 1950s. Merritt and Housner (1954) showed that the fundamental period of typical buildings could increase by up to about 10 percent with respect to that of the corresponding fixed-base models because of SSI-related rocking effects. Housner (1957) also noted that low and stiff buildings on very soft ground could benefit from having large base dimensions, as long as their foundations were sufficiently stiff.

The dynamics of SSI were studied extensively in the 1970s by means of analytical models. Luco (1969) provided solutions to the problem of infinitely long elastic shear wall founded on a semicircular rigid foundation underlain by a half-space for a two dimensional SH-type vibration. He found that the displacement of the foundation is zero for the fixed-base natural frequencies of the shear wall. This dynamic absorber effect was also observed by Bielak (1971) when he showed that this effect holds true at a frequency in which the system that can translate but is constrained against rotation. Jennings and Bielak (1973) obtained simplified approximate formulas for modified period and damping ratio of the structure founded on an elastic half-space by assuming that interaction system possesses $n+2$ significant resonant frequencies. These results were confirmed later by the findings of Veletsos and Meek (1974). They both suggested that the principal effect of interaction is to reduce the fundamental frequency of the structure but, SSI does not always yield conservative results especially if the fixed-base structure has damping. In the following year, Bielak (1975) studied the interaction problem by taking into account the embedding of the foun-

dation and concluded that the natural frequency and damping in the soil-structure system increase with embedding.

At the same time, SSI effects were studied also via large-scale tests, numerical models, observations and analysis of strong motion records (Trifunac et al., 2001). Both aspects associated with the SSI, namely, (i) the changes in the dynamic characteristics of buildings and (ii) the modified ground motion due to scattering of incident waves from the foundation and the wave field radiated back into the half-space, were examined in detail. In the following two paragraphs, we will review some of the related studies done on these two aspects, respectively.

The effects on the dynamic properties are mainly assessed by means of base and roof transfer functions and, rocking and relative translation of the base. Crouse and Jennings (1975) investigated the role of SSI during the San Fernando earthquake of 1971 using the accelerograms obtained at the Hollywood Storage Building and, reported that the base transfer functions with respect to the parking lot decay rapidly around 5 Hz for the long, EW direction, whereas the decay is more gradual for the shorter NS direction of the building. Luco et al. (1988) analyzed the SSI effects of the nine-story reinforced concrete Millikan Library Building at the Caltech campus by a forced vibration test. They determined that the fixed-base natural frequencies and modal damping ratios of the superstructure were significantly different from the corresponding values of the flexible-base system. It is also reported that translation and rocking of the base accounts for more than 30 percent of the total roof response. Bard (1988) investigated the rocking motion of four buildings, 4 to 10 stories high and located at the south of the San Francisco Bay, recorded during two different earthquakes. He found that for the stiffer 3 buildings, on average, the measured rocking motion represents 25 to 50 percent of the total transverse motion of the roof relative to the base. Using a mathematical model of the Los Angeles Warehouse Building including the foundation and the soil, Fenves and Serino (1990) concluded that the base shear for the building was 17 percent less than the base shear force calculated by neglecting the effects of interaction. Stewart et al. (1999) performed system identification analyses for 57 building sites using 77 strong motion data sets, and evaluated model vibration periods and damping ratios for both flexible and fixed cases. They

listed several factors that can significantly affect SSI, with the ratio of structure-to-soil stiffness being the most influential one. They also indicated that the ratio of the flexible-base period to the fixed-base one could reach up to 4 for a very stiff structure resting on very soft soil.

Modifications on the ground motion due to building vibration have been studied via different methods over the years. During the vibration tests of the nine-story Millikan Library Building, [Jennings and Kuroiwa \(1968\)](#) showed that it is possible to excite measurable ground motion at appreciable distances from the structure. To confirm this, [Jennings \(1970\)](#) conducted another experiment by exciting the same building into resonance via vibration generators, and found that the building-induced motion was measured at distances up to 10.7 km from the building site. [Kanamori et al. \(1991\)](#) showed that shock waves generated by the space shuttle Columbia on its re-entry, after interacting with the high-rise buildings in Los Angeles, excited ground motions that are recorded at the seismic stations in southern California. Later, [Wirgin and Bard \(1996\)](#) emulated the Mexico City urban environment by numerically solving the wave propagation problem of a periodic assembly of parallel, cylindrical blocks with rectangular cross sections underlain by a layered half-space. They found that the effects of SSI are significant up to distances of at least 1 km. [Gueguen et al. \(2000a\)](#) performed a pull-out test (POT) on a five-story RC structure at a one-third scale, resting on the surface square footing at the Volvi test site. Results showed that ground motion due to building vibration corresponds to 25–5 percent of the base motion vibration at distances 2–10 times the building base size, respectively.

In order to compare them qualitatively with our results later, multiple figures from ([Trifunac et al., 2001](#)) are included in Appendix A. They show the transfer functions and the Fourier amplitude spectra obtained from the Hollywood Storage Building during various earthquakes.

After the early experimental evidence on building-induced ground motion, it became natural to infer that two or more structures might interact with each other through the soil. Such structure-soil-structure interaction (SSSI) effects were first considered analytically by [Luco and Contesse \(1973\)](#), followed by [Wong and Trifunac \(1975\)](#). These studies examined the anti-plane response of multiple shear walls on rigid foundations of semi-circular cross section under incident SH waves

on a half-space. Their results suggested that large, rigid, and sufficiently close buildings could have significant effects on the ground motion and interact with each other at frequencies near their fundamental natural frequency. Various aspects of SSSI have been reviewed recently by [Lou et al. \(2011\)](#). Some of these are shown below.

1.1.2 Site-City Interaction (SCI) Effects

We are interested in the coupled SSI and SSSI effects of building clusters in dense urban areas during earthquake ground shaking. This problem has become known as site-city interaction (SCI), a term first introduced by [Gueguen et al. \(2000b\)](#). In the last two decades, SCI effects have received increased attention. After the pioneering work of [Wirgin and Bard \(1996\)](#), [Clouteau and Aubry \(2001\)](#) solved the interaction problem between a large number of buildings distributed on a layered half-space using a 3D numerical model. They found that the interaction has a small damping effect on the response and, observed that ground motion, when site-city resonance is reached, has double peaks in the frequency domain such as those that have been observed during the Michoacan earthquake. Rocking motion was neglected in their model. This double peak behavior in the frequency domain was also observed by [Boutin and Roussillon \(2004\)](#).

[Gueguen et al. \(2002\)](#) developed a 2D analytical model to estimate the modifications on the seismic motion due to the presence of buildings in the urban environment of Mexico City. Even though they did not take into account the soil-structure kinematic effects and multi-interaction effects between buildings, they obtained similar results with the real recordings of the ground motion during the Michoacan earthquake, by superposing the free-field motion with the contribution from all the buildings, but each one considered as isolated. With this simple model, they showed that the intensity of the motion radiated into the soil from the buildings is of the same order as the intensity of the input motion.

Using the finite element method, [Tsogka and Wirgin \(2003\)](#) simulated an idealized 2D city, which consists of ten homogenized blocks in a non-periodic and non-homogenized city-setting, resting on a soft layer. They found that the presence of the buildings leads to quasi-Love waves,

which in turn increase the shaking duration and the amplitude. Later, [Groby et al. \(2005\)](#) improved the model used in [Tsogka and Wirgin \(2003\)](#) by considering that the buildings and the soil are composed of dissipative media. They concluded that dissipation does not necessarily eliminate the anomalous effects that were found in the initial study. They reported also that reducing the spacing between buildings increases the interactions.

[Kham et al. \(2006\)](#) computed the response of 2D site-city models to a vertically incident plane SH Ricker wavelet using the boundary element method. By conducting a parametric study considering the basin thickness and the city configuration, they found that the multiple interactions are effective when the site-city resonance occurs, leading to a significant reduction of ground motion in the city and an increase outside the city. Their results showed that the roof motion of a building inside the city is reduced with respect to the single-building case. In the case of an irregular city, they suggested that the spatial variability in the ground motion increases due to the presence of different building types and their non-periodical arrangement. [Semblat et al. \(2008\)](#), by using a 2D basin profile instead of a 1D one previously proposed by [Kham et al. \(2006\)](#), further examined the SCI effects.

1.1.3 Torsional Coupling Effects

It is well known that asymmetric and symmetric buildings behave differently during earthquakes ([Newmark, 1969](#)). If a structure is asymmetric in plan and/or has an uneven distribution of either mass or stiffness, a lateral seismic load can cause a response in which the torsional and lateral motions of the structure are coupled, since the center of mass and the center of rigidity do not coincide in such buildings. Torsion can also arise in symmetric buildings due to the rotational components in the ground motion. For example, [Luco \(1976\)](#) reported that the surface waves contribute to the occurrence of such rotational motions by generating phase differences between the free-field motion at different points. All these factors, acting individually or together, may lead to a larger building response than the symmetric case, resulting in severe structural damage. Indeed, [Rosenblueth and Meli \(1986\)](#), in a report on the Mexico earthquake of September 1985, indicated

that almost 50 percent of the collapses could be directly or indirectly attributed to asymmetry in the structures. Another interesting example is reported by [Tezcan and Alhan \(2001\)](#) for a building which had been moderately damaged during the Izmit Earthquake (Turkey, August 17, 1999) and was repaired only at one corner due to financial problems. Two months after its strengthening, the structure was subjected to the Duzce Earthquake (Turkey, November 12, 1999). The structure was severely damaged this time, as a result of the torsional irregularity created by the partial strengthening of the structure.

There has been a substantial amount of research undertaken to understand the behavior of the torsionally coupled buildings—usually with the fixed-base assumption—during earthquakes. In the early years, [Ayre \(1938, 1943\)](#) investigated the torsional coupling effects of a structure that consists of a single, rigid mass, free to move only in a horizontal plane, and connected with the ground by perfectly elastic restraints. He noted that mode shapes could be composed of both translational and rotational components if the centers of mass and rigidity are not coincident. Later, [Housner and Outinen \(1958\)](#) showed that the static analysis of asymmetric structures is inadequate in the sense that it yields smaller stresses in the flexible wall than the stresses that would have been obtained by the dynamic analysis. At the time, it had been evident that strong coupling is likely to happen with large eccentricities, but several studies in the following years showed that coupling effects also occur for small eccentricities when the corresponding uncoupled natural frequencies are close to each other (e.g. [Shepherd and Donald, 1967](#); [Hoerner, 1971](#); [Kuo, 1974](#); [Kan and Chopra, 1977](#); [Tso and Dempsey, 1980](#)), which is due to the beating phenomenon developed in such situations. Some of these studies investigated coupling effects using structures that are shear-beam type, or extension of them in 3D (e.g. [Hoerner, 1971](#); [Kuo, 1974](#); [Tso and Dempsey, 1980](#)). Others used the results of vibrations tests of actual buildings (e.g. [Bouwkamp and Blohm, 1966](#); [Hoerner, 1971](#)). In order to investigate the influence of the beam-to-column stiffness ratio on the response of torsionally coupled buildings, frame buildings were also studied instead of shear beam idealizations (e.g. [Hejal and Chopra, 1989](#)).

Only a few researchers considered simultaneously SSI and torsional coupling effects in the

dynamic analysis for building structures. [Balendra et al. \(1982\)](#) used approximate frequency independent spring and dashpot coefficients associated with translational, rocking and torsional modes of vibration of torsionally coupled buildings. [Tsienias and Hutchinson \(1984\)](#), by investigating the torsional coupling effects of single-story buildings excited by translational ground motion on flexible foundations, concluded that flexibility of the foundation medium does not alter too much the coupling of lateral and torsional response of the buildings for the representative range of values of the controlling parameters. [Chandler and Hutchinson \(1987\)](#) performed a study on the effect of SSI on asymmetric buildings subjected to a series of historical free-field earthquake base motions and showed that for particular classes of actual buildings the equivalent rigid-base responses are significantly increased for structures founded on medium-stiff soils. Later, [Sivakumaran et al. \(1992\)](#) developed a method of analysis to determine the seismic responses of 3D asymmetric building-foundation systems and indicated that the soft soil conditions do influence the response of asymmetric buildings and lateral deflections are increased with eccentricity. [Bazan et al. \(1998\)](#) performed a parametric study to assess the effects of the foundation impedance, building eccentricity, and excitation characteristics on the seismic response of elastic building-foundation systems. Their results indicated that ignoring SSI in the seismic analysis of torsionally eccentric structures oftentimes is not conservative. In the last decade, [Wu et al. \(2001\)](#) incorporated the frequency-dependent foundation impedance functions in the frequency domain and applied modal analysis to combine SSI and torsional coupling effects on asymmetric buildings. Besides their other noteworthy results, they concluded that SSI effects can enlarge the translational response if the structure is slender and the two resonant frequencies are very close. Finally, [Shakib and Fuladgar \(2004\)](#) solved the 3D dynamic SSI problem of asymmetric buildings in the time domain. They found that SSI effects reduce the lateral and torsional displacements of asymmetric systems and the eccentricity ratio has a significant effect on the response. However, to our knowledge, there has not been any attempt to consider torsional coupling effect of structures along with the combined action of SSI and SCI effects, which is investigated in detail in this thesis.

Although not examined in the thesis, there are other factors that affect the torsional coupling

of buildings such as nonlinearity of the eccentric structures, which has been studied by researchers over the years (e.g. [Sadek and Tso, 1989](#); [De Llera and Chopra, 1995](#); [Chandler and Duan, 1991](#)).

1.2 Research Design & Methods

Earlier studies have shown that SCI effects are mainly influenced, among other factors, by the separation and size of the structures, their stiffness relative to that of the soil, the characteristics of their foundations, and the angle of incidence of the incoming waves. Most of these studies, however, have been limited to 2D analyses or restricted to include only some aspects of the simultaneous action of multiple soil-structure systems. In most previous studies, the underlying soil has been considered as either a halfspace, a single layer on a halfspace, or an idealized (trapezoidal) basin on a halfspace. Such representations have been used to model situations like that of the lakebed region in Mexico City, in which the soil deposits exhibit a distinct dominant fundamental resonant frequency that is clearly separated from higher resonant frequencies. There are other highly seismic regions, however, such as the Greater Los Angeles Basin and San Fernando Valley, which consists of highly heterogeneous soils that do not possess a clear dominant fundamental resonant frequency. In the present study, we are interested in examining the site-city effects for this situation. The earthquake ground motion in such regions tends to be more complex and richer in frequency content than the nearly monochromatic motion observed in regions with a simple geotechnical structure. Thus, analysis techniques that are appropriate for simpler systems (e.g. [Kham et al., 2006](#)), for which the fundamental resonant frequency of the soil structure is an important parameter, are not necessarily applicable to a medium with highly heterogeneous crustal properties.

To our knowledge, there are only a few studies that have addressed SCI effects using 3D models ([Clouteau and Aubry, 2001](#); [Lombaert and Clouteau, 2006, 2009](#); [Fernandez-Ares and Bielak, 2004](#); [Taborda and Bielak, 2011b,a](#)). [Clouteau and Aubry \(2001\)](#); [Lombaert and Clouteau \(2006, 2009\)](#), for instance, considered numerical and analytical solutions of uniformly and randomly distributed simplified building models on rigid surface foundations subjected to vertically incident

waves in a layered halfspace. These studies did not consider rocking or embedment of the foundation, and thus neglected the kinematic interaction between the foundation and the incident wavefield. [Fernandez-Ares and Bielak \(2004\)](#); [Taborda and Bielak \(2011b,a\)](#), on the other hand, considered 3D models that synthesized the earthquake source and the ground response of idealized and realistic basins with the presence of idealized building models in city- and downtown-like arrangements. In these latter studies, the building models had embedded foundations that could translate and rock, and thus the systems accounted for the complete kinematic and inertial interaction effects present under oblique and surface incident waves.

In this study, we conduct parametric studies to advance recent efforts by [Taborda \(2010\)](#) and [Taborda and Bielak \(2011a,b\)](#) for improving our understanding of the effects and dynamics of large building inventories during earthquakes through a series of 3D numerical simulations that synthesize the earthquake source and the coupled response of idealized building clusters. In order to address the multi-resolution problem that arises from the inclusion of the earthquake source at a regional scale and the building models at a local scale, and to be able to vary the system configuration during repeated simulations, I implement the Domain Reduction Method (DRM) introduced by [Bielak et al. \(2003\)](#). Simulations are performed using a parallel finite element computer code for simulating anelastic wave propagation through heterogeneous media.

As for the building models, first symmetric structures are investigated in detail. After this reference case is analysed, nonsymmetric structures, including torsion, are modeled and used in the simulations. However, different from the initial study, a particular emphasis is placed on understanding the torsional coupling effects along with the SCI effects in the second case study.

The main goals of this research can be summarized as follows: (i) to estimate the individual SSI and coupled SCI effects on the ground motion and on the structural response, and to reveal the main governing parameters; and (ii) to investigate torsionally coupled buildings under the action of these effects.

CHAPTER 2

Earthquake Simulation Approach

We conduct a series of numerical simulations that synthesize the earthquake source and the coupled response of idealized building clusters. In order to address the multi-resolution problem that arises from the inclusion of the earthquake source at a regional scale and the building models at a local scale, and to be able to vary the system configuration during repeated simulations, we implement the Domain Reduction Method (DRM) introduced by [Bielak et al. \(2003\)](#). Simulations are performed using Hercules, a parallel finite element computer code developed at Carnegie Mellon University ([Tu et al., 2006](#); [Taborda, 2010](#)), for modeling anelastic wave propagation through heterogeneous media.

2.1 Wave Propagation Model

2.1.1 Governing Equations

A deterministic earthquake ground motion simulation entails the solution of a wave propagation problem. Under the assumption of small displacements, and for a linear, isotropic, elastic medium, this problem is governed by Navier's equations of elastodynamics, which are customarily extended

to include the effects of intrinsic attenuation.

$$\nabla \cdot [\mu (\nabla \mathbf{u} + \nabla \mathbf{u}^T) + \lambda (\nabla \cdot \mathbf{u}) \mathbf{I}] + \mathbf{f} = \rho \frac{\partial \mathbf{u}^2}{\partial t^2} \quad (2.1)$$

In equation (2.1) \mathbf{u} is the displacement vector field, \mathbf{f} is the body force, ρ is the density, and λ and μ are the Lamé or elastic material constants. The shear (V_S) and dilatational (V_P) wave velocities may be expressed in terms of the Lamé constants, or the elasticity modulus E and Poissons Ratio v as follows in equation (2.2).

$$V_P = \sqrt{\frac{\lambda + 2\mu}{\rho}} = \sqrt{\frac{E(1-v)}{\rho(1+v)(1-2v)}} \quad V_S = \sqrt{\frac{\mu}{\rho}} = \sqrt{\frac{E}{2\rho(1+v)}} \quad (2.2)$$

2.1.2 Numerical Discretization

We apply standard Galerkin finite element approximation in space to the appropriate weak form of equation (2.1) in order to obtain the following system of ordinary differential equations (2.2).

$$\mathbf{M}\ddot{\mathbf{u}} + \mathbf{K}\mathbf{u} = \mathbf{f} \quad (2.3)$$

In equation (2.2), \mathbf{M} is the mass matrix, \mathbf{K} is the stiffness matrix, \mathbf{u} is the displacement vector field and \mathbf{f} is the force vector. Terms related to the boundary conditions are omitted, for brevity. Matrices are rank 3 blocks. The (i, j)th element of \mathbf{M} and \mathbf{K} are given by equations (2.4) and (2.5) respectively, where ϕ_i is the finite element global basis function associated with the i-th mode, and Ω is the volume domain. \mathbf{f} is the assembled vector of body forces given by equation (2.6), which represents the earthquake source.

$$\mathbf{M}_{ij} = \int_{\Omega} \rho \phi_i \phi_j d\Omega \quad (2.4)$$

$$\mathbf{K}_{ij} = \int_{\Omega} (\mu + \lambda) \nabla \phi_i \nabla \phi_j^T d\Omega + \int_{\Omega} \mu \nabla \phi_i^T \nabla \phi_j \mathbf{I} d\Omega \quad (2.5)$$

$$\mathbf{f} = \int_{\Omega} f \phi_i d\Omega \quad (2.6)$$

Soil and rock elements can be modeled with elastic viscous damping. One way of introducing damping is the Rayleigh formulation which is added to (2.3) in equation (2.7). For each element, damping is expressed as a linear combination of mass and stiffness matrices, as in equation (2.8), where α and β are scalar constants and the superscript e indicates an element matrix.

$$M\ddot{\mathbf{u}} + C\dot{\mathbf{u}} + K\mathbf{u} = \mathbf{f} \quad (2.7)$$

$$C^e = \alpha M^e + \beta K^e \quad (2.8)$$

Given appropriate initial conditions, the system described by equation (2.7) is integrated in time by using central differences to yield the explicit method equation (2.9). Here, Δt is the time step, and \mathbf{u}_n represents the displacement vector at the n -th time step, where $t = n\Delta t$. A lumped mass approximation is used, which is equivalent to integrating with evaluation points at the element vertices, resulting in a diagonal mass matrix. Using the lumped mass approximation, and equation (2.8), equation (2.10) is obtained, which gives the forward solution of the displacement field at each node i in the mesh. In (2.10), m^i is the mass and f^i is the nodal force corresponding to the i -th node. K^e and \mathbf{u}^e are the local stiffness matrix and displacement vector of all elements associated with node i .

$$M \left(\frac{\mathbf{u}_{n-1} - 2\mathbf{u}_n + \mathbf{u}_{n+1}}{\Delta t^2} \right) + C \left(\frac{\mathbf{u}_n - \mathbf{u}_{i-n}}{\Delta t} \right) + K\mathbf{u}_n = \mathbf{f}_n \quad (2.9)$$

$$\begin{aligned} u_{n+1}^i = & \frac{\Delta t^2}{m^i} f_n^i + (2u_n^i - u_{n-1}^i) - \alpha \Delta t (u_n^i - u_{n-1}^i) \\ & + \frac{\Delta t}{m^i} \beta \left(\sum_e K^e (\mathbf{u}_n^e - \mathbf{u}_{n-1}^e) \right)_i - \frac{\Delta t^2}{m^i} \left(\sum_e K^e \mathbf{u}_n^e \right)_i \end{aligned} \quad (2.10)$$

Equation (2.10) is used in our simulation engine, Hercules, in order to solve the wave propagation problem.

2.2 Large-Scale 3D Earthquake Simulator: Hercules

The resulting problem of anelastic wave propagation in heterogeneous media can be solved numerically using different methods. For the case of earthquake simulations at regional scales, approaches that use finite differences and low- or high-order finite element (FE) techniques have been particularly successful in the last two decades (e.g. [Frankel and Vidale, 1992](#); [Graves, 1996](#); [Bao et al., 1998](#); [Olsen et al., 2009](#); [Bielak et al., 2010](#)). Here, we use a FE approach and solve the resulting semi-discretized system explicitly in the time domain using Hercules, the parallel-computing code for earthquake simulations developed by the Quake Group at Carnegie Mellon University ([Tu et al., 2006](#); [Taborda, 2010](#)). Hercules uses tri-linear elements and relies on an octree-based approach for automatic and efficient mesh generation and memory management. It has a quadratic convergence rate for displacements, in both time and space. Material damping can be modeled by means of a viscoelastic model that uses a combination of Maxwell and Voigt elements ([Bielak et al., 2011](#)), which is capable of modeling a constant Q behavior in the time domain or more simply, by Rayleigh damping. The code uses a plane-wave approximation of the absorbing boundary condition to limit the occurrence of spurious wave reflections at the boundaries of the computational domain ([Lysmer et al., 1969](#)), and double-couple equivalent forces to represent the source. Hercules has been used in multiple simulations, including verification and validation studies (e.g. [Bielak et al., 2010](#); [Taborda and Bielak, 2013](#)), which have found it to be a sufficiently robust and reliable tool for ground motion modeling.

Hercules provides an end-to-end approach in which all simulation components—meshing, partitioning, solver, and visualization—are executed in parallel with shared data structures and no intermediate I/O. Figure 2.1 shows the schematic representation of the simulation process in Hercules.

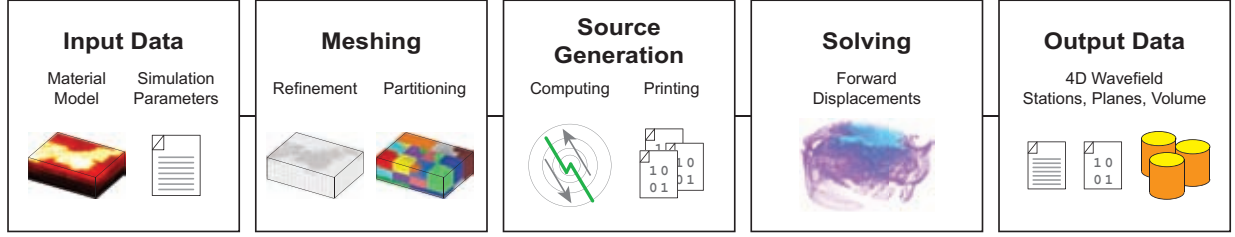


Figure 2.1: Schematic representation of the simulation process in Hercules (after [Taborda, 2010](#)).

2.2.1 Meshing and Stiffness Contribution

Octrees have been used as a basis for finite element approximation, particularly since they can be adapted to the wavelengths of propagating seismic waves while maintaining a regular shape of finite elements. A refinement criteria recursively subdivides the hexahedra into 8 elements. In our case, this criterion reads as seen in equation (2.11).

$$h_{max} \leq \frac{V_S}{pf_{max}} \quad (2.11)$$

In equation (2.11), p is the number of nodes per wavelength, V_S is the shear velocity in (m/s), and f_{max} is the maximum frequency of interest. The process of meshing in Hercules consists in 5 different steps, namely NEWTREE, REFINETREE, BALANCETREE, PARTITIONTREE and EXTRACTMESH. This process of generating an octree-based hexahedral mesh is shown in Figure 2.2 . First, NEWTREE generates a shallow octree common to all processors. Besides, each processor is made responsible only for a small area of the domain. Then, local tree in each processor is expanded by REFINETREE using the refinement criterion explained above. This results in many separate subtrees distributed among the processors. BALANCETREE enforces the 2-to-1 constraint on the parallel octree, which makes sure that the element size does not differ by more than a factor of two across neighboring elements. PARTITIONTREE redistributes the leaf octants evenly among the processors. Finally and most importantly, EXTRACTMESH creates the node and element tables and derives various associations between elements and nodes.

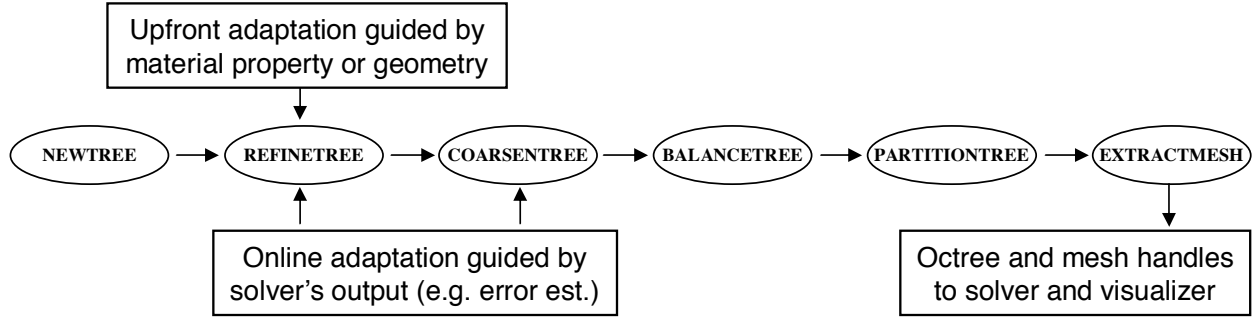


Figure 2.2: Meshing procedure in Hercules (after [Tu et al., 2006](#)).

Since a lumped mass matrix assumption is used while obtaining (2.10), we say the system is uncoupled with respect to M . This allows us to calculate the stiffness contribution of each element individually. We refer to this strategy as the `ConventionalMethod`. In addition to this, Hercules is modified to perform the stiffness contributions computations in a more efficient manner. Details related to this `EfficientMethod`, and also to `ConventionalMethod`, can be found in [Taborda \(2010\)](#); [Taborda et al. \(2010\)](#).

2.3 Domain Reduction Method (DRM)

We perform SCI simulations using a two-step approach that incorporates the DRM. This method was introduced by [Bielak et al. \(2003\)](#) and has been used successfully in earthquake simulations and other related applications (e.g. [Yoshimura et al., 2003](#); [Fernandez-Ares and Bielak, 2004](#); [Jeremic et al., 2009](#)). The DRM is particularly useful in this study because it enables one to address efficiently the multi-resolution problem of combining the regional scale simulation with multiple building arrangements at the local scale.

2.3.1 Formulation

Figure 2.3 shows and summarizes the steps of the DRM. In Step I of the DRM, the earthquake source, propagation path, and site effects are simulated in a model that includes the source

and the background crustal structure without the building models present. Here, the displacement field over a layer boundary is stored for later use as input for the following phase. In Step II, one solves the problem in the interior region—including the building models—but uses a set of equivalent effective forces defined in terms of the free-field motion stored during Step I, as input. These effective forces are applied to the element nodes of the interface and are calculated as follows.

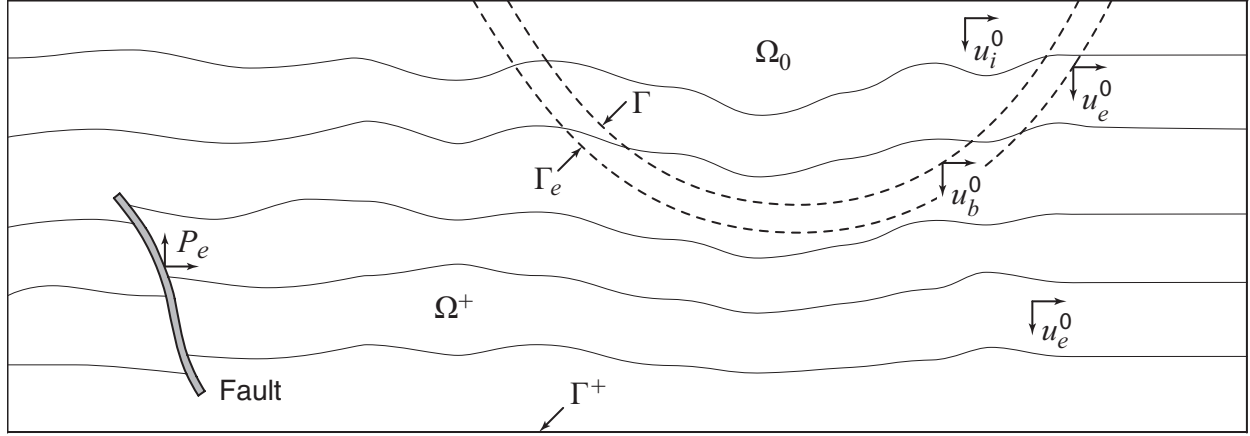
$$P^{\text{eff}} = \begin{Bmatrix} 0 \\ -M_{be}^{\Omega^+} \ddot{u}_e^0 - K_{be}^{\Omega^+} u_e^0 \\ M_{eb}^{\Omega^+} \ddot{u}_b^0 - K_{eb}^{\Omega^+} u_b^0 \end{Bmatrix} \quad (2.12)$$

The sub-matrices $M_{be}^{\Omega^+}$, $M_{eb}^{\Omega^+}$, $K_{be}^{\Omega^+}$ and $K_{eb}^{\Omega^+}$ correspond to the finite elements within the boundary, b , and exterior, e , surfaces, according to their respective subindexes. These matrices are such that they vanish everywhere, except in the single layer in the interface. This enables us to reduce the domain size in the second step.

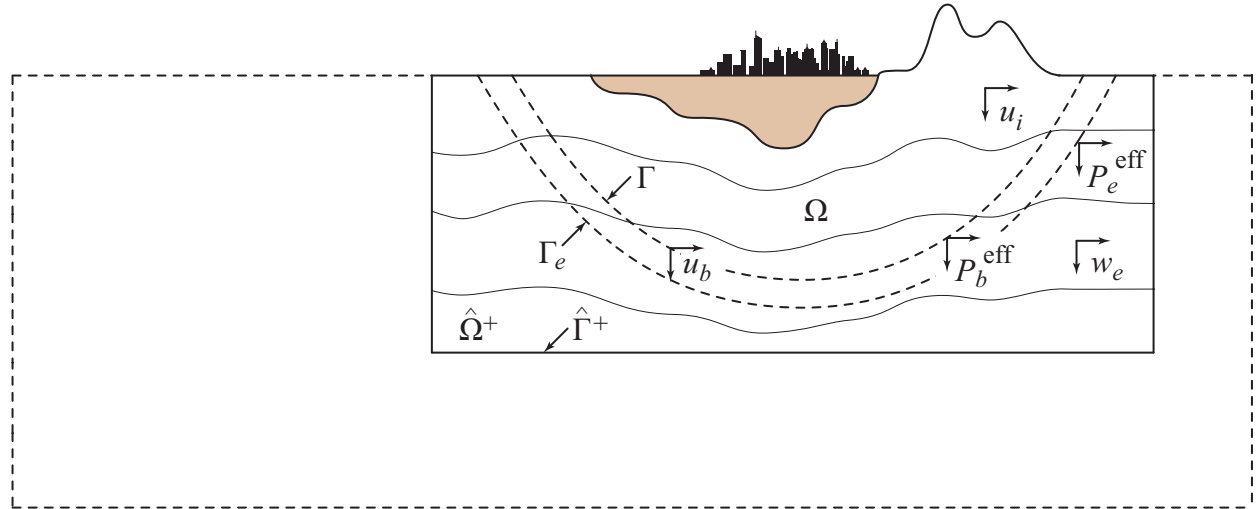
The main advantage of the DRM is that it reduces the computational demand in both Step I, by not including the building models, which would require a much finer mesh, and in Step II, by reducing the domain size considerably while also allowing one to vary the local conditions. In particular, in Step II, we change the model parameters several times without the need for repeating the larger (Step I) simulation.

2.3.2 Implementation of the DRM into Hercules

I have implemented the DRM into Hercules for this study. The implementation consists of three different parts namely, part0, part1 and part2, all of which need to be executed separately. part0 is designed as a preliminary step, which focuses on the interior region without building models.



(a) Step I



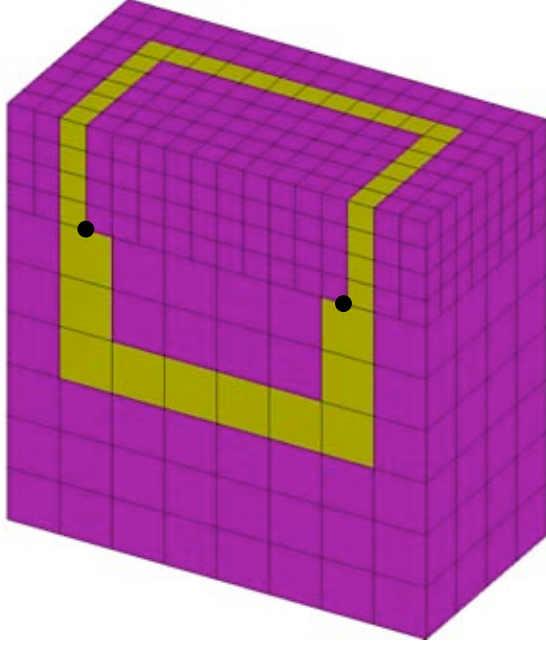
(b) Step II

Figure 2.3: Summary of two-step DRM. (a) Step I defines the auxiliary problem over background geological model. Resulting nodal displacements within Γ , Γ_e , and the region between them are used to evaluate effective seismic forces P^{eff} required for step II. (b) Step II, defined over reduced region made up of Ω and $\hat{\Omega}^+$ (a truncated portion of Ω^+). The effective seismic forces P^{eff} are applied within Γ and Γ_e . The unknowns are the total displacement fields u_i in Ω and u_b on Γ , and the residual displacements w_e in $\hat{\Omega}^+$ (after Bielak et al., 2003).

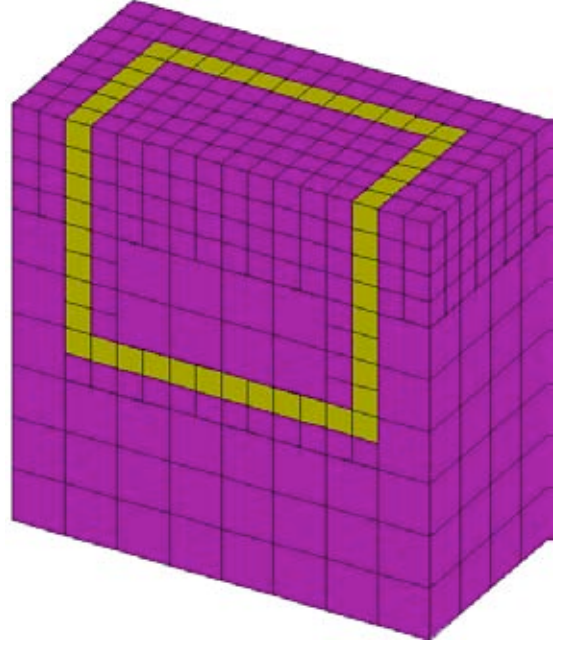
Here, the DRM boundary is defined and coordinates of the DRM nodes are stored for later use in part1. For these purposes, part0 only needs to execute the meshing routines and can be terminated before the solver starts. This makes this part by far the least time-consuming of the three. Indeed, part0 can be run several times in order to determine the DRM boundary, with almost negligible total run times.

part1 corresponds to the Step I of the DRM. In part1, a large-scale simulation which includes the source and the background crustal structure without the building models is performed. During this simulation, the calculated displacements at the coordinates of the DRM nodes—the coordinates have been determined in part0 and are taken as input here—are stored at each time step. part1 is the most time-consuming part of the three but needs to be run only once.

In part2, the problem in the interior region—including the building models—is solved. This corresponds to the Step II of the DRM. Here, the displacements stored in part1 are read as input and then converted to a set of equivalent effective forces as seen in (2.12). part2 can be repeated multiple times by changing buildings' configurations. The total service units allocated to run a single part2 simulation is just a small fraction of the part1's, which comes as no surprise and makes the DRM very useful in this study. In all the three parts, the DRM related data is stored in memory using hash tables with linked lists. During this implementation, I have faced two issues which are worth mentioning here. They are explained in the following paragraphs.



DRM layer with the presence of dangling nodes



DRM layer without dangling nodes

Figure 2.4: Vertical cuts of simple simulation domains that illustrates the two cases of the DRM layer: with (left) and without (right) the dangling nodes. Black dots show the location of dangling nodes in the figure on the left. Elements in the DRM layer are colored in yellow-green. The mesh on the right is used for DRM calculations.

Modified Meshing

The first issue arises due to the presence of dangling nodes in the DRM boundary layer. A mesh node is defined as dangling if it is located on the edge or the face of some element. Otherwise, it is anchored. In order to satisfy the continuity of displacement field, displacement of a dangling node needs to be the average of the displacement of its anchored neighbors. However, this requirement poses some difficulties while calculating the effective forces in part2. This is basically due to the fact that part2 yields the residual displacements w_e in the exterior region, but the total displacement fields u_i in the interior. If a dangling node has two anchored neighbors, one located in the interior and the other in the exterior, then obviously it is not correct to take the average of these two and set as the displacement of the dangling node. The simplest technique to overcome this problem is to avoid dangling nodes in the DRM layer by enforcing the presence of equal sized elements all around the boundary. In addition to that, one needs to make sure that the sizes of these elements

are the smallest in the simulation domain. Or at least, the DRM layer should be some distance away from the building clusters in case of buildings with smaller element sizes. Figure 2.4 shows the vertical cuts of two simulation domains, with and without dangling nodes.

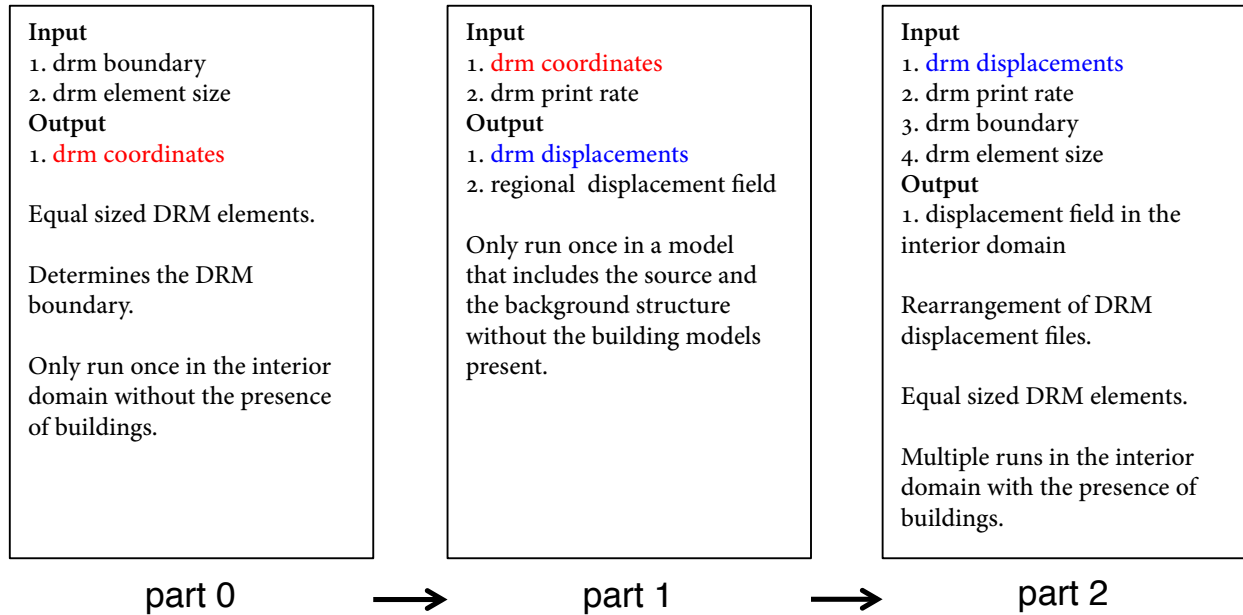


Figure 2.5: Summary figure that shows how the different parts of the DRM are related to each other. Mesher is modified in part0 and part2, whereas solver is modified in part1 and part2.

Rearranging DRM Files in part2

The second difficulty arises while trying to store and read the DRM displacement data in part1 and part2, respectively. Each processor writes the displacement data of its DRM nodes in a separate file in part1. This may result in hundreds of these files, each of which may easily be as large as tens or hundreds of gigabytes in size, depending on the number of time steps and the number of DRM nodes. This may be problematic in part2 since no measure is taken to guarantee that processors find all the data they need contiguously in a single file. To overcome this, these displacement files are rearranged in part2 before the solver starts so that each processor has its displacement data contiguously in a single file. This is also crucial for taking advantage of IOBUF which is an I/O buffering library that can reduce the I/O wait time for programs that read or write large files sequentially. Another way to reduce I/O time is to decrease file sizes in part1 by storing

displacements at every n -th time step. I used $n=40$ in the simulations. Finally, Figure 2.5 shows the summary of part0, part1 and part2.

CHAPTER 3

Case Study I : Site-City Interaction Using Torsionally Uncoupled Buildings

The realistic arrangement of buildings used in [Taborda and Bielak \(2011b,a\)](#) made it difficult to differentiate the multiple interactions that take place in 3D city-like models under realistic seismic excitation. Here, we use the same modeling framework introduced by [Taborda \(2010\)](#) to investigate the dynamics of building clusters during earthquakes. We conduct a series of numerical simulations that synthesize the earthquake source and the coupled response of idealized building clusters; and we pay particular attention to the building at the center of each cluster, which we use as reference throughout our analysis. We compare the response of the center building with that of an identical building located at the same site, but with no other buildings present. This allows us to separate the site-city effects for this building from those solely due to soil-structure interaction. As explained in detail in [Chapter 2](#), Hercules and the Domain Reduction Method (DRM) are used to perform the simulations.

We proceed with the analysis of results in a sequential manner, starting from the earthquake source and moving on to the individual and collective response of the building models. We begin by modeling the 1994 Northridge earthquake and describing the ground motion in the San Fernando Valley, with emphasis in the smaller area of interest that contains the building clusters.

Such 3D wave propagation and ground motion simulations are by now becoming commonplace, and, with our approach, we need to perform the regional simulation only once. This simulation automatically incorporates the effect of the different types of body and surface waves and provides the spatial and temporal (and thus frequency) variability of the free-field motion within the region of interest. This is the main reason we model one particular historic earthquake. This also allows us to examine how the spatial variability of the ground motion within a small region of interest influences the earthquake response of identical structures located at different sites. We then analyze in detail the SSI response of a single building model, as a reference that can be used to identify the changes caused by the presence of additional building models across various cluster arrangements. We perform a parametric study that includes different separations and numbers of structures for three building models with different fundamental natural frequencies. We are particularly interested in addressing the overall SSSI effects, rather than on the detailed behavior of individual structures. Therefore, we use simple solid anelastic models to represent the main dynamic properties of buildings. We also consider two soil conditions, original and softened, in order to simulate approximately the effect of soil nonlinearity on the response of the soil-structure systems.

3.1 Building Models

We model the structure-foundation systems using homogeneous blocks made up of the same type of solid hexahedral finite elements as those used for representing the crustal structure and the soil. This may be considered as a generalization to three-dimensions of the well-known shear beam or bending beam models, but the solid 3D model accounts naturally for both shear and bending effects. Previous similar studies in 2D have also used solid block-models to represent buildings as a first approximation to characterizing SCI effects (e.g. [Wirgin and Bard, 1996](#); [Tsogka and Wirgin, 2003](#); [Kham et al., 2006](#)). We select the elastic properties of the solid elements in such a way that the block-model of each building matches the height, base dimensions, and fundamental natural frequency of the intended target structure. We consider three building models, B1, B2, and

B3, to represent structures of approximately 3, 13, and 40 stories, respectively. In each case we define the nominal fundamental natural period as 1/10th the total number of stories, and assume that the interstory height varies between 4 and 5 m. Thus, the nominal fundamental periods of the three structure types are 0.3, 1.3, and 4.0 s. We define the material properties of each building type in the following manner. We keep ρ constant and set $V_P = 2.5V_S$. Then, we adjust the value of V_S so that the actual fixed-base fundamental natural period of the building model comes close to the nominal one. Material attenuation is considered in the elements of the building models in the form of Rayleigh damping, which is set equal to 5 percent of the critical value for the frequency range used in the simulation [Bielak et al. \(1999\)](#). Table 3.1 shows the height and base dimensions, and the actual fixed base and flexible soil fundamental natural frequencies of the three building models, plus the material properties of the finite elements used to build the block-models. The values of V_S assigned to each building type are different because they depend on the buildings dimensions. The flexible soil frequencies are calculated with respect to two different soil conditions, as explained later in the text. Changes in the natural frequencies are in all cases less than 10 percent. The largest changes occur for the smaller, stiffer building models. The foundations depths were chosen based on an approximate number of underground stories (1, 2, and 4 for building types B1, B2 and B3, respectively), and their mechanical properties defined assuming that the foundations are significantly stiffer than their corresponding superstructures.

The selection of the modeling approach to represent the buildings obeys our particular interest in addressing the overall effects of SSI and SSSI, rather than on the detailed behavior of individual structures. Thus our choice to use simple solid anelastic models to represent the primary dynamic properties of buildings (e.g., fundamental natural frequency and damping). The values we used for the material properties of the block-models are similar to those used in previous studies (e.g. [Kham et al., 2006](#)).

Table 3.1: Dimensions and fundamental period and frequencies of both the rigid-base and flexible-soil building models, and mechanical properties of the finite elements used in the building and foundation blocks. ICB refers to Isolated Control Building.

Type	Height (m)	Found. Depth (m)	Base Size (m × m)	Rigid Base Fund. Nat. Period (s)	Fund. Nat. Freq. (Hz)			V_S (m/s)	V_P (m/s)	ρ (kg/m ³)
					Fixed Base	SSI for ICB				
						Orig. Soil	Mod. Soil			
B1	15	5	10 × 10	0.30	3.37	3.20	3.06	320	800	300
B2	55	10	30 × 30	1.25	0.80	0.78	0.76	340	850	300
B3	160	15	50 × 50	3.70	0.27	0.26	0.25	500	1250	300
Foundation								750	1875	300

3.2 Earthquake and Regional Simulation

We consider the ground motion of the M_w 6.7 1994 Northridge, California, earthquake as the seismic excitation. In Step I, we simulate the ground motion during the earthquake in a volume domain of 81.92 km × 81.92 km × 40.96 km that includes the entire San Fernando Valley and some of the Los Angeles metropolitan area. Figure 3.1 shows the region of interest, the simulation domain, the fault plane, and the earthquake source model’s distribution of the total slip. This model corresponds to the extended kinematic fault rupture proposed by [Graves and Pitarka \(2010\)](#). The plane has a strike equal to 122°, and dips at an angle of 40°. The rupture model consists of a set of 140 × 140 asperities with variable rake angles, and slip functions with an average and maximum total slip equal to 66 and 281 cm, respectively. Using Hercules, we build a FE mesh of the simulation domain tailored to a minimum shear wave velocity, $V_{Smin} = 200$ m/s and a maximum frequency, $f_{max} = 5$ Hz. Hercules creates the mesh automatically by recursively querying a discrete representation of the seismic velocity model of the region of interest. Here, the elastic material properties of the individual elements were determined from the Community

Velocity Model of the Southern California Earthquake Center (CVM-S), version 4.1. This model is based on the original work by [Magistrale et al. \(1996, 2000\)](#) and has been used extensively in similar earthquake simulations (e.g. [Olsen et al., 2009](#); [Bielak et al., 2010](#)). Figure 3.2 shows the spatial distribution of the shear wave velocity at the free-surface, as obtained from the CVM-S. Details of the meshing procedure and element-size defining criteria can be found in Chapter 2.

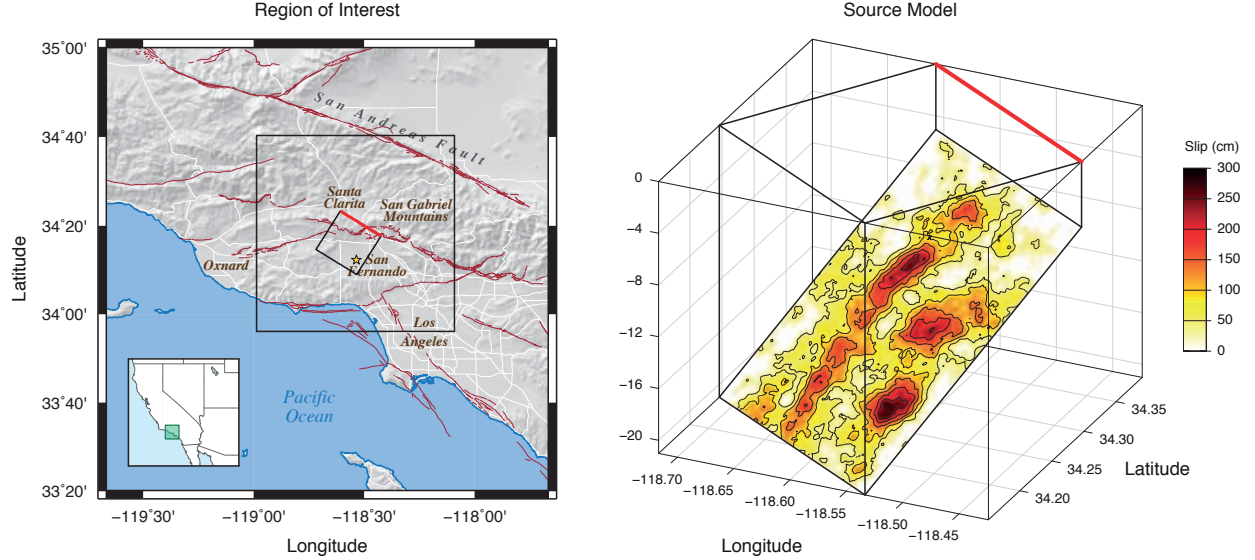


Figure 3.1: (Left) Region of interest in Southern California. The interior large box indicates the horizontal projection of the simulation domain and the small tilted box is the projection of the fault plane. The epicenter of the 1994 Northridge earthquake is indicated with a star. (Right) Distribution of total slip on the fault plane following to the source model by [Graves and Pitarka \(2010\)](#).

Although deterministic earthquake simulations have been predominantly limited to low frequencies (< 2 Hz), a recent study has shown that simulations at higher frequencies, as considered here, can produce realistic ground motion records if provided with the appropriate velocity and source models ([Taborda and Bielak, 2013](#)). It is out of the scope of this thesis to validate the ground motions simulated for the Northridge earthquake. We assume that both the CVM-S, and the source model proposed by [Graves and Pitarka \(2010\)](#) are plausible representations of the regional subsurface structure and the earthquake ground characteristics for the purpose of studying SCI effects.

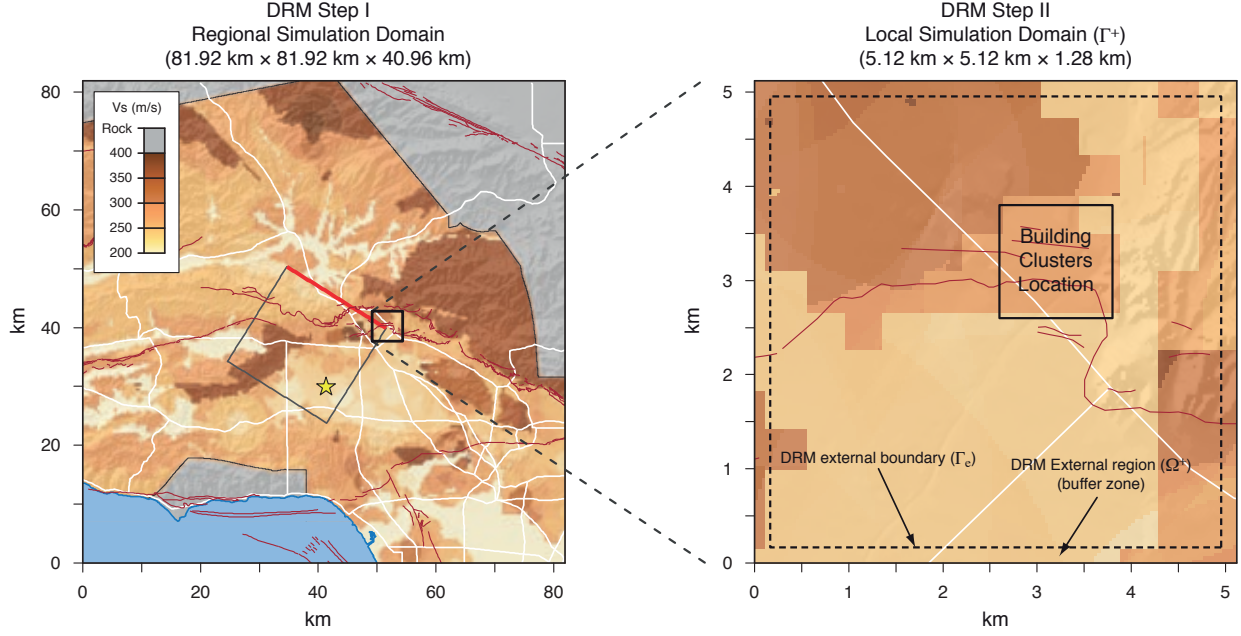


Figure 3.2: (Left) Regional simulation domain used and (right) detail of the local sub-region of interest. The location of the fault plane and the building clusters area are outlined in black lines. The epicenter of the 1994 Northridge earthquake is indicated by a star. The background shows the shear wave velocity at the free surface corresponding to the CVM-S model.

3.3 Subregion of Interest and Building Clusters

In Step II, we focus our attention on a subdomain of $5.12 \text{ km} \times 5.12 \text{ km}$, as shown in Figure 3.2. The location of this area coincides with one of the zones where a significant number of buildings were red-tagged after the 1994 Northridge earthquake (e.g. [Hartzell et al., 1996](#); [Meremonte et al., 1996](#)). We consider the behavior of various building clusters in the smaller area shown in the figure, which consist of regular $N \times N$ buildings, where $N = 1, 3, 5$, and 9 , for each of the three building models described earlier. The special case of a single building, $N = 1$, is hereafter referred to as the isolated control building (ICB), and the clusters with $N = 3, 5$, and 9 are identified as C1, C2 and C3, respectively. In addition, each cluster is examined using three different separations, S1, S2 and S3, between the buildings. The characteristics of the different building clusters and separations are described in Tables 3.2 and 3.3.

Table 3.2: Description of the different building clusters.

Cluster Type	Arrangement	Total Number of Buildings
ICB	1×1	1
C1	3×3	9
C2	5×5	25
C3	9×9	81

Figure 3.3 illustrates a typical building cluster and the simulation domains for Steps I and II. Notice that the center building, denoted here as CB, remains at the same location as the ICB for all the arrangements, but includes the interaction effects with the surrounding structures. The CB and the ICB are used in this study to help differentiate the collective SCI from the individual SSI effects as we vary the building cluster arrangements. We use regular building clusters as opposed to more realistic (random) city-like arrangements, as we are interested mainly in estimating the effect of various parameters such as the number of structures and separation between them on the response of these systems.

Table 3.3: Separation considered for the different spatial distribution of building clusters.

Building Type	Fixed-base		Seperation (m)		
	Nat. Period (s)	Nat. Freq. (Hz)	S1	S2	S3
B1	0.30	3.37	10	15	20
B2	1.25	0.80	15	30	45
B3	3.70	0.27	20	40	60

In an earlier study [Taborda and Bielak \(2011b,a\)](#), we considered a single distribution of heterogeneous building models meant to characterize more closely the building arrangement in a downtown setting. The overall results are qualitatively similar to those of the present study. The

choice of cluster arrangements is motivated by our particular desire to examine the general characteristics of SSSI effects in building clusters, and the influence of various parameters, such as the number of buildings in a cluster, the separation between individual buildings, base dimensions and dynamic properties on the overall system behavior, rather than the response of individual structures. Therefore, the cases we consider are meant to help gain a global insight into the effects of these parameters. They are not intended to illustrate any one particular situation.

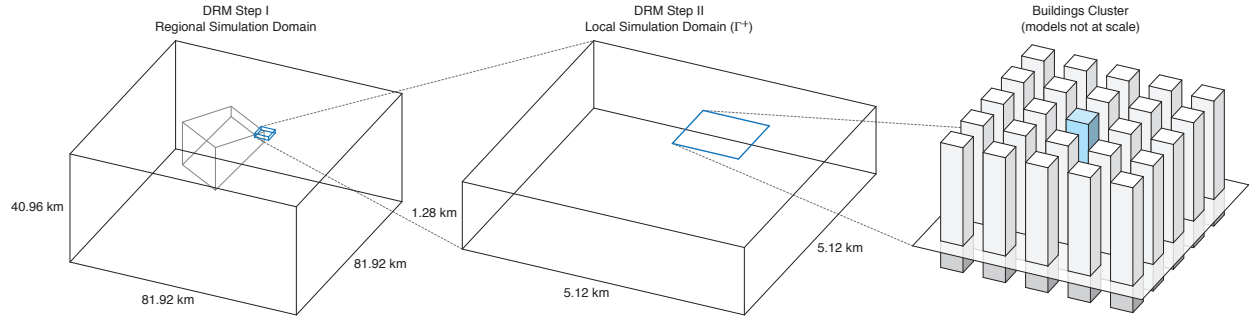


Figure 3.3: (Left) Volume domain for the regional simulation; (center) Simulation domain for the subregion of interest; and (right) schematic representation of the configuration of the buildings cluster model. The control building (CB) is indicated in color.

3.3.1 Softened Soil Conditions

It is widely accepted that the Northridge earthquake produced widespread nonlinear soil behavior in the Los Angeles and San Fernando basins (e.g. [Trifunac and Todorovska, 1996](#); [Field et al., 1997](#); [Beresnev et al., 1998](#)). We were therefore motivated to consider an additional set of simulations under conditions that might resemble the changes in soil stiffness and effective damping due to nonlinearity. This, in turn, will allow us to investigate the effect of the soil properties on the behavior of the individual and collective response of the soil-structure systems and their interaction with the ground motion. To simulate the nonlinear soil behavior, we use equivalent reduced shear moduli and increased damping ratios in soft-soil deposits in the DRM region and perform a second set of simulations only within the reduced domain for all the possible combinations of building models and cluster arrangements. We refer to the first set of simulations that use the CVM-S material properties, as the simulations under original soil conditions, and to the second set, which

uses the modified shear moduli and damping ratios, as the simulations under modified or softened soil conditions. The modified shear wave velocities and damping ratios used for the softened soil simulations were obtained as follows. Based on the values of peak horizontal velocity (\dot{x}) obtained from the simulation with the original soil model, we approximated the shear strains (γ) near the free surface using the expression A/V_S , where A is an empirical scaling function. This expression was used by [Trifunac et al. \(1996\)](#) to estimate the strains observed during the Northridge earthquake. According to [Trifunac et al. \(1996\)](#), in the case of the shear strains in the horizontal plane, A can be taken as a constant equal to 0.22. The results over the DRM region yielded a maximum shear strain, $(\gamma_{max}) = 1\text{E-}2.4$ near the surface. This value is in agreement with observations reported in the literature, corresponding to reductions of up to 50 percent in the effective stiffness of the soil (e.g. [Beresnev et al., 1998](#)). Using the expressions proposed by [J.A. Santos \(2000\)](#) for the lower and upper bounds of the relationship between the normalized shear strain ratio ($\gamma^* = \gamma/\gamma_t^r$) and the shear modulus degradation factor (G/G_0), we obtained the corresponding average values for G/G_0 . These were, in turn, used to compute the new values of V_S in the soil deposits within the DRM region. Computing γ^* entails knowing the reference shear-strain, γ_t^r , which is defined as the corresponding shear strain for a reference degradation factor, $G/G_0 = 0.7$. For this, we used typical depth-dependent modulus reduction curves, such as those provided by [Hartzell et al. \(1996\)](#). Similarly, the modified damping ratios were obtained using the expression proposed by [Ishibashi and Zhang \(1993\)](#) for the relationship between damping and shear strain.

The differences between the original and softened soil models in terms of the profiles of shear wave velocity and damping ratio beneath the region of interest are illustrated in Figure 3.4. The left panel compares the ranges of variation in the V_S profiles for both models in the first 200 m beneath the free surface in the building cluster area, and the right panel compares the variations in damping. Notice that the modifications introduced in the softened soil model only affect the upper 150 m. The maximum reductions in V_S occur near the surface, with average values decreasing from 280 to 150 m/s. Notice, however, that for both soil conditions, V_S falls below 300 m/s only within the top 20 m of soil. Damping is significantly increased at different depths, with values increasing

up to 19 percent of the critical damping. The softest soil deposits in the building clusters area are located on the top-right corner of the region of interest (see Figure 3.2). The shear-wave velocity and damping profiles at this particular location are denoted in Figure 3.4 by dashed lines.

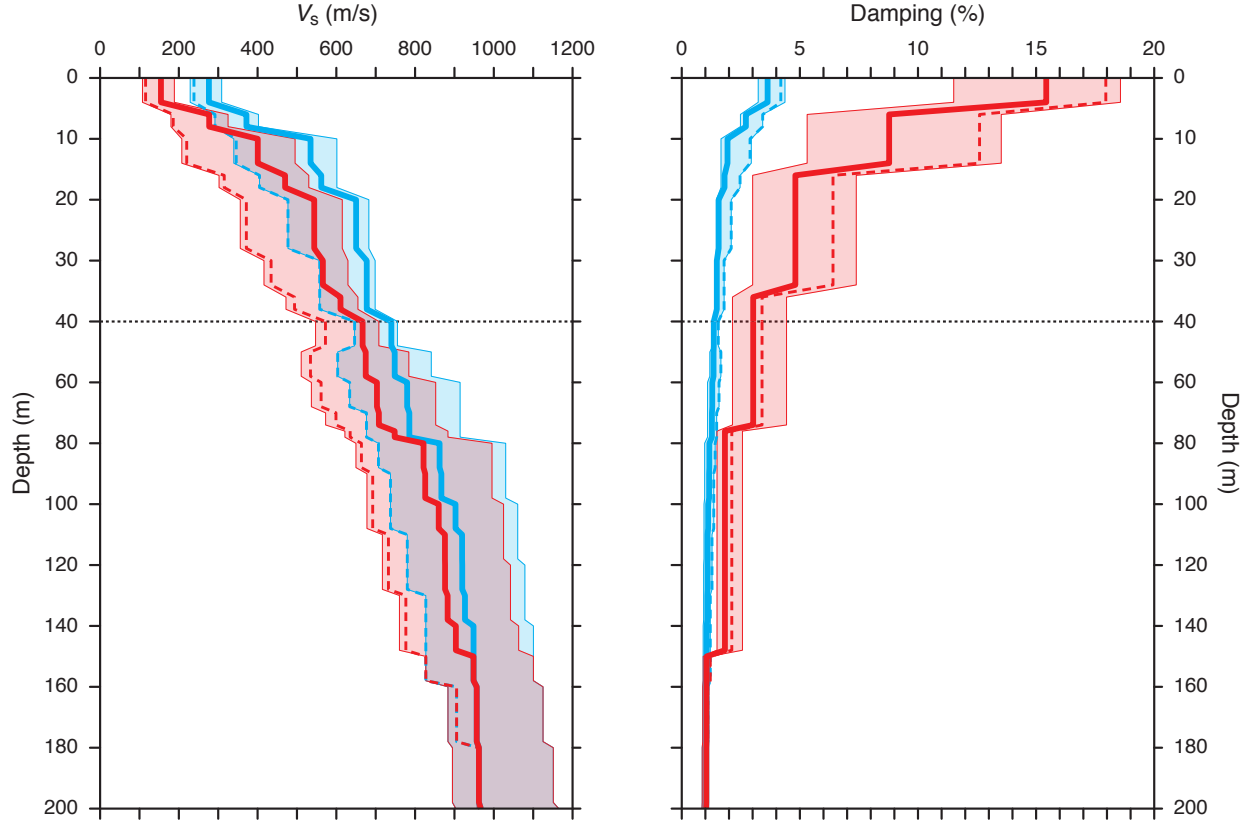


Figure 3.4: Shear wave velocity (V_s) (left) and critical damping ratio (right) profiles for the original (blue) and softened (red) soil models beneath the building clusters area. Shaded areas indicate the ranges of variation in each case and thick lines represent the average values. The dashed lines in the V_s profile correspond to the soil near the top-right corner of the building clusters area used for reference as a zone with very soft soil conditions.

3.3.2 Computational Effort and Performance

Simulations were run in Kraken at the U.S. National Institute for Computational Sciences. Kraken is a Cray XT5 supercomputer with 112,896 cores distributed on 9,408 compute nodes. Details related to the computational effort and performance are included in Table B.1 in the Appendix Figure B.

3.4 Results and Analysis

3.4.1 Regional Response

Figure 3.5 shows a sequence of snapshots of the amplitude of the free-surface horizontal velocity—calculated as the square root of the sum of the squares of the east-west (EW) and north-south (NS) components of motion—at different times during the Step I simulation. The wave propagation observed here indicates significant rupture directivity and basin effects. The latter are particularly evident from the continued vibration levels at and after 12.8 s. The amplifications within the area of the DRM box are mostly due to a wave front reflected by the San Gabriel Mountains (including edge effects), which travels south and southeast. This is highlighted at the bottom of Figure 3.5, where the ground motion in the DRM region is shown in greater detail. The passage of the main wave front through this area occurs at 9.6 s, but the reflected waves coming from the northwest pass by between 14.4 s and 19.2 s. These reflected waves carry as much energy as the main shock, reaching horizontal ground velocities as high as 2 m/s. This value is of the same order as the maximum value of 1.75 m/s recorded during the Northridge earthquake at the Rinaldi station (Trifunac et al., 1998). In the case of the DRM region, Figure 3.6 shows the peak values of the amplitude of the free-surface horizontal velocity for both the original and the softened soil conditions (obtained from a Step II simulation without building models). The maximum values were 2.45 and 3.80 m/s for each case. Within the building clusters area, in particular, the peak values vary between about 0.55 and 1.5 m/s, and between 0.6 and 2.3 m/s for the original and softened soil models, respectively. These values within the building cluster area are in close agreement with the PGV recorded at the Rinaldi station during the earthquake. This figure also shows the level of spatial variability that occurs in an area of only $1.2 \text{ km} \times 1.2 \text{ km}$. Similar levels of variability were observed by Meremonte et al. (1996) for the case of a series of aftershocks of the 1994 Northridge earthquake.

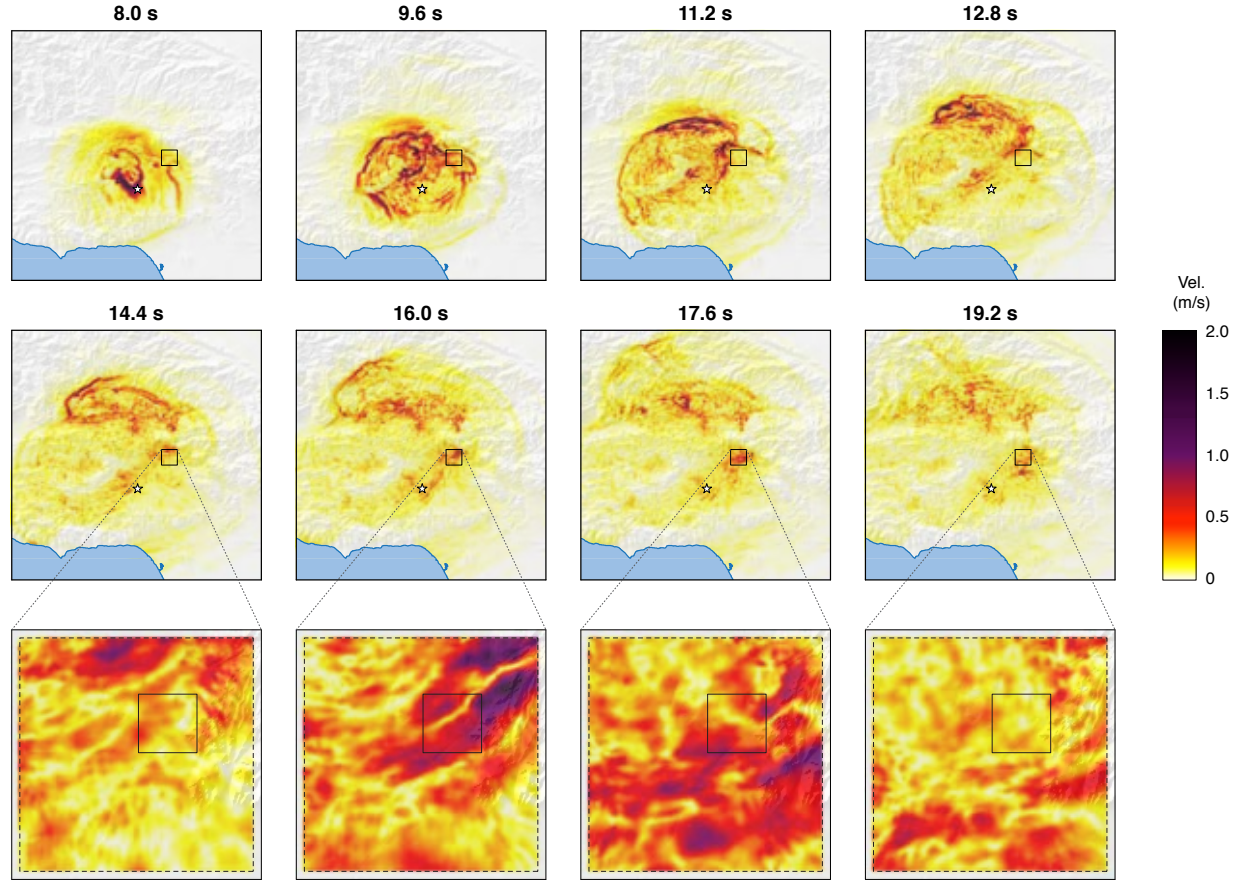


Figure 3.5: Still-frames of the amplitude of the free-surface horizontal velocity for the regional-scale simulation at different times after the faults rupture, and details of the DRM region of interest (for later times, using the original soil conditions). The epicenter of the earthquake is indicated by a star. The small box in the upper two rows corresponds to the DRM area enlarged in the bottom row. The dashed and medium boxes in the DRM frames at the bottom correspond to the DRM external boundary and the building clusters area, respectively (see Figure 3.2).

The spatial variability of the free-field motion within the buildings' area (with no buildings present) is illustrated in Figure 3.7, for both the original and softened soil cases. The top panels show synthetic seismograms of the horizontal velocity in the NS and EW directions along 25 stations equally spaced along a diagonal of 1.7 km across the building cluster area. Notice the variability in the amplitude and frequency content of the seismograms along the line. The amplitude of the ground motion is appreciably higher near the north-east corner (green dot), where the soil is softer. The middle panels show the average Fourier transform of the velocities ± 1 standard deviation in a regular grid of 13×13 stations equally spaced at 100 m throughout the same area.

Notice that for both soil cases, the upper bound of the standard deviation has spectral ordinates that are twice as large as the corresponding ordinates of the lower bound. This provides a measure of the spatial variability of the free-field ground motion to which the buildings will be exposed.

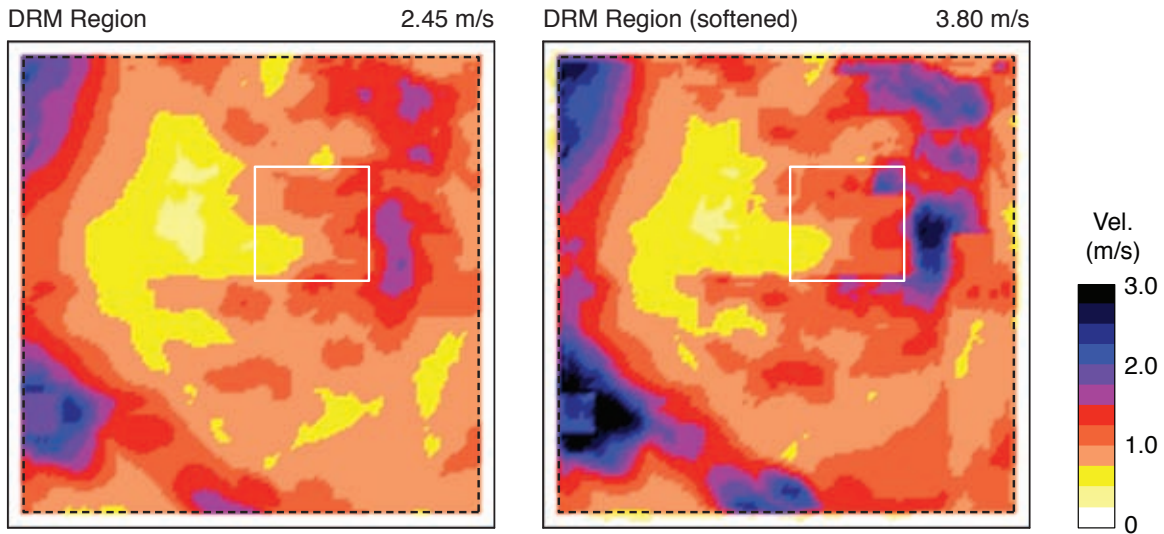


Figure 3.6: Amplitude of the peak free-surface horizontal velocity for the DRM region of interest using the original velocity model (left) and the softened model (right). Maximum values are indicated at the top of each frame and to the right. The small ($1.2 \text{ km} \times 1.2 \text{ km}$) square subregion inside the DRM region is where the building clusters will be located.

Results in Figure 3.7 help visualize the energy distribution of the ground motion with frequency. For both the original and softened soil cases, the spectral amplitudes are somewhat larger in the EW than in the NS direction, and the maximum values occur between 0.7 Hz and 1.1 Hz, and between 0.6 Hz and 1.3 Hz, respectively. In addition, the ground motion in the EW direction exhibits a second set of resonant frequencies between 1.6 Hz and 2 Hz. The energy content decays after 1.5 Hz and 2 Hz and is lowest between 3.5 Hz and 4.55 Hz. Below 1 Hz, the differences between the original and softened soil models are minimal. By contrast, above this value, the softened soil model consistently exhibits an increase in energy, especially between 1.5 Hz and 3 Hz. The relative distribution of both soil models with frequency, however, remains very similar. Figure 3.7 also includes the average of the horizontal over vertical (H/V) spectral ratios of the free-field ground motion within the area of $1.2 \text{ km} \times 1.2 \text{ km}$ at the location of the buildings—computed for the ground response without the presence of the structures at the same 100 m spaced

grid points.

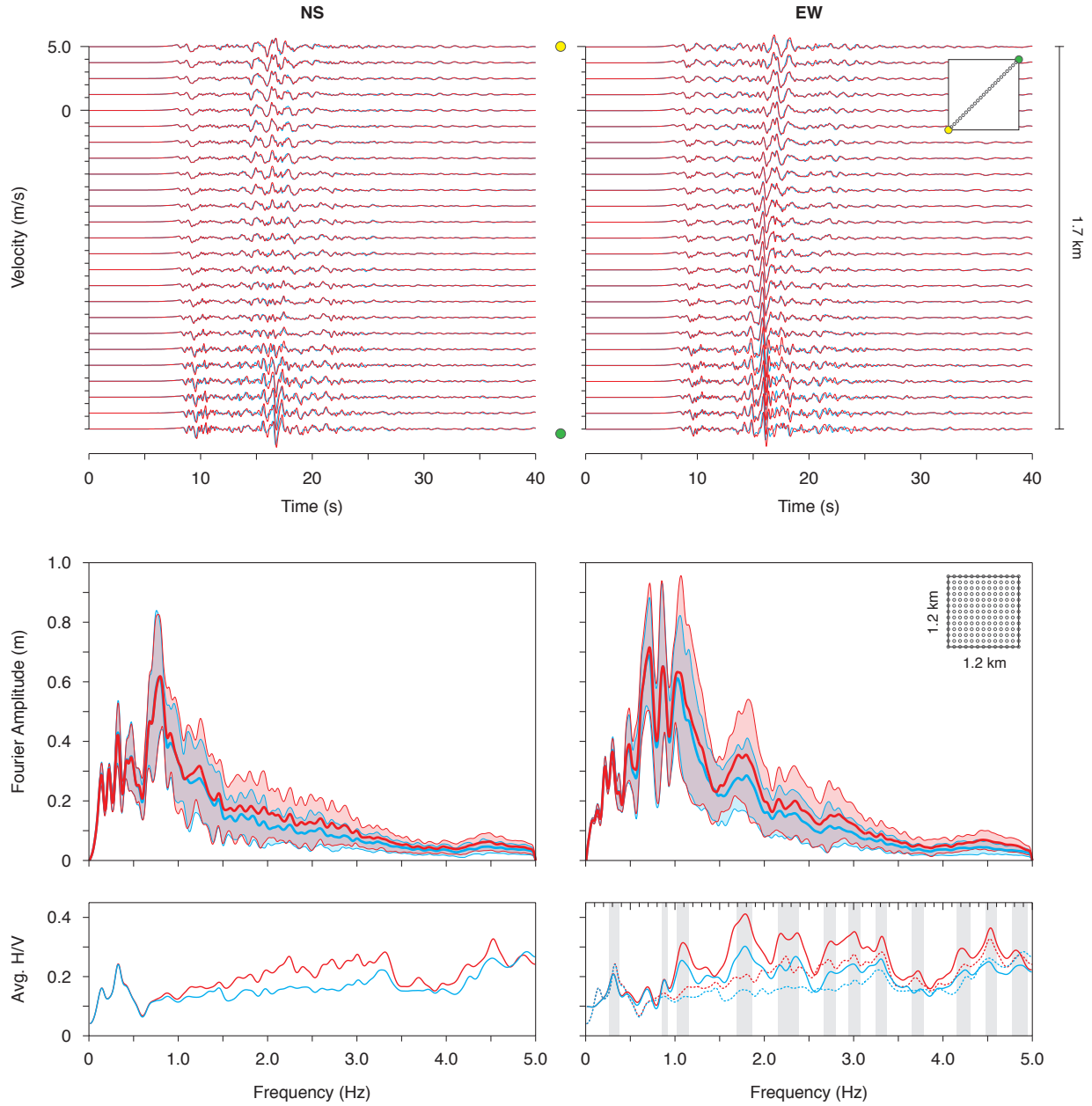


Figure 3.7: Top: velocity time series in both the NS and EW directions for a sequence of stations equidistantly distributed along a diagonal of 1.7 km from the southwest to the northeast corners of the building clusters area (see Figure 3.2). Middle: average Fourier amplitude spectra of the ground velocity within the 1.2 km \times 1.2 km buildings area, ± 1 standard deviation (shaded areas). Bottom: average H/V spectral ratio within the same area. In general, blue lines correspond to the simulation using the original soil model, and red lines to the softened soil model. The average H/V ratios for NS are repeated in the EW frame using dashed lines for cross referencing. In the same frame, the gray shaded areas indicate the presence of coincident resonant peaks in both NS and EW.

H/V ratios are often used to infer the fundamental natural frequency of sites using ambient vibration tests, but they can sometimes be difficult to interpret under strong ground shaking. Here, however, despite the 3D nature of the model and complexity of the source, they provide some insight about the characteristics of the ground motion. At the bottom-right frame of Figure 3.7, we highlight the presence of some resonant peaks that appear to be associated with the natural frequencies of the site. It is noteworthy that the peak value of the H/V ratio occurs at the same resonant frequencies for the EW and NS directions. The fundamental natural frequency associated with the underlying basin appears to be at 0.32 Hz. Higher resonant peaks associated with shallower deposits are visible at about 1.1, 1.8, 2.3, 3, and 4 Hz, among several other resonant, but less prominent peaks across the spectrum.

3.4.2 Effects of the Building Clusters on the Ground Motion

The combined effect of SSI and SCI on the ground motion within the region of the building clusters is illustrated in Figure 3.8. This figure shows the changes in the amplitude of the peak free-surface horizontal velocity with the buildings present, with respect to the corresponding free-field ground motion (without buildings) for the various arrangements of the B3 model, with the clusters ranging from the isolated 1×1 (ICB) model to the 9×9 (C3) building cluster. This allows us to examine the effect that the building-foundation systems have on the ground motion in the spacing area between the buildings and in the surrounding area, as well as on the base motion of the buildings themselves. Similar qualitative results were observed for the B1 and B2 model configurations. The results for the isolated case buildings (ICB), which we consider as a baseline for comparison with the results of the various building clusters, show a small increase at the base of the buildings, for the original soils, and a small reduction for the softened soils. There is very little change in the ground motion around the ICBs due to scattered and radiated waves relative to that in the free field. However, changes in the ground motion become more relevant as the number of buildings increases and the separation between them decreases. The changes are greatest, on the order of 10 to 15 percent, for the softened soil cases, the largest number of buildings in the cluster, and the densest

configuration. This is consistent with the results of [Gueguen et al. \(2002\)](#), who introduced the relative occupancy area parameter θ , and found that for the structures they considered, the largest changes in ground motion occur when θ is greatest. Looking now at the motion of the buildings at ground level, reductions on the order of 10 to 15 percent on average are predominant with respect to the corresponding free-field motion, although small amplifications, of about 7 percent, are observed in some cases (especially for the original soil models). The largest reductions, on the order of 40 percent, occur beneath the buildings at the northeast corner in the softened soil models S2-C3 and S3-C3. These buildings are located in an area where the soil is predominantly softer than in the rest of the cluster area, with a minimum $V_S = 110$ m/s (see [Figures 3.2 and 3.4](#)). Since this value is significantly smaller than the foundation stiffness ($V_S = 750$ m/s), the foundation enhances the scattering (or inertial interaction) effects. The free-field velocity in this area is also the largest, with a corresponding PGV of about 2.3 m/s in the softened soil model (see [Figure 3.6](#)). From the results in [Figure 3.8](#) it appears that the building foundations begin to act as a unit vis-à-vis the seismic motion as the number and concentration of buildings increases. This results in an effective surface dimension that gets closer to the wavelengths of the incoming waves; this causes an increase in the amount of scattering. For instance, the building cluster B3-C3-S1 has a total base dimension of $610 \text{ m} \times 610 \text{ m}$. The side dimension is comparable to a wavelength of 625 m that corresponds to a velocity V_{S30} of 500 m/s (see [Figure 3.3](#)), and a frequency of 0.8 Hz, for which the peak free-field motion in the EW direction occurs (see [Figure 3.2](#)).

In order to differentiate between the motion that takes place directly under the buildings, in the space between them, and in the area surrounding them, [Figure 3.9](#) shows three different condensed representations of the change in horizontal velocity at the free-surface level over different subdomains. These condensed results are summarized from the velocity changes distribution shown in [Figure 3.8](#) for the 9×9 40-story (B3-C3) models with different spacings, using the softened model, which is also shown in the top row in [Figure 3.9](#). Condensed changes in the ground motion throughout the entire domain are shown in red. Both minimum and maximum (envelope) values of the velocity changes in the NS and WE directions are shown in a single plane view representa-

tion along with the average values, indicated by dashed lines. These changes with respect to the free-field are then separated into two different contributions: blue shaded areas, which correspond to changes in the ground motion between and around the buildings; and green shaded areas, which show the changes under the buildings at the free-surface level, that is, in the base motion of the buildings.

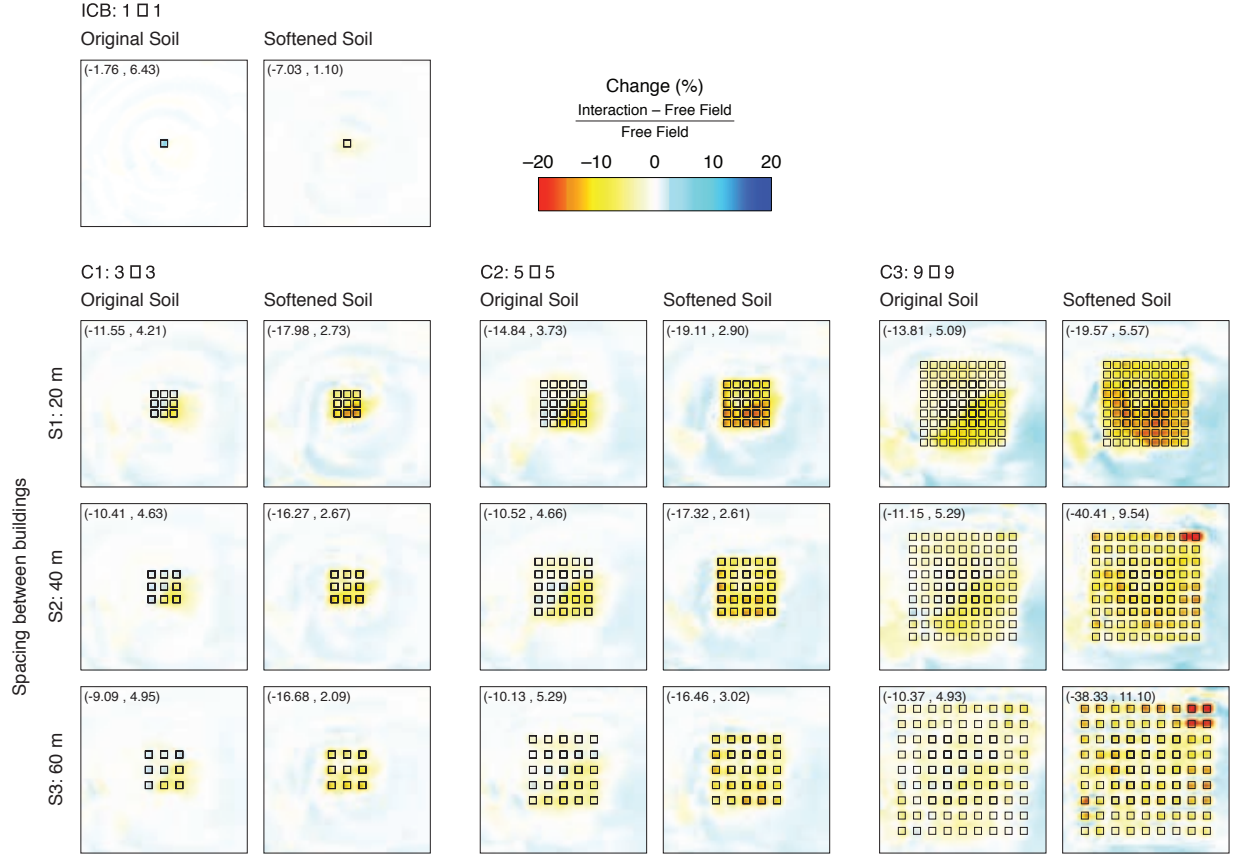


Figure 3.8: Change in the peak horizontal-magnitude velocity at the free-field level for the 40-story building (B3) clusters with variable number of buildings (C1, C2 and C3) and spacing (S1, S2 and S3). Results for the original and softened velocity (soil) models are shown to the left and right of each cluster group, respectively. The case of the isolated control building (ICB) is shown on the top-left for reference. Minimum and maximum values are indicated at the top-left corner of each frame.

In each case, the comparison between the three frames allows one to separate the changes in the ground motion from those at the base of the buildings. Changes in the ground motion in the area surrounding the buildings, for instance, are evenly distributed between reductions and amplifications of about ± 5 percent. Changes in the ground motion between buildings, on the

other hand, oscillate mainly between -15 and +5 percent, except for the smaller area at the top-right corner of the C3-S2 and C3-S3 clusters where the maximum reduction and amplification are between -30 and +10 percent, respectively. This increased variability near the top-right corner is due to the influence of the buildings located in the soft soil portion of the reduced domain. Changes at the base of the buildings (shown in the panels with green shaded areas at the bottom of Figure 3.9) are dominated by reductions, with an average on the order of 20 percent for the majority of the buildings, and maximum reductions of up to 40 percent for the buildings on soft soil. Previous studies that have considered the influence of simplified 2D models of regular and random city configurations on the ground motion observed similar effects (e.g. [Kham et al., 2006](#); [Semblat et al., 2008](#)). In particular, these studies noted that the presence of the buildings on the ground motion tends to decrease the energy of the surface ground motion within the city limits by factors of up to 40 and 50 percent (under ideal conditions of resonance), and that the waves radiated by the buildings may increase the energy of the ground motion outside of the city limits by factors that can exceed by 10 percent the free-field motion energy.

Our results are compatible with these findings, although measured in terms of PGV, which, as pointed out by [Semblat et al. \(2008\)](#), is well correlated with energy. Figures 3.8 and 3.9 presented results limited to various combinations of the B3 model. Figure 3.10 shows a compacted version of these results along with the corresponding results obtained also for the B1 and B2 building models. In particular, this figure shows the minimum, maximum, and average changes in the peak horizontal velocity of the ground motion and the motion at the base of the buildings with respect to the free-field motion (without buildings), for the three building types, the different cluster arrangements and separations, and the two soil conditions. We had previously selected the case of the B3 model because, as it can now be seen in Figure 3.10, it corresponds to the building model for which the largest changes occur. This is true especially for the cluster C3 and the separations S2 and S3, for which the building clusters extend into the softer soils at the northeast corner. The largest deviations from the free-field ground motion (both on average and for the extreme values) occur for the taller structures (B3), which have the deepest foundations, and for the softened soil

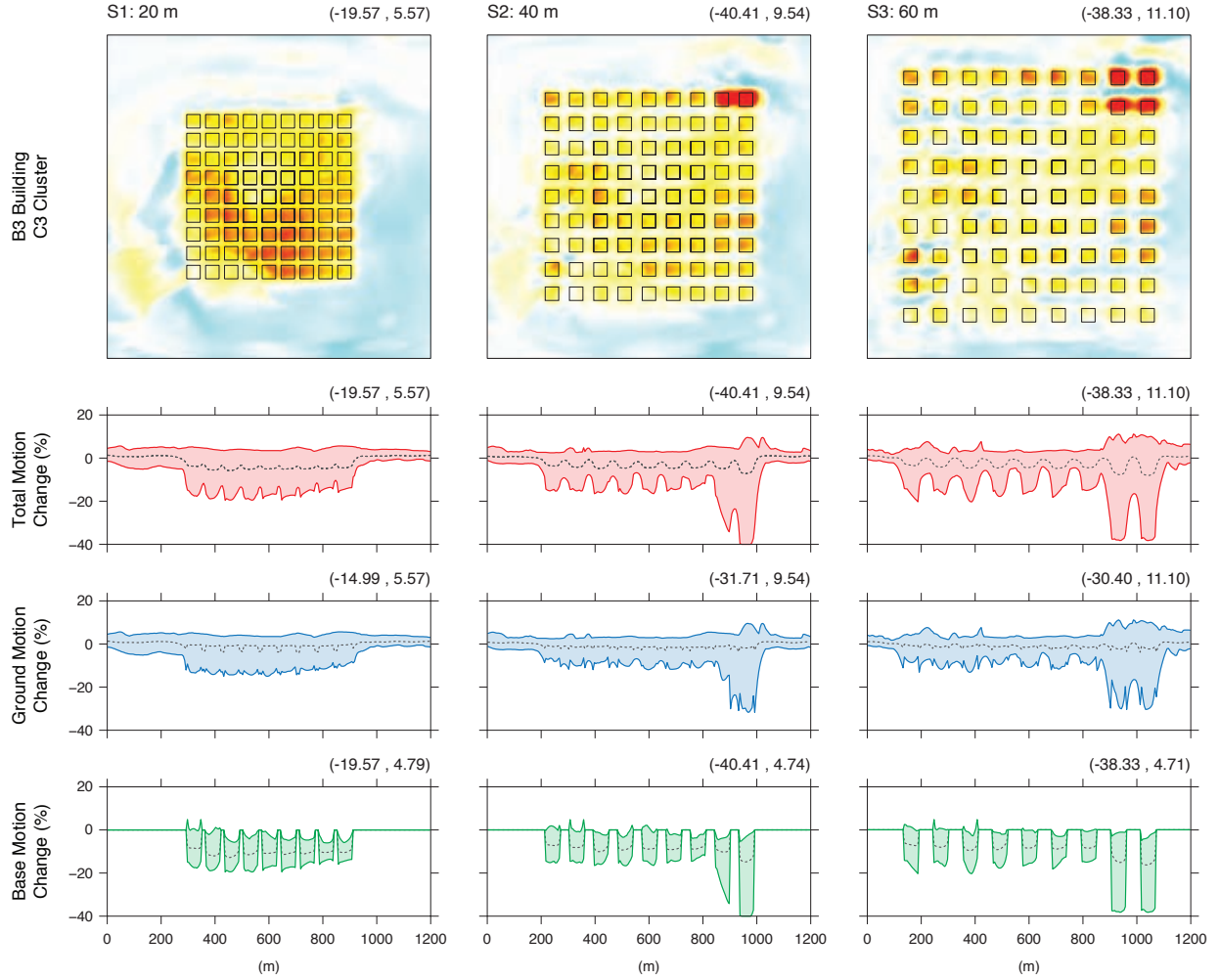


Figure 3.9: Condensed representation of the change in the motion at the free-surface level with (red) and without (blue) considering the buildings, and change in the motion at the base of the buildings (green) for the case of 9×9 40-story buildings (B3-C3) with different spacing, using the softened soil model. Line plots condense the surface plots by computing maxima and minima in NW and EW combined. Average values are indicated by the dashed lines. The color scale for the top panels is the same as in Figure 3.8. Minimum and maximum values are indicated on top of each frame and to the right.

condition. In all cases, the reductions are larger at the bases of the structures than on the ground motion around them. The motion of each building base is variable from point to point because the foundation is flexible and because there are several finite element nodes within each base. This is the reason why in Figure 3.10, the results for each isolated control building (ICB) also show a variability range, including minimum, maximum and average.

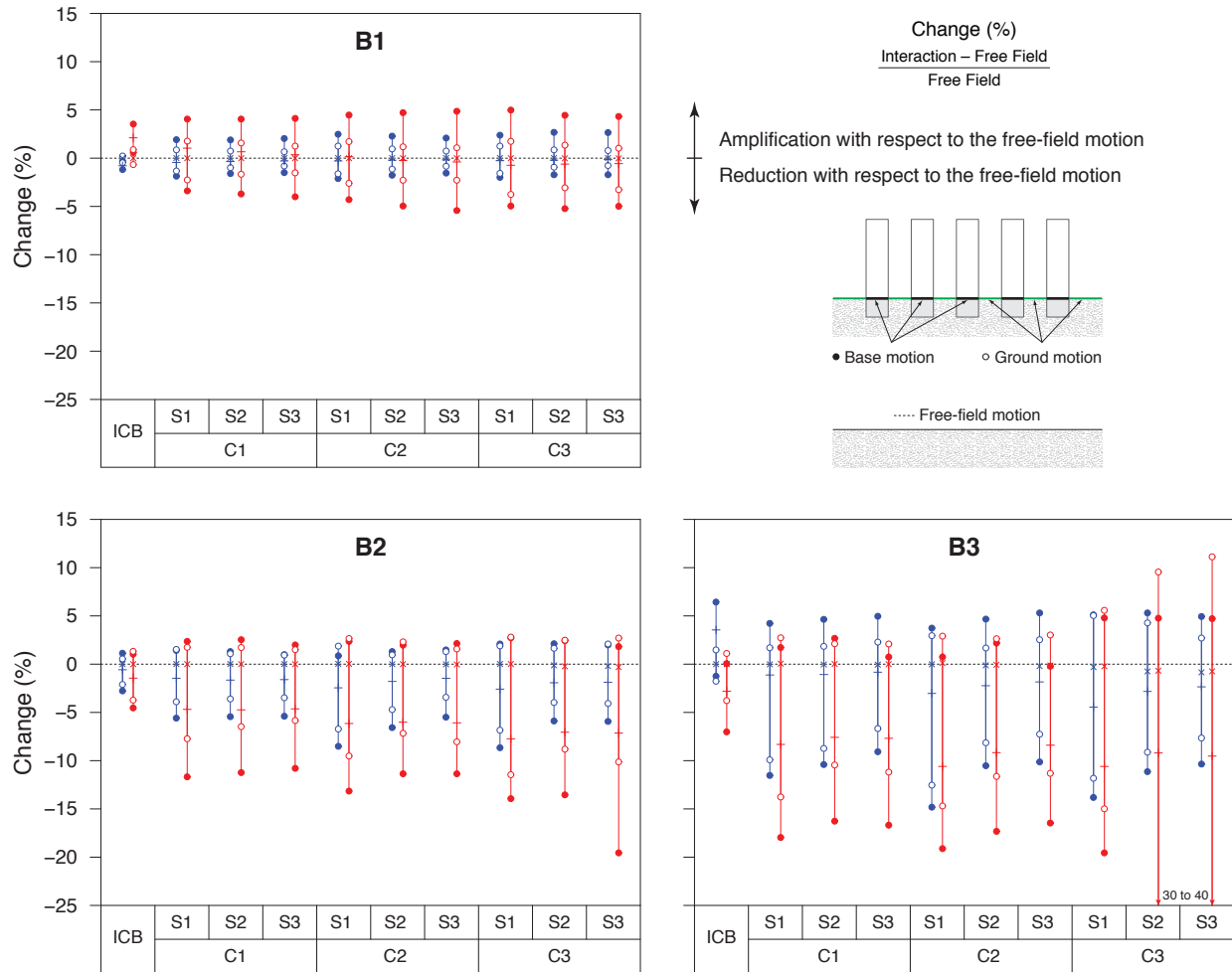


Figure 3.10: Changes in the peak horizontal velocities in the base motion of the buildings (filled symbols) and the ground motion (open symbols) with respect to the free-field response, for the various building models, cluster arrangements, and separations. The intervals go from the minimum to the maximum as indicated by the range lines. In each interval, the average of the change in the base motion is indicated with a horizontal bar, and the average of the change in the ground motion is shown with cross symbol. Blue intervals correspond to the original soil properties and red intervals to the systems with the softened soil conditions. The dashed horizontal line represents no change.

Figure 3.10 also shows that for the original soil condition, the average free-surface ground motion with the buildings present differs little from the corresponding free-field motion, while that at the base of the buildings decreases by values of up to 5 percent. For the softened soil condition, this average change is up to 11 percent, and in some cases, the ground motion is amplified by factors of up to 10 percent. For individual structures, especially those in the NE corner where the soil is softest, the change reaches 40 percent. Except for the case of the ICB, which consists of

a single structure, the results shown in Figures 3.8-3.10 include the effects of both the SSI from each individual soil-foundation-building system and the collective action due to SCI effects. In the following sections we compare the response of the structure located at the center of each cluster (CB), with that of the corresponding single structure at the same location (ICB), in order to isolate the effects of SCI from those of SSI at that location.

3.4.3 Structural Behavior of Buildings

SSI of Isolated Control Building

We now turn to the analysis of the dynamic behavior of the building models in the presence of SCI effects. But first, in order to provide a baseline, we start by examining the response of the ICB to identify its SSI characteristics in the absence of other buildings, i.e., pure SSI without interaction with any other neighboring structures. Figure 3.11 shows the components of the base motion and the roof response of the ICB-B2 model in the EW direction, in the softened soil system. We also show the response of the building on a rigid base. This response was obtained separately using as input at the base of the building the free-field horizontal ground motion recorded at the same location during the simulation with the buildings absent. The relative roof response is obtained as the relative motion with respect to the base. On the other hand, for the flexible-soil case, we subtract the contributions of the base translation and motion at the roof of the structure due to rocking of the foundation in order to determine the relative roof response. That is, in examining the roof response, we are interested in comparing only the corresponding structural deformation of the building system. Several velocity components are shown in Figure 3.11, in both the time and frequency domains (left and middle frames, respectively). These components are defined in the cartoon shown to the right hand side of the figure, in which the motion of the structure is shown only at the roof and at the base of the structure. The panels on the right show the transfer functions of the flexible soil and rigid base models with respect to the free-field motion. The total base (A) and free-field motion (B) show a great similarity; the interaction effects only become apparent by

looking at the contributions of the relative translational base motion ($C = A - B$), and the rocking of the foundation (D) measured as a rocking displacement at the roof level. In the case of the flexible base motion, the differences with respect to the free field are of up to 20 percent during the strong shaking interval in time. It is noteworthy that the relative translational base motion exhibits a high-frequency component that is not apparent in the total base motion. This behavior is due to the predominantly rigid body translational mode of the foundation mass. In this mode, the translation of the base mass is out of phase with the roof motion. This effect, together with the kinematic interaction (wave diffraction) that occurs between the foundation and the surrounding soil result in a reduction of the total base motion at higher frequencies, with respect to the corresponding free-field motion. This is clearly seen in the spectral ratio A/B , where the lateral base motion experiences a maximum reduction above 2.6 Hz on the order of 50 percent. Notice the presence of the two blips that occur around the frequencies of 0.8 Hz and 2.6 Hz, which practically coincide with the first two natural frequencies of the superstructure. The occurrence of such blips has been observed from actual records by [Duke et al. \(1970\)](#); [Bielak \(1971\)](#); [Luco and Contesse \(1973\)](#); [Jennings and Bielak \(1973\)](#), using analytical models. The latter found that the blips are followed by a rapid reduction in the total base motion, due to a dynamic absorber effect. In [Figure 3.11](#), the reduction is much stronger in the higher frequency than in the fundamental frequency, most likely due to the stronger scattering effects associated with the shorter wavelengths in the soil corresponding to this higher frequency. The contribution to the roof motion due to rocking of the base (D) is illustrated in [Figure 3.11](#) in the left and the middle bottom frames. In the time domain, the peak rocking velocity is almost 20 percent of the total base velocity; and in the frequency domain, it is on the order of 30 percent. These values are similar to those observed in the Millikan Library by [Luco et al. \(1987\)](#). Notice that there is also a significant peak in the rocking response at the second natural frequency of the SSI system. The roof velocity in the time domain, illustrated in the leftmost frame at the top, shows only a small difference between the rigid-base and the flexible-soil models, and between the total roof (E) and the relative roof (F) velocities. On the other hand, the corresponding Fourier amplitude spectra (top row, middle column) show visible differences

in the vicinity of the fundamental natural frequency of the structure, where most of the energy of vibration is concentrated, and also, though in smaller amounts, near the second natural frequency.

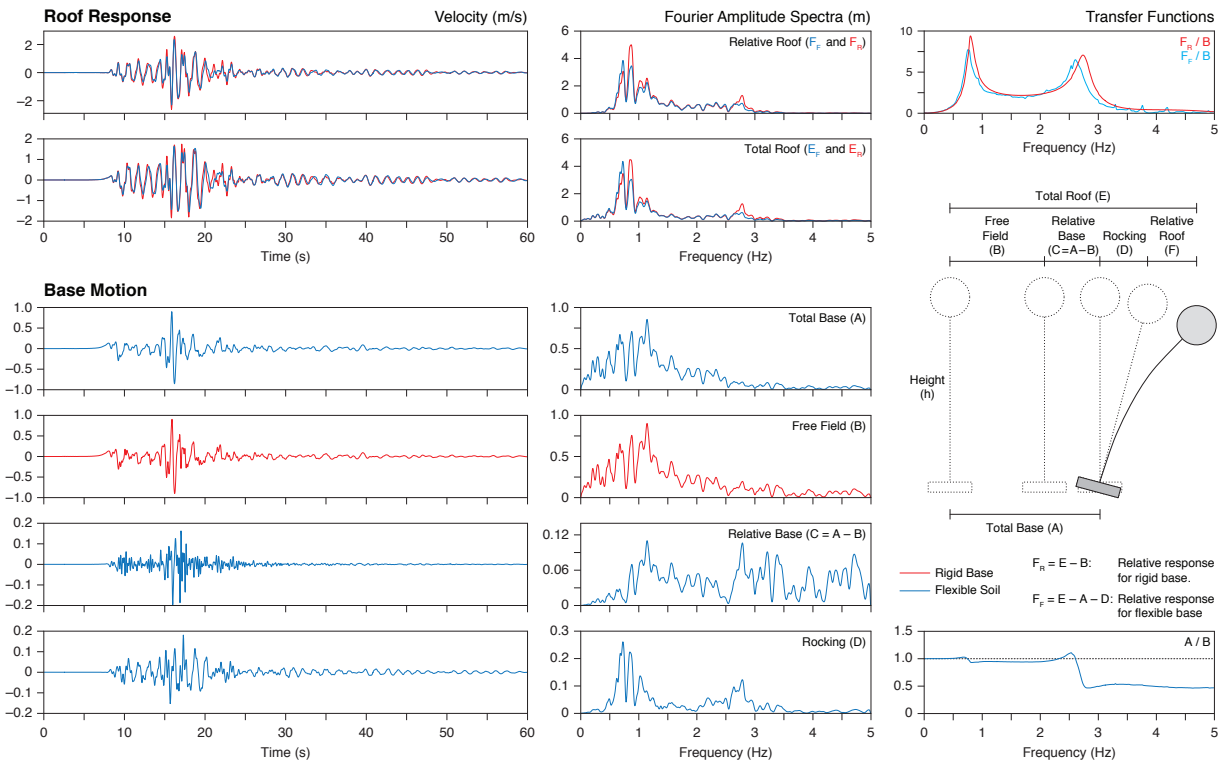


Figure 3.11: Components of the base motion and the relative roof response of the ICB-B2 model for the softened soil system in the EW direction and in both the time (left) and frequency (center) domains, along with the transfer functions (right) of both the base motion (bottom) and the relative roof motion of the flexible-base model (top) with respect to the free-field motion, and in comparison with the corresponding plots of the rigid-base model.

The net effects of SSI on the roof response are more clearly illustrated by comparing the transfer functions F_R/B and F_F/B of the roof response for the rigid-base and flexible-soil cases with respect to the free-field motion. The respective plots in the top right frame show a reduction in the first two natural frequencies and the peaks' amplitudes due to the flexibility of the soil. In this particular case, the first and second natural frequencies shift to the left by about 5 percent, from 0.8 Hz to 0.76 Hz and from 2.73 Hz to 2.61 Hz, respectively. These reductions, along with a reduction of about 10 percent in the amplitude of the peak response due to radiated energy, are the well-known most significant effects of SSI on building structures. Both the frequency and amplitude reductions are moderate for this case because of the low relative stiffness between the structure and

the surrounding soil. Table 3.1 presents the average SSI frequencies for the different building types in the clusters in contrast with those of the reference fixed-base models. The largest reduction, as expected, occurs for the stiffest structure B1, which also has the smallest footprint, and thus the largest relative structure-foundation stiffness.

SCI Effects on Structural Response

The response of a single building supported on a flexible soil, such as the one considered in the previous section, depends on the input motion, the dynamic properties of the structure, and the impedance ratio between the structure, its foundation, and the surrounding soil. In a collection of buildings, however, additional factors, such as the number of buildings and separation between them, influence the response of the individual buildings and of the ensemble. In this section we summarize the overall structural response of the different types of buildings and clusters described in Tables 3.1 to 3.3 in terms of the peak roof response. We recall that all the structures within each cluster are identical, and that we consider structures with three different fixed-base fundamental frequencies: 3.37 Hz (B1), 0.80 Hz (B2), and 0.27 Hz (B3), corresponding approximately to 3-, 13-, and 40-story buildings. We consider three different building clusters (C1, C2, C3) according to the number of buildings in each cluster (3×3 , 5×5 , 9×9), and different separations (S1, S2, S3) as listed in Table 3.3. Figure 3.12 shows the variability of the relative roof displacement normalized by the corresponding building height, F_F/h in Figure 3.11, for each cluster configuration, for both the original and the softened soil conditions, in both the NS and EW directions. We refer to this normalized displacement as the relative roof displacement. Also included, for reference, are the values of the corresponding isolated structure (ICB) and those of the buildings at the center of any given cluster (CB). Solid circles denote the minimum and maximum deformation of all the structures within a given cluster; the mean value is indicated with a small horizontal bar. The normalized relative roof displacement of the corresponding CB is indicated with an open circle. Considering the response of a complete cluster of structures located within the same general area allows us to simultaneously analyze the effects of the spatial variability of the ground motion on

the structural response, the interaction of each structure with the soil, and the coupling through the soil between the multiple structures.

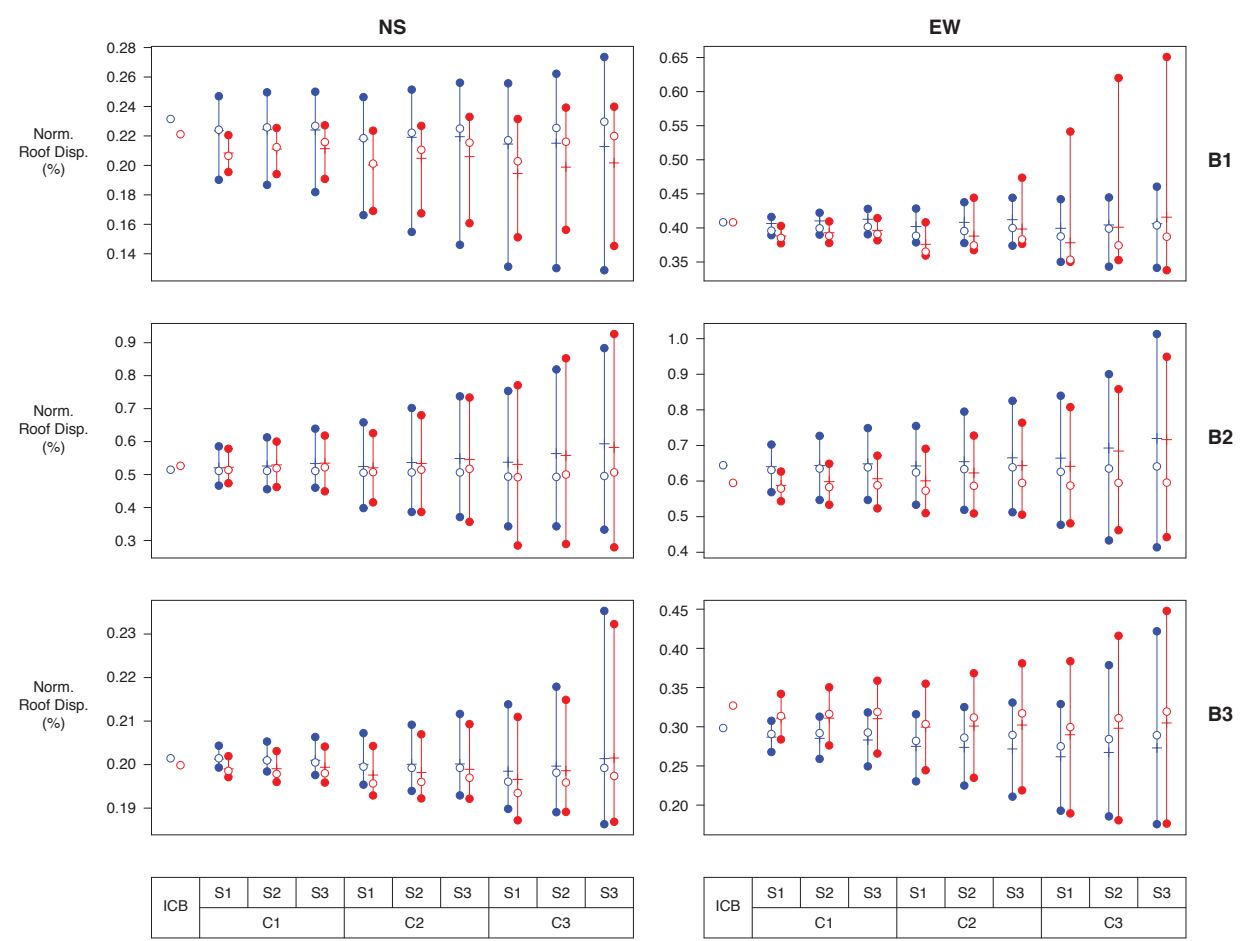


Figure 3.12: Variation in the normalized relative roof displacement for the different configurations in both the NS (left) and EW (right) directions and for the original (blue) and softened (red) soil conditions. Filled symbols show the ranges (minimum to maximum); the average is indicated with a small horizontal bar. Open symbols indicate the normalized relative roof displacement of the center building (CB).

Several observations can be made from Figure 3.12.

- (i) The single most important effect is the pronounced difference that can occur between the minimum and maximum relative roof displacement for the various structures in a given cluster. This is due in large part to the spatial variability of the ground motion. This difference varies from between 0.19 and 0.22 percent for the B1 buildings in the C1-S1 cluster, to variations between 0.28 and 0.93 percent for the B2 buildings in the C3-S3 arrangement. The

largest spread corresponds, in all cases, to the largest building separation, S3, as in this case some of the structures are located in the softest soil.

- (ii) The largest relative roof motion is observed for the B2 structures, whose fundamental fixed-base natural frequency of about 0.8 Hz lies within the range of frequencies for which the free-field ground motion is strongest. Moreover, the largest variation in the roof motion also occurs for the B2 cluster, for the C3 separation, from about 0.28 to 0.93 percent in NS and from about 0.4 to 1 percent in EW. This is due in significant part to the large differences in the free-field ground motion that also occur between 0.7 Hz and 1.25 Hz (see Figure 3.7). Large relative roof displacement spreads also occur for the low-rise B1 structures in the EW direction.
- (iii) For a given cluster, the spread in the normalized relative roof displacement increases with the separation between the structures.
- (iv) The spread also varies with the type of soil (original or softened), though there is no clear pattern. In some cases (B1-NS, B2-EW, B3-NS) the spread is wider for the structures on the original soil model, whereas the converse is true for B3-EW; still in other cases, the trend alternates for the same structural model between one cluster and another (B1-EW, B2-NS). This behavior has to do with factors other than SCI such as the irregular spatial distribution of the free-field ground motion and with the slope of the response spectra near the natural frequencies of the corresponding structures.
- (v) In contrast to the large variability in the spread of the relative roof displacement, its mean values over all the structures in a cluster is much more stable. In no situation does the mean relative displacement deviate from that of the corresponding ICB by more than 20 percent.

To examine the relative influence of the various interaction effects, both at the level of an individual structure and of a cluster, we now compare the results of the CB with those of the corresponding fixed-base and ICB models. Since these two models, namely CB and ICB, are identical,

and are placed at the same location, any change in the response between the two structures is due entirely to SCI effects. Figure 3.13 shows the changes in the peak relative roof displacement of the center building due to the total interaction effects; that is, the sum of soil-structure and site-city interaction, as well as the changes only due to site-city interaction. In particular, the changes due to the total interaction effects are shown in Figure 3.13a. They are computed relative to the corresponding fixed-base response; that is, they include both the kinematic and dynamic interaction effects of each individual soil-structure system, as well as those due to the presence of the surrounding buildings.

We make the following observations about the total interaction effects on the CB.

- (i) For all the B3 ICB and CB cases, in both the original and softened soil models, the relative roof displacement of the structures with interaction effects is greater than that of the corresponding cases with no interaction (positive change); whereas in most of the B2 cases, the relative roof displacement with interaction is less than that of the corresponding cases with no interaction effects (negative change). Total changes in the B1 cases, on the other hand, show mixed results.
- (ii) The largest changes due to interaction effects in the ICB, on the order of 20 percent, occur for the low-rise structure (B1), in the NS direction, and for the tall structure (B3), in the EW direction. In these cases, the relative roof displacement of the structures with interaction is greater than that of the corresponding cases with no interaction. However, while the largest change for the short building (B1) occurs for the model in the original soil, the largest change for the tall structure (B3) occurs for the softened soil. This is due to the particular characteristics of the corresponding response spectra for frequencies in the vicinity of the respective natural frequencies (and modes) that most contribute to the structural response.
- (iii) In all cases, the group effect on the CB is greatest for the clusters with the largest number of buildings and the shortest separation. The influence of the separation between buildings, in particular, has a stronger influence on the CB in the 9×9 cluster of the tall buildings

(B3-C3), which shows a steeper change from the S1 to the S3 separation arrangements.

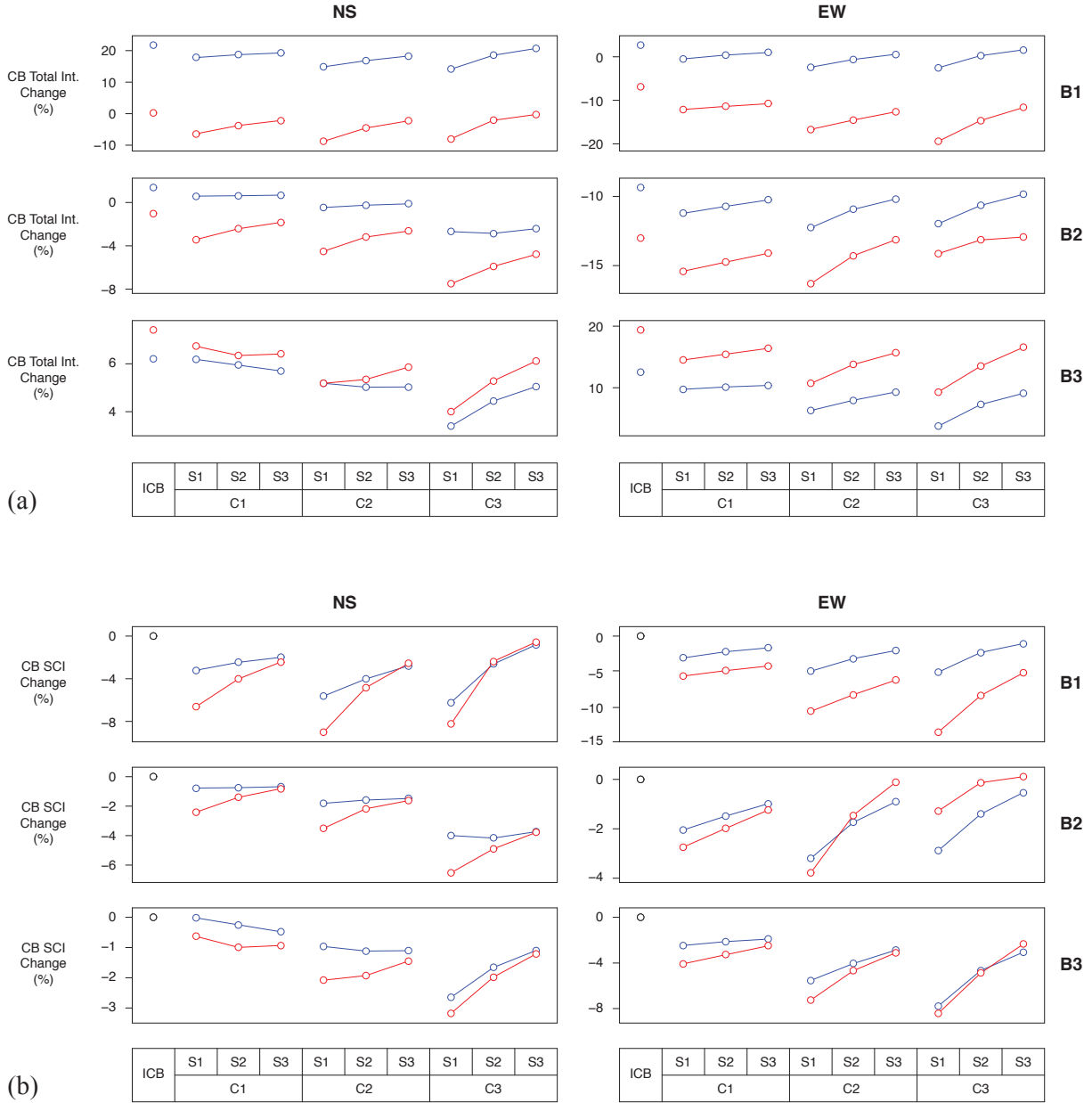


Figure 3.13: Change in the normalized relative roof displacement of the center building (CB) due to interaction effects for the different configurations in both the NS (left) and EW (right) directions and original (blue) and softened (red) soil conditions. (a) Changes due to the total interaction, that is, the sum of soil-structure and site-city interaction effects. (b) Changes in the normalized displacement of the CB due solely to site-city (SCI) interaction effects, relative to the ICB.

The changes due solely to SCI effects are shown in Figure 3.13b. These results are obtained by subtracting the change in the ICB from the total change in the corresponding CB of each cluster

(shown in Figure 3.13a). Using the results of the ICB as reference allows us to isolate the effects due to the presence of other structures in each cluster from those of the individual SSI effects. Therefore, the change due to SCI effects alone in Figure 3.13b is zero for the ICB cases as there are no additional surrounding structures. In all other cases, however, we observe changes with respect to the ICB, as follows:

- (i) While the SCI effect on the relative roof response is generally less pronounced than that of SSI alone, it is quite noticeable in some cases and can add or subtract to the net effects of SSI. For instance, in Figure 3.13a, we observe a reduction of 8 percent for the ICB B1-structure in the EW direction for the softened soil due to SSI alone; but in Figure 3.13b it is shown that clustering effects produce an additional 13.5 percent reduction for the B1-C3-S1 case. On the other hand, the ICB-B3 structure for the softened soil experiences an increase in the response due to SSI alone of 20 percent in the EW direction; but due to the addition of the surrounding buildings, for the case of the B3-C3-S1 cluster, the total amount of interaction decreases to 10 percent.
- (ii) All values in Figure 3.13b are negative. This indicates that, in terms of the total structural response, here measured as the relative roof displacement, SCI generally helps decrease the level of deformation in the structure. However, as illustrated in the previous point, whether that reduction adds or subtracts to the net interaction effects depends on the orientation (positive or negative) of the effects of SSI alone, which are shown for the ICB in Figure 3.13a.
- (iii) As expected, the changes due to SCI decrease as the separation between buildings increases. This change goes to zero as the separation tends to infinity.

Transfer Functions in the Presence of Site-City Interaction

All the numerical results of the present study have been based on the simulation of a single earthquake. As we have seen, the results can help provide insight into the behavior of the individual structures within a cluster and of the extent of coupling between them. However, so far, they do

not explicitly provide any information regarding the possible response that might occur under a different earthquake. While from this single simulation it is not possible to extrapolate the results to an arbitrary earthquake, we can nonetheless extract several transfer functions of interest in order to examine the dynamics of the cluster's response for an earthquake source of similar general characteristics (fault, epicenter, asperities, and rupture velocity), but independent of the particular frequency distribution of the free-field ground motion at a given site. In this section we examine two types of transfer functions. These transfer functions are obtained by dividing the amplitude of the Fourier transform of a given quantity as a function of frequency by the corresponding amplitude of the Fourier transform of the free-field ground motion at the same location. This is done for the total lateral motion at the base of each structure, and for the relative roof response.

Figures 3.14 and 3.15 show the average base and roof transfer functions for all the building models considered in this study for the various building types. These figures include the results of both the original and softened soil models, and show the ranges between the minimum and maximum envelopes of all the transfer functions. For reference, these figures also show the first few natural frequencies of vibration of the corresponding rigid-base building model. Recall that for all the systems considered in each set, the foundation-building model is the same. Therefore, the variability observed in the transfer functions in Figures 3.14 and 3.15 involves the changes in the ground motion depending on the location of any given building in the cluster, and the combined action of the individual SSI and the collective SCI effects.

Figure 3.14 shows the variability of the transfer functions of the base motion for each structure type. In each case, the shape of the average transfer functions exhibits the blips and reductions around the natural frequencies discussed before. Both the inertial and kinematic interactions play a role in influencing the base motion and filtering out higher frequencies. On average, the base response experiences a rapid reduction above each natural frequency. These jumps increase with the size of the foundation ($B3 > B2 > B1$). These effects are more conspicuous in the softened soil case, for which the impedance ratio between the foundation and the soil is larger. Notice also that the range of variability is greater for the (stiffer) original soil model and that, in all

cases, the variability increases with the frequency. This is particularly relevant because SSI effects are often associated only with the first mode of vibration. Here, however, the results of the B2 and B3 models suggest that SSI base effects appear to be more significant for the second and higher modes. Figure 3.15 focuses on the variability of the transfer functions for the relative roof response. These results are compared to the transfer functions of the corresponding rigid-base structure. As expected, the natural frequencies of the flexible-soil systems are smaller than those of the rigid-base reference models, and the effective damping increases (as reflected by the smaller resonance amplitudes). These are well-known SSI effects (e.g. Jennings and Bielak, 1973; Veletsos and Meek, 1974), which are more prominent for the shorter buildings (B1) and for the softened soil conditions. There is, however, one exception. The average amplitude at the second mode of the taller buildings (B3) is larger than that of the rigid-base model. This behavior brings to ones attention the fact that SSI may not always play a conservative role in terms of reducing the structural response. Another aspect of interest captured by the transfer functions shown in Figures 3.14 and 3.15 is the increased response and variability with frequency, especially above 3.5 Hz and 2.5 Hz in the B2 and B3 models, respectively. Such an increase has been observed before by Clouteau and Aubry (2001), who concluded that the influence of buildings interaction increases almost linearly with frequency. They also found that the correlation decreases with frequency above the lowest natural frequency of the buildings. This matches our results in Figures 3.14 and 3.15. To help explain the physical meaning of the rapid variability and presence of spikes in Figures 3.14 and 3.15, we have examined the roof displacement due to rocking of the foundation and the relative base displacement of the foundation for the ICB model. We calculated the transfer functions of the roof rocking (D in Figure 3.11) and relative base motion (C in Figure 3.11) with respect to the corresponding free-field motion (B in Figure 3.11) for this model, and found that in addition to the resonant behavior in the vicinity of the response at the natural frequencies, there occur several, more spiked peaks, at a number of frequencies.

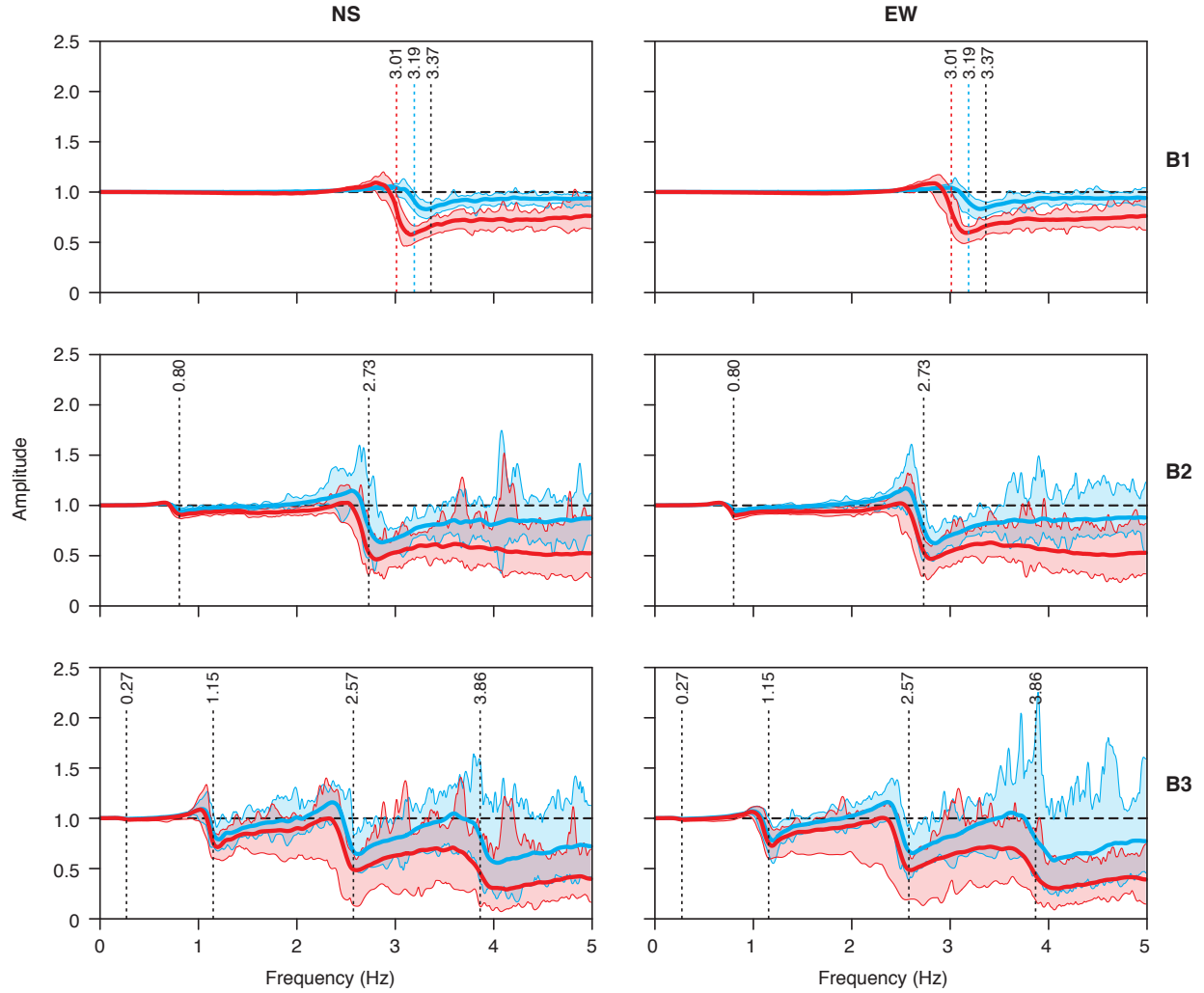


Figure 3.14: Average (thick lines) and maximum and minimum envelopes (thin lines) of the transfer functions between the base and the free-field motions for all the building models in the various cluster and spacing arrangements for the three building types, B1 (top), B2 (middle) and B3 (bottom), in the NS (left) and EW (right) directions. Blue lines correspond to the results obtained using the original soil model and red lines to the results corresponding to the softened soil conditions. Filled areas cover the range from the minimum to the maximum envelopes. The black dashed line indicates the case of no interaction, in which the base motion is equal to the free-field motion. In each frame, the vertical dotted lines mark the natural frequencies of vibration of the rigid-base model for each type of building. In the case of the B1 model, we also indicate the average of the fundamental natural frequency of the flexible-soil systems, as identified from Figure 3.15.

Those peaks become sharper and larger above the resonant frequencies of the system. Going back to the transfer function F_F/B for the relative roof motion, one can see that the same type of sharp peaks present in Figure 3.15, also occur even for the case of a single building (ICB) in the top-right panel of Figure 3.11 at frequencies of about 3.3, 3.75 and 4.2 Hz—although much

smaller. These spikes will appear again at the same frequencies later in Figures 3.16 and 3.17 in the next section, and it will be shown that their amplitude varies with the presence of additional buildings—most likely due to constructive and destructive interference of the waves traveling between the structures. Since Figure 3.15 shows the envelope of all the structures in the various cluster arrangements, the presence of multiple peaks at different frequencies is the result of overimposing all the individual cases for which these spikes occur at different frequencies that depend on the individual impedance between the foundation and the surrounding soil.

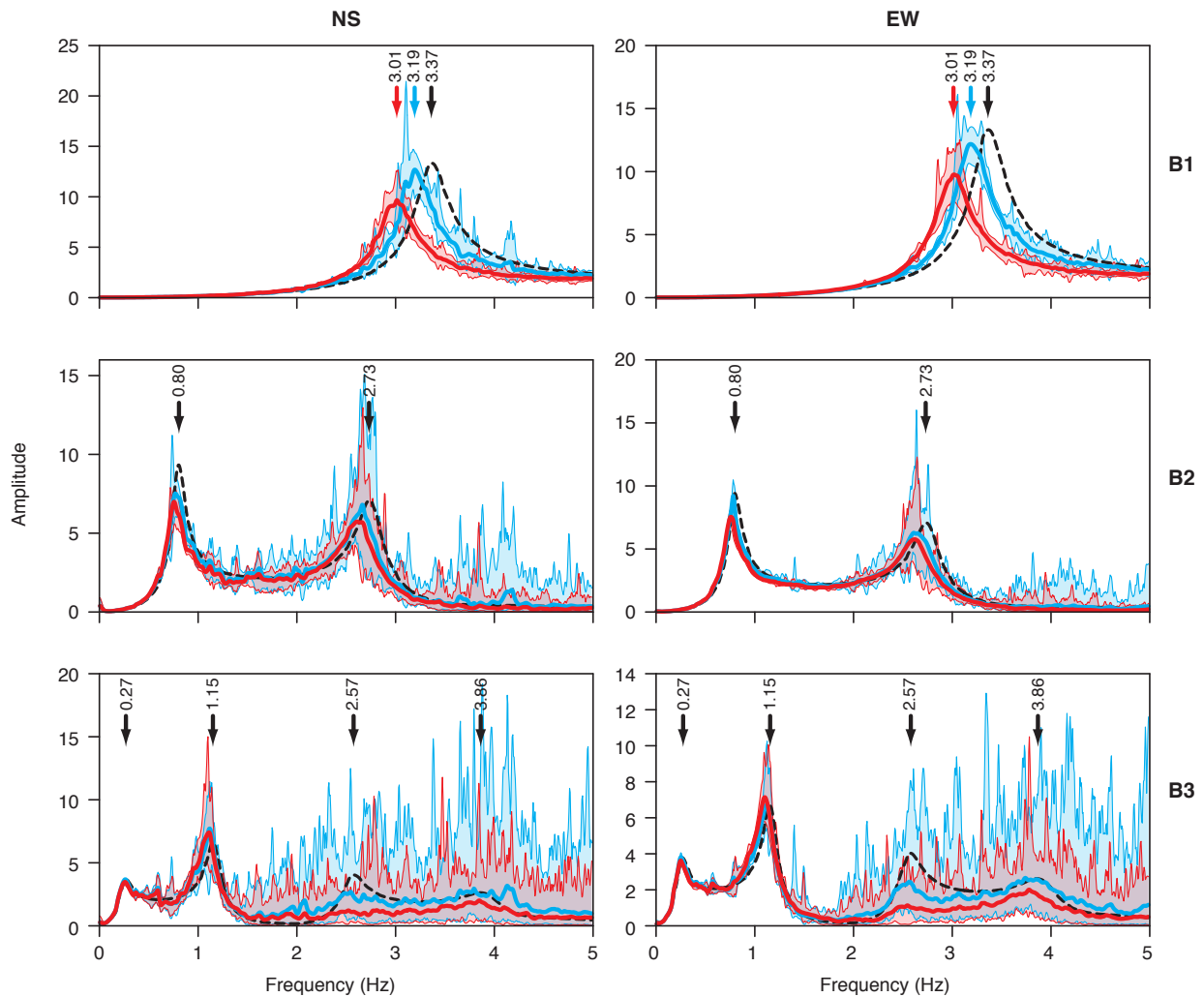


Figure 3.15: Same as Figure 3.14 but for the transfer functions between the relative roof and the free-field motions. Here, the black dashed lines correspond to the transfer functions of the rigid-base models. The black arrows in each frame indicate the natural frequencies of the rigid-base models, and in the case of the B1 models, the colored arrows indicate the average natural frequency of vibration of the flexible-soil systems as identified from the average transfer functions.

We also believe that earlier analyses of records from instrumented buildings may have revealed the presence of a similar increase in the energy content and amplitude variability at the high frequencies. This can be seen, for instance, in the transfer functions of the Hollywood Storage Building in [Duke et al. \(1970, Fig. 13\)](#) and in [Trifunac et al. \(2001, Figs. 8 and 14\)](#). Unfortunately, most studies of SSI effects in instrumented buildings focus only on the lower modes of vibration. Besides, strong motion records are susceptible to increasing noise ratios at the higher frequencies. This makes it difficult to confirm this behavior in observations. In fact, [Duke et al. \(1970\)](#) attributed the occurrence of the spikes to possible computational inaccuracy. However, in the more recent study by [Trifunac et al. \(2001\)](#), one can observe the same kind of behavior for a number of different earthquakes. In the present study, for the case of the rigid base models, the transfer functions for the relative roof response are very smooth, even at high frequencies, for which the energy content of the earthquake ground motions is very small. Thus, given that a highly variable oscillatory behavior of the transfer functions can be observed in the case of the Hollywood Storage building, and given that in our study the spikes appear at high frequencies for the buildings on deformable soils, but not for the rigid-base buildings, it appears that the spikes in [Figures 3.14 and 3.15](#) are due to SSI and SCI effects. For the cases considered here, the increments in the energy and variability at the higher frequencies seem to increase with the number of buildings. This is examined in greater detail in the next section.

SCI Effects on the Transfer Functions of the Control Building

We focus now on the changes due to the collective SCI effects, as opposed to those caused by SSI alone, using the response of the center building (CB) of each cluster. We compare its behavior with that of the corresponding ICB case; that is, the same building but without any other buildings around it. [Figures 3.16 and 3.17](#) show, respectively, the base and relative roof transfer functions with respect to the free-field motion at the same location of the CB for the various building models, cluster arrangements, and separations, including the corresponding transfer functions of the ICB. These results correspond to the simulations done using the softened soil model. In general,

as discussed before, the base transfer functions in Figure 3.16 follow the characteristic peaks and drops (or blips) near the natural frequencies of the building-foundation systems, followed by subsequent reductions. These frequencies are not aligned with the natural frequencies of the site or its surrounding basin in all cases (see Figure 3.7), and in the cases where they are, such alignment does not seem to play a significant role. Therefore, it appears that the blips and reductions in the base transfer functions are related to the geometric and dynamics characteristics of the individual buildings and clusters—as understood from classical SSI studies, and not to the free-field ground motion. Also notice that the base transfer functions obtained from the actual records in the Hollywood Storage Building during various earthquakes match qualitatively well with our findings in this study (see Appendix A), although none of the building + foundation systems we consider here is meant to represent the Hollywood Storage Building or its surrounding soil conditions.

The amplitudes of the transfer functions, however, change with respect to that of the corresponding ICB, depending on the clusters, number of buildings, and separation. In the vicinity of the blip, below and near the fundamental frequency, for instance, the amplitude of the transfer functions corresponding to the CB in the clusters is smaller than that of the ICB and the frequency of the system shifts left. This reduction and shift have been observed before by Clouteau and Aubry (2001). After the local minima, on the other hand, the amplitude of the transfer functions increase and eventually becomes larger than that of the corresponding ICB. For some cases, this means that the reductions in the higher frequencies with respect to the free-field motion are smaller for the CB in the cluster than for the ICB. Lombaert and Clouteau (2006) attribute these changes to the global reduction of the natural frequency of the site due to the added mass of the buildings. This is, in a sense, similar to the effect of the mass of the foundation (here acting as a group) on the amplitude of the blip and shift in the fundamental frequency of the soil-structure system as explained in Jennings and Bielak (1973). In fact, Jennings and Bielak (1973) found that the blips around the natural frequencies of the building-foundation systems represent a dynamic absorber effect and occur even when the base is assumed to have no mass, and the underlying soil is a halfspace, with no associated resonant frequencies. Near the fundamental frequency of vibration

of the SSI system, the changes with respect to the ICB become larger as the number of buildings increases and separation between buildings decreases, especially for the shorter buildings (B1). At the higher modes of vibration, the number of buildings does not have a consistent effect on the transfer functions with respect to that of the ICB, other than significantly increase the variability in the amplitude of the spectral ratios, especially in the case of a set of resonant peaks (or spikes), most notably in the transfer functions of the B2 and B3 models for frequencies above 3 and 2.5 Hz, respectively. These spikes appear to be enhanced by constructive interference of the seismic waves generated by the presence of the building clusters. They are, however, also present in the transfer function of the corresponding ICB at the same frequencies, although much smaller—almost unnoticeable. We identified some of these higher frequency resonance peaks to be related to modes of translation and rocking of the base. Thus it appears that the waves generated by the building clusters influence (and are influenced by) the rocking and translation of the building foundations in the cluster. Overall, the changes in the spectral ratios with respect to the corresponding transfer function of the ICB become consistently smaller as the separation between buildings increases. The largest differences between the spectral ratios in the CB and that of the ICB occur in the S1 arrangements.

The coupled interaction effects of the various building models and arrangements also have an impact on the structural response of the building models. Figure 3.17 shows the relative roof transfer functions of the CB in each cluster with respect to that of the corresponding ICB and the rigid-base model. The following trends are worthy of note in this figure:

- (i) There is no considerable change in the natural frequencies of vibration in the various systems with respect to those of the ICB. Reductions in the frequencies occur only as one moves from the rigid-base model to the flexible-soil systems; that is, changes in the natural frequencies are almost independent of the SCI effects. In a comparison not included here, we found that frequency reductions with respect to the rigid-base models were of the order of 11 and 8 percent in the first and second modes of vibration, but only 1 to 3 percent of the total changes were due to SCI effects. Reductions in the fundamental natural frequencies due to SSI alone

were of the order of 10 percent. These results are of the same order as observations made in the past in instrumented buildings supported on similar soils as those considered here (e.g. Stewart et al., 1999).

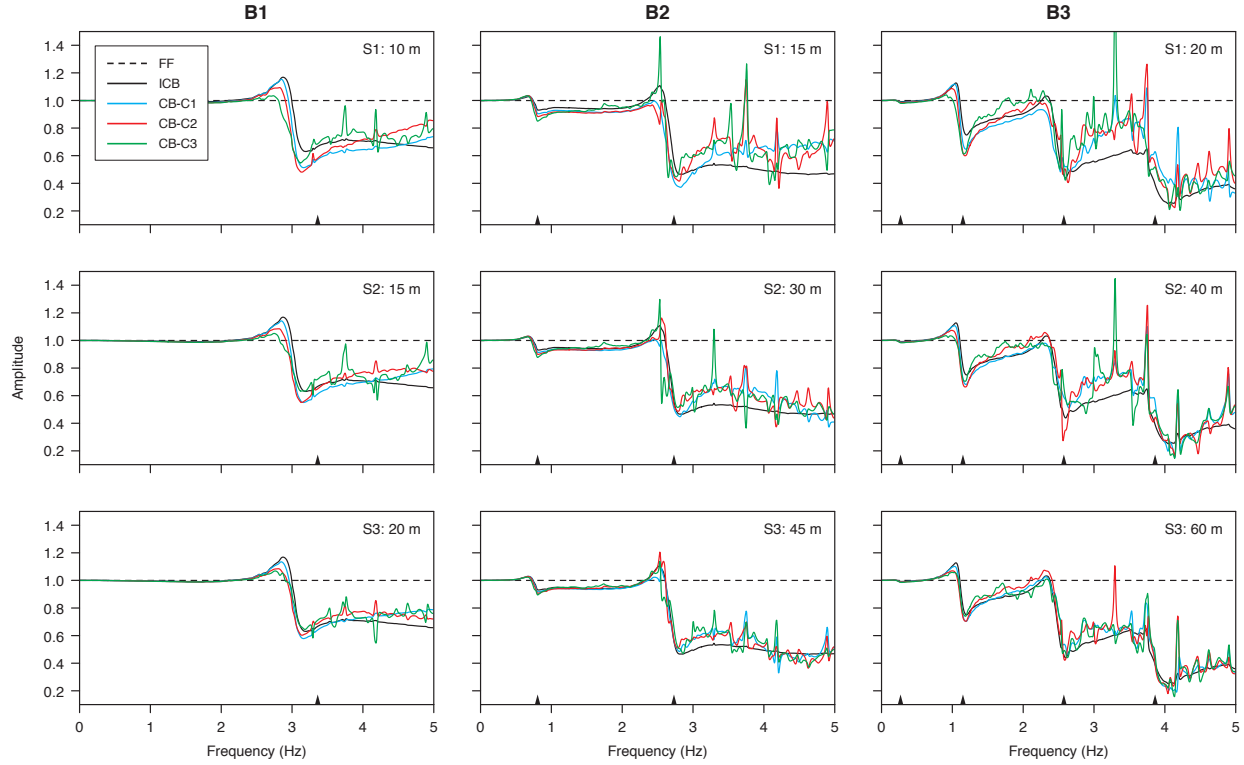


Figure 3.16: Comparisons between the base transfer function of the isolated control building (ICB) (black) and the various transfer functions corresponding to the same building at the center of each cluster (CB) for the arrangements C1 (blue), C2 (red) and C3 (green), the separations S1 (top), S2 (middle) and S3 (bottom), and the building models B1 (left), B2 (center) and B3 (right). The horizontal dashed line indicates no change with respect to the free-field motion. These results correspond to the motion in the EW direction and to the softened soil system.

- (ii) The amplitudes of the spectral ratios in the fundamental mode in the clusters are smaller than in the ICB or in the rigid-base system. These reductions tend to increase with the number of buildings, and are more prominent for the arrangements with smaller separations, especially in the case of the B1 models for which the peak response is about 40 percent smaller than that of the corresponding fixed-base model.

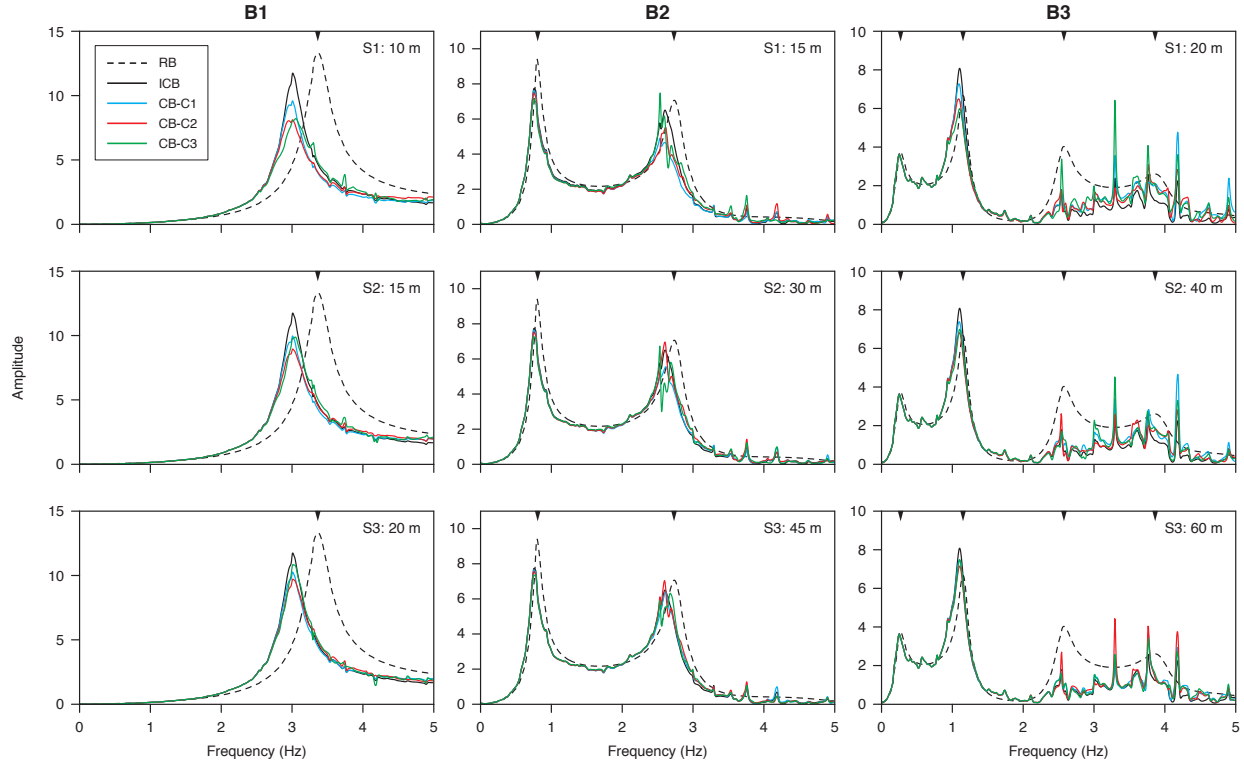


Figure 3.17: Comparisons between the system's relative roof transfer function (with respect to the free-field) of the isolated control building (ICB) (black) and the various transfer functions corresponding to the same building at the center of each cluster (CB) for the arrangements C1 (blue), C2 (red) and C3 (green), the separations S1 (top), S2 (middle) and S3 (bottom), and the building models B1 (left), B2 (center) and B3 (right). The dashed line corresponds to the relative roof transfer function of the rigid-base (RB) system. These results correspond to the motion in the EW direction and to the softened soil system.

- (iii) The changes in the amplitudes of the transfer functions of the taller buildings (B2 and B3) are larger in the second mode of vibration than in the fundamental mode. In addition, they exhibit both reductions and amplifications with respect to that of the ICB, and in the case of the tallest buildings (B3), the change is larger than that of the rigid-base model. These changes do not show a clear link with the number of buildings or the separation between the structures. Most important, the smoothness at the top of the peaks is significantly disrupted (or split). Since these perturbations are not present in the transfer function of the ICB, they must be due to the presence of the other buildings. This indicates coupling between the buildings due to SCI effects. Such coupling effects have been observed in previous studies (e.g. Clouteau and Aubry, 2001; Boutin and Roussillon, 2004; Kham et al., 2006; Semblat

et al., 2008).

- (iv) Resonant frequencies above 3.2 Hz and 2.5 Hz in the taller buildings (B2 and B3, respectively) are significantly enhanced by the presence of the additional structures. A careful look at various spectral ratios reveals that these frequencies are associated with the translational and rotational (rocking) modes of vibration of the base of the flexible soil-structure systems. That is why they are also present in the ICB and not in the rigid-base model. This indicates that the source lies in the characteristics of the individual SSI system. Their amplitude, however, clearly increases with the number of buildings and is more prominent for the denser building arrays (smaller separations). This is particularly visible in the B3 models for the S1 and S2 separations. Notice that these frequencies are consistent with those seen in Figure 3.15.
- (v) Overall, there is a large reduction in the transfer functions of the B3 structures on deformable soil at the higher frequencies with respect to the corresponding function for a rigid base. This implies that for an earthquake with significant high-frequency content, the high-frequency response of the structures on the softened soil system would be greatly reduced compared to that of the structures on a rigid ground.

Although not included here for brevity, we also studied the variation and interaction changes in the amplitude of the roof transfer functions of the natural modes of vibration of the various building types and clusters using both the isolated control building and the fixed-base model as reference. We found that interaction effects tend to reduce the amplitude of the fundamental resonance peak, especially for the softened soil systems, although some amplifications were also present for the buildings on the original (stiffer) soil model. On average, the total changes in the CB with respect to the fixed-base model vary from reductions on the order of 30 percent to amplifications on the order of 10 percent, with maximum reductions on the order of 40 percent for the cases of the buildings on the softest soil in the region of consideration. This margin of changes corresponds to the combined soil-structure and site-city interaction effects. Using the amplitude of the resonance

peaks of the ICB as reference, we found that the maximum changes due only to SCI effects were on the order of 30 percent. In general, the changes just described increase with the number of buildings and are more prominent in building clusters with smaller separations between the structures.

CHAPTER 4

Modeling Torsionally Coupled Buildings

In Chapter 3, we use the same modeling framework introduced by [Taborda \(2010\)](#) to investigate the dynamics of symmetric building clusters during earthquakes. The analogy of the buildings as solid bodies made of homogeneous material is a 3D extension of the same approach used in 2D studies by different authors in the past (e.g. [Wirgin and Bard, 1996](#); [Tsogka and Wirgin, 2003](#); [Kham et al., 2006](#)). While we recognize that these models are not general, they do incorporate both shear and bending effects and can be used as an approximation to characterizing SCI effects. In this sense, we find the present approach—which builds on [Taborda \(2010\)](#); [Taborda and Bielak \(2011b,a\)](#)—to be a step forward.

However, it is well known that asymmetric and symmetric buildings behave differently during earthquakes ([Newmark, 1969](#)). If a structure is asymmetric in plan and/or has an uneven distribution of either mass or stiffness, a lateral seismic load can cause a response in which the torsional and lateral motions of the structure are coupled, since the center of mass and the center of rigidity do not coincide in such buildings. Therefore, in order to investigate the coupling effects of asymmetric building clusters during earthquakes, we perform another parametric study similar to the previous one, but using asymmetric—and also symmetric for comparison—structures this time. Similar to the first case study, the second study is also meant to help gain a global insight rather than investigating the response of individual structures in detail. Based on this, certain assumptions and simplifications are done on the building models, which led to modifications in the mesher and

the solver in Hercules, as explained next.

4.1 Modified Meshing

4.1.1 Nonuniform Distribution of Stiffness in Plan

Torsional coupling occurs if the center of mass and the center of stiffness does not coincide in the building. One way to obtain non-coincident centers is to have buildings with plan irregularities (e.g., those with re-entrant corners such as L-shape plans on corner plots). Yet another simpler way is to have regular shaped buildings with nonuniform stiffness distributions in plan, while keeping density constant. Here, we proceed with the second strategy (non-uniform stiffness distribution in plan). After [Taborda \(2010\)](#), all the finite elements in the structure have identical material seismic velocities (V_S and V_P) and density (ρ). This has changed for this study to allow for variation in the velocity values. Since ρ is kept constant, the mass center is still remained at the geometric center.

4.1.2 Nonuniform Distribution of Stiffness Along Height

With the exception of some low-rise buildings, the assumption of uniform stiffness distribution along height is not valid for most real buildings where, due to the static, live and nonuniform vertical distribution of earthquake-induced lateral forces in buildings, the lateral stiffness at the top of the structure is typically smaller than that at the base of the building ([Miranda and Reyes, 2002](#)). By using the data obtained from forced vibration tests of 8 different buildings in California, [Jennings \(1969\)](#) showed that, as a general rule, most fundamental modes of tall buildings tend to resemble straight lines more nearly than the first mode shapes of either bending beams or shear beams. He also stated that the tall buildings in California have a cross-section that is constant with height, which implies that the mass per story is approximately constant throughout the building. Later, [Bielak \(1969\)](#) showed that a shear beam with uniform cross section and mass density will have a linear first mode if and only if the shearing stiffness is distributed parabolically. Based on

these observations, stiffness of the buildings are decreased along their heights, while keeping the density uniform.

According to [Bielak \(1969\)](#), shearing stiffness should be parabolically distributed such that it reaches a value of zero at the roof level. However, this is not realistic for the case of actual buildings. Therefore in our calculations, the stiffness value at the roof level of the nonhomogeneous structure is made equal to 0.3 times of the stiffness value of the corresponding homogeneous structure. Using this condition and maintaining the total shearing stiffness of the homogeneous structure, the following expression is found for the nonuniform distribution of stiffness in the nonhomogeneous structure. Note that, the stiffness is directly proportional to V_S^2 , not to V_S , which can be inferred from equations (2.2) and (2.5).

$$V_S^2(\bar{z}) = [1.05(1 - \bar{z}^2) + 0.3] V_{S_{hom}}^2 \quad (4.1)$$

In equation (4.1), $V_S(\bar{z})$ is the shear velocity in the nonhomogeneous structure, \bar{z} is the normalized height with respect to the total height of the building (0 at base, 1 at roof), and $V_{S_{hom}}$ is the shear velocity in the corresponding homogeneous structure. To calculate $V_P(\bar{z})$, $V_S(\bar{z})$ is multiplied by the same constant (ratio between V_P and V_S) that is used for the homogeneous structure, so that the Poissons Ratio (ν) stays the same.

Figure 4.1 shows the $V_S^2/V_{S_{hom}}^2$ distributions for both the associated homogeneous and nonhomogeneous structures. It can be seen that the building gets stiffer at the base and becomes more flexible towards to the roof.

4.1.3 Designing Eccentric Structures

In previous studies, it has been shown that the eccentricity (e)—distance between the center of resistance (CR) and the center of mass (CM)—and the ratio between the uncoupled torsional (ω_θ) and uncoupled translational (ω_v) natural frequencies ($\omega_\theta/\omega_v = \Omega$) are the two main controlling parameters affecting the torsional coupling. In order to examine the influence of these parameters

on SCI effects, we design buildings with different normalized eccentricities (e/r) for given Ω values, where r is the radius of gyration about the mass center. Only one-way coupled buildings are used in this study. Direction of the eccentricity can be determined by user input. Also for convenience, the buildings-foundation systems are forced to have same-sized finite elements.

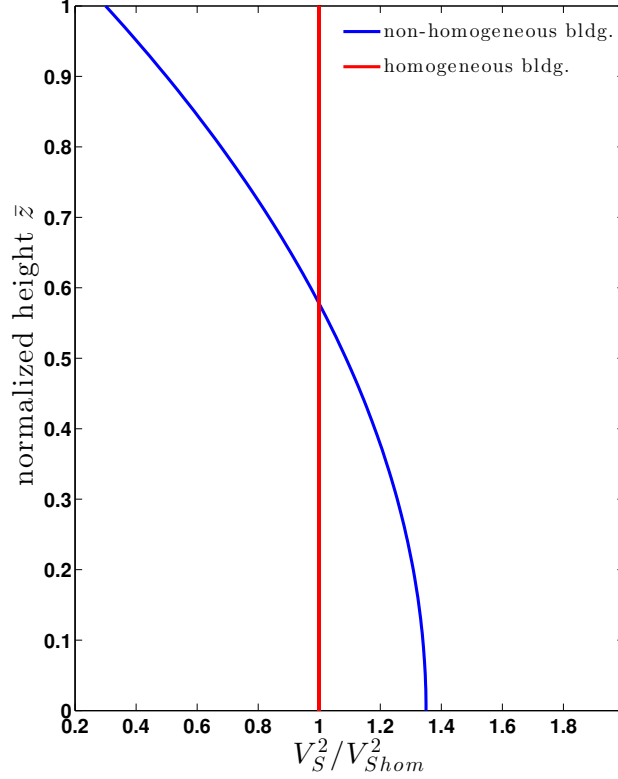


Figure 4.1: Distribution of V_S^2/V_{Shom}^2 for homogeneous and nonhomogeneous structures along height. Note that $\bar{z} = 0$ at the base level, and $\bar{z} = 1$ at the roof level.

In our calculations, ω_θ is assumed to be the frequency of vibration when the centre of mass is constrained to remain stationary. It is obtained by applying a pure rotation (around center of mass) at the fixed base of the building and recording the fundamental frequency at the roof level. Similarly, ω_v is obtained by constraining the system so that rotation is prevented around the center of mass. Pure translation is applied at the fixed base then, in order to obtain the uncoupled translational frequency (ω_v).

The center of resistance (CR) of a single-story system is the point on the rigid deck through which the application of a horizontal static force causes pure translation of the deck without any

rotation. Also, a static torsional moment about a vertical axis causes pure rotation of the floor about the vertical axis passing through the CR (Hejal, 1987). Any of these two definitions can be used to determine the location of CR. As mentioned earlier, in our calculations ρ is kept uniform, thus the center of mass (CM) is located at the position of the geometric center.

Figure 4.2 illustrates how the asymmetric buildings are designed. Each level in the building is divided into 6 different parts. Area (A_i), V_{Si} , V_{Pi} and ρ_i values are given as input parameters for each part ($i = 1$ to 6). To design different asymmetric structures for a given Ω , first V_{Si} and A_i are determined for the given eccentricity value by keeping the values of total translational stiffness and Ω the same as the symmetric building's. Then, V_{Pi} can be determined by multiplying V_{Si} with the $V_{P_{sym}}/V_{S_{sym}}$ ratio of the symmetric structure. The same ρ value is used regardless of the eccentricity value. The same procedure can be followed to obtain other symmetric structures with different Ω values (but with the same uncoupled translational fundamental natural frequency).

Since only one-way asymmetric structures are investigated, $A_5 = A_6$, and similarly $V_{S5} = V_{S6}$. These values are adjusted based on the value of Ω .

This procedure, however, requires a lot of trial errors and is an arduous task unless some simple expressions are obtained. Using the above-mentioned definitions of CR, it can be shown that (Hejal, 1987)

$$e = \frac{\sum_i x_i k_{yi}}{\sum_i k_{yi}}. \quad (4.2)$$

As mentioned earlier, the stiffness (k_{yi}) is directly proportional to V_{Si}^2 , and also to the area (A_i). So equation (4.2) can be rewritten as:

$$e = \frac{\sum_i x_i V_{Si}^2 A_i}{\sum_i V_{Si}^2 A_i}. \quad (4.3)$$

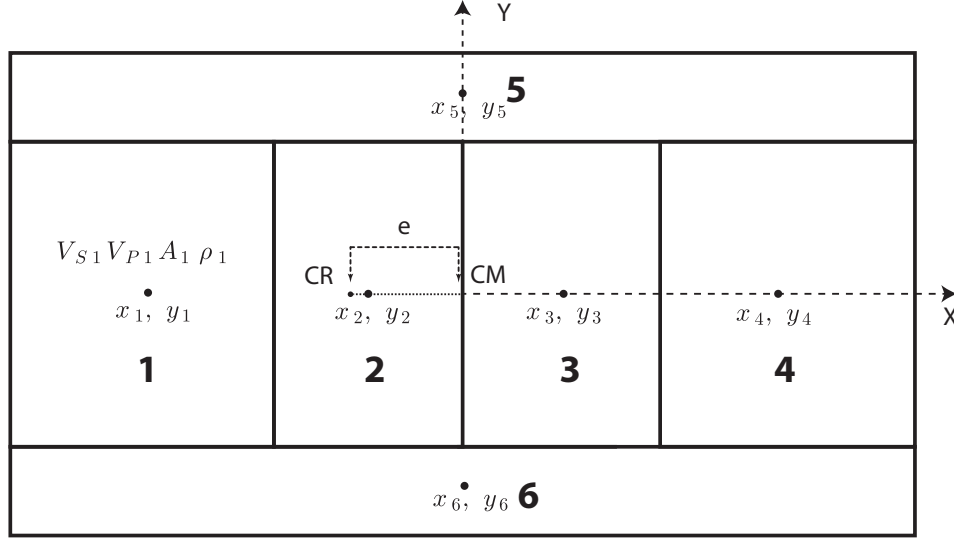


Figure 4.2: This figure shows how asymmetric structures are designed. Building's plan section is divided into 6 parts. CM is the center of mass, CR is the center of resistance, and e is the eccentricity. Only one-way eccentricity is assumed. In this case, the eccentricity is perpendicular to the y direction. A_i , V_{Si} , V_{Pi} values are determined depending on the values of e and Ω , and given as input parameters for $i = 1$ to 6.

In addition, the total translational stiffness is constrained as follows.

$$\sum_i V_{Si-sym}^2 A_i = \sum_i V_{Si}^2 A_i \quad (4.4)$$

In equation (4.4), V_{Si-sym} is the shear velocity in the associated symmetric building.

Since the total translational stiffness is maintained, it is appropriate to maintain the total torsional stiffness as well in order to obtain buildings that share the same Ω value. Assuming that torsional stiffness is calculated around the CM, this is achieved by (i) using the same A_i values, (ii) using the same ratio $V_{S1}/V_{S2} = V_{S4}/V_{S3} = \text{Constant}$ and (iii) using the same $V_{S5} = V_{S6}$ values for each structure with a given Ω .

Using the above-mentioned expressions, buildings with the same Ω but different e/r values can be designed for a particular structure model (i.e. see B1, B2, B3 in Chapter 5). Plus, each building belonging to a particular model has the same total translational stiffness. However, since V_{Si} and A_i values can not be negative (plus V_{Si} should be big enough for numerical stability), and also the smallest A_i value is determined by the building's element size, there are always upper and lower

bounds on the possible Ω and e/r values, which by necessity, limit the cases considered in this study.

4.2 Constrained Displacements

In earthquake engineering, it is usually assumed that each floor diaphragm is rigid in its own plane but is flexible in the transverse direction, which is a reasonable representation of the true floor system behavior (Clough and Penzien, 2003). Moreover, most of the early studies that investigated the torsional coupling effects used structures that are shear-beam type, or extension of it in 3D (e.g. Hoerner, 1971; Kuo, 1974; Tso and Dempsey, 1980). Based on these, modifications are done on the building models so that each level deforms as a rigid body. Different building types can be obtained by manipulating these dof. Some of them are explained as follows.

4.2.1 Most General Constrained Model

For this case, each level in the building+foundation system is allowed to deform as a rigid body that has 6 degrees of freedom (dof) as seen in Figure 4.3. These dof are $u_o(z)$, $v_o(z)$, $w_o(z)$, $\theta_x(z)$, $\theta_y(z)$ and $\theta_z(z)$ (translations and rotations along x,y and z, respectively) and are defined at the center of mass (CM) which is located at the geometric center. These displacements depend on z since they differ at each level of the building (there is a total of $6 \times N$ dof in the building+foundation system, where N is the total number of levels). To find these dof, one alternative is to modify the stiffness matrix for the system and do the calculations accordingly. However, since this is not a straightforward task in Hercules, we came up with another strategy. That is, at the end of each time step, we find approximate average values for these dof by taking into account all the nodal displacements at the same level. Then, before the next time step calculations start, all displacements in the building+foundation system are updated based on these average dof values (equation (4.5)).

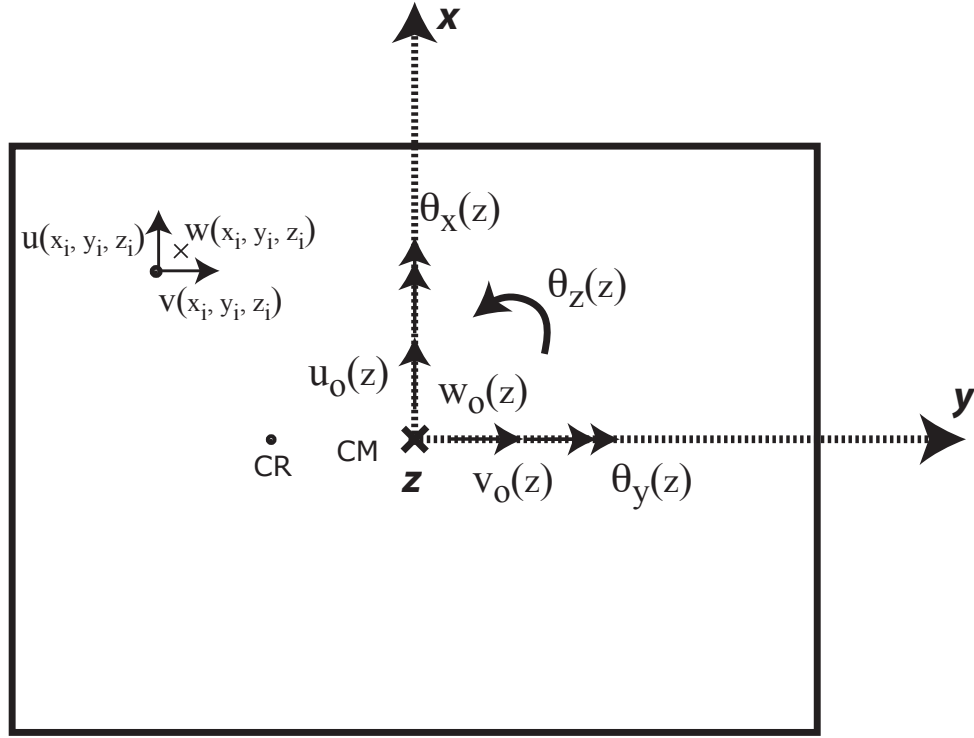


Figure 4.3: There are 6 degrees of freedom(dof) defined at the CM (center of mass) for each level in the building+foundation system ($u_o(z)$, $v_o(z)$, $w_o(z)$, $\theta_x(z)$, $\theta_y(z)$ and $\theta_z(z)$). Displacement of any point in the system ($u(x, y, z)$, $v(x, y, z)$ and $w(x, y, z)$) can be calculated using these dof based on the rigid body assumption. z -axis can be imagined as going "into the the page". CR is the center of resistance, and CM is located at the center of the rectangle.

Assuming rigid body deformation and small displacements at each level, the constrained translational displacements ($u(x, y, z)$, $v(x, y, z)$ and $w(x, y, z)$ in the x , y and z directions, respectively) can be calculated as follows for any point at a given height in the building.

$$u(x, y, z) = u_o(z) + y\theta_z(z)$$

$$v(x, y, z) = v_o(z) - x\theta_z(z) \quad (4.5)$$

$$w(x, y, z) = w_o(z) + y\theta_x(z) - x\theta_y(z)$$

Note that $\theta_z(z)$ represents the torsional rotation around the CM, and $\theta_x(z)$ and $\theta_y(z)$ represents

the rocking motions around their associated directions.

Thus, calculating the updated displacements $u(x, y, z)$, $v(x, y, z)$ and $w(x, y, z)$ entails knowing the 6 average dof defined at the CM. The average translational dof at the CM ($u_o(z)$, $v_o(z)$ and $w_o(z)$) are calculated as follows.

$$\begin{aligned}
 u_o(z)A_t &= \int_A u_{old}(x, y, z)dA \\
 v_o(z)A_t &= \int_A v_{old}(x, y, z)dA \\
 w_o(z)A_t &= \int_A w_{old}(x, y, z)dA
 \end{aligned} \tag{4.6}$$

In (4.6), A_t is the total area of the building's cross section, and $u_{old}(x, y, z)$, $v_{old}(x, y, z)$ and $w_{old}(x, y, z)$ are the displacements calculated by equation (2.10). They are updated by the constrained values at the end of each time step (equation (4.5)).

Similar approach can be followed in order to calculate the average rotations around the CM. First, calculations for the average $\theta_z(z)$ are shown. For this, twisting moments around the CM due to the displacements along x-axis are equated to each other.

$$\begin{aligned}
 M_{uy}(z) &= \int_A y u_{old}(x, y, z)dA \\
 &= \int_A y u(x, y, z)dA = \int_A y (u_o(z) + y\theta_z(z))dA \\
 &= \underbrace{\int_A y u_o(z)dA}_{M_{oy} \rightarrow 0} + \underbrace{\int_A y^2 \theta_z(z)dA}_{I_x \theta_z(z)}
 \end{aligned} \tag{4.7}$$

$$\theta_z(z)_{uy} = \frac{M_{uy}(z)}{I_x} \tag{4.8}$$

In equation (4.7), M_{oy} vanishes since the origin of the coordinate system is at the center of geometry. I_x is the the second moment of area with respect to the x-axis.

Similar calculations can be repeated for moments due to the displacements along the y-axis, and the following expressions can be found (details are omitted)

$$M_{vx}(z) = \int_A x v_{old}(x, y, z) dA \quad (4.9)$$

$$\theta_z(z)_{vx} = \frac{-M_{vx}(z)}{I_y} \quad (4.10)$$

in which I_y is the the second moment of area with respect to the y-axis.

Taking the average of equations (4.8) and (4.10) yields the final form of the average $\theta_z(z)$.

$$\theta_z(z) = \frac{\theta_z(z)_{uy} + \theta_z(z)_{vx}}{2} = \frac{M_{uy}(z)}{2I_x} + \frac{-M_{vx}(z)}{2I_y} \quad (4.11)$$

On the other hand, the average $\theta_x(z)$ is calculated as follows.

$$\begin{aligned} M_{wy}(z) &= \int_A y w_{old}(x, y, z) dA \\ &= \int_A y w(x, y, z) dA = \int_A y (w_o(z) + y\theta_x(z) - x\theta_y(z)) dA \\ &= \underbrace{\int_A y w_o(z) dA}_{M_{owy} \rightarrow 0} + \underbrace{\int_A xy\theta_y(z) dA}_{I_{xy}\theta_y(z) \rightarrow 0} - \underbrace{\int_A y^2\theta_x(z) dA}_{I_x\theta_x(z)} \end{aligned} \quad (4.12)$$

$$\theta_x(z) = \frac{M_{wy}(z)}{I_x} \quad (4.13)$$

Similarly, the average $\theta_y(z)$ is calculated as follows.

$$\begin{aligned}
M_{wx}(z) &= \int_A xw_{old}(x, y, z)dA \\
&= \int_A xw(x, y, z)dA = \int_A x(w_o(z) + y\theta_x(z) - x\theta_y(z))dA \\
&= \underbrace{\int_A xw_o(z)dA}_{M_{owx} \rightarrow 0} + \underbrace{\int_A xy\theta_x(z)dA}_{I_{xy}\theta_x(z) \rightarrow 0} - \underbrace{\int_A x^2\theta_y(z)dA}_{I_y\theta_y(z)}
\end{aligned} \tag{4.14}$$

$$\theta_y(z) = \frac{-M_{wx}(z)}{I_y} \tag{4.15}$$

At the end of each time step, equations (4.6), (4.11), (4.13) and (4.15) are used to calculate the average values of the dof defined at the CM at each level. Then, these 6 values are used to update the nodal displacements at each level in the building using equation (4.5).

This model accounts naturally for both shear and bending effects. However, further simplifications can be done to obtain new building types, such as 3D shear buildings.

4.2.2 Shear Buildings

As mentioned earlier, in most of the previous studies, torsional coupling effects have been studied using structures that are shear-beam type, or extension of it in 3D (e.g. Hoerner, 1971; Kuo, 1974; Tso and Dempsey, 1980). In this study, so-called 3D shear buildings are obtained by setting the values of $\theta_x(z)$ and $\theta_y(z)$ equal to zero. Therefore, for these buildings there are only 4 dof for each level.

One advantage of studying shear buildings is that they can simplify the analysis while investigating the influence of torsional coupling on the combined effects of SSI+SCI. Plus they can provide baseline information even before studying the problem using more realistic building models.

The second advantage arises due to their distinctive dynamic properties. For a rectangular

structure with mass and stiffness uniformly distributed over the plan area, the translational and the torsional fundamental frequencies are equal to each other (Newmark, 1969). This implies that $\Omega = 1$ for the uniform structure. This property is especially important in our case since torsional coupling effects increase as Ω approaches to 1. Therefore, using these models, we will be able to study buildings with $\Omega = 1$, which otherwise might be difficult to attain due to the limitations on the possible Ω values (see section 4.1.3). As a matter of fact, for the general building model that allows bending deformations, Ω is usually larger than 1 if realistic building dimensions are used. This makes it highly unlikely to design building models with $\Omega = 1$ using the procedures explained in section 4.1.3.

One limitation of this model is that base rocking, which is important for SSI, is also restrained. However, restraining rocking will enable us to isolate the coupling effects of SSI due to translational motion only. Then by comparing these results with the ones obtained using shear buildings that allow base rocking, we will in the future also be able to isolate the influence of base rocking on SSI.

CHAPTER 5

Case Study II : Site-City Interaction Using Torsionally Coupled Buildings

In the case study in Chapter 3, we considered only symmetric building models. These models can experience torsional motion only if the input motion includes rotations. While such rotations are implicitly included in our simulations, there we focused only on the lateral motion of the building models. Here, we want to examine torsional effects by using asymmetric building models.

We use the same simulation methods and tools that are used in Chapter 3. That is, we conduct a series of numerical simulations that synthesize the earthquake source and the coupled response of idealized building clusters; and we pay particular attention to the building at the center of each cluster, which we use as reference throughout our analysis. We compare the response of the center building with that of an identical building located at the same site, but with no other buildings present. This allows us to separate the site-city effects for this building from those solely due to soil-structure interaction. However, in contrast to the symmetric buildings studied earlier, particular emphasis is placed here on understanding the torsional effects that are coupled with SSI + SCI. This is done by comparing the SSI+SCI responses of otherwise identical buildings with different eccentricities.

As in Chapter 3, we begin by modeling the 1994 Northridge earthquake and describing the

ground motion in the Simi Valley, with emphasis in the smaller area of interest that contains the building clusters. Note that the subregion of interest has changed for this study. We considered this particular region as it contains softer soils than in our previous simulations. We perform a parametric study that includes different separations, numbers of structures, eccentricities (e) and corresponding uncoupled natural frequency ratios (Ω) for three building models with different fundamental natural frequencies. We use the modified building types (see Chapter 4) to represent the main dynamic properties of buildings including torsion. Similar to the first study, we also consider two soil conditions, original and softened, in order to simulate approximately the effect of soil nonlinearity on the response of the soil-structure systems.

5.1 Building Models

We use shear buildings which have 4 degrees of freedom (dof) per level. A schematic representation of the plan level of such a building is shown in Figure 5.1. We consider the same three building models, B1, B2, and B3, to represent structures of approximately 3, 13, and 40 stories, respectively. This time, however, we assume that interstory height varies between 3 and 4 m, and we define the nominal fundamental natural periods using the approximate fundamental period formula given in ASCE 7-05. As a result, the nominal fundamental periods of the three structure types are set as 0.4, 1.18, and 4.0 s. For each general structure type, we consider two subtypes with different uncoupled torsional fundamental natural frequencies (Ω_1 and Ω_2 , $\omega_\theta/\omega_v=\Omega$). Then for each of these subtypes, we design three different asymmetric structures that have eccentricities e_0 , e_1 , and e_2 . Note that e_0 corresponds to the symmetric structure. Therefore, for each general structure type (B1, B2, and B3), we consider 6 different structures with the same uncoupled translational fundamental natural frequency (ω_v or f_v) but different uncoupled torsional fundamental natural frequencies (ω_θ or f_θ) and normalized eccentricities ($\bar{e}=e/r$), where r is the radius of gyration of the cross section about the CM. So there is a total of 18 different structures that we study in detail. We set $\Omega_1 = 1.0$ and $\Omega_2 = 1.3$. The foundations depths were chosen based on an approximate number of underground

stories (1, 2, and 4 for B1, B2 and B3, respectively), and their mechanical properties defined assuming that the foundations are significantly stiffer than their superstructures. For each structure considered in this study, we set $h = 1.5w$ (Figure 5.1), and place the eccentricity perpendicular to the long dimension.

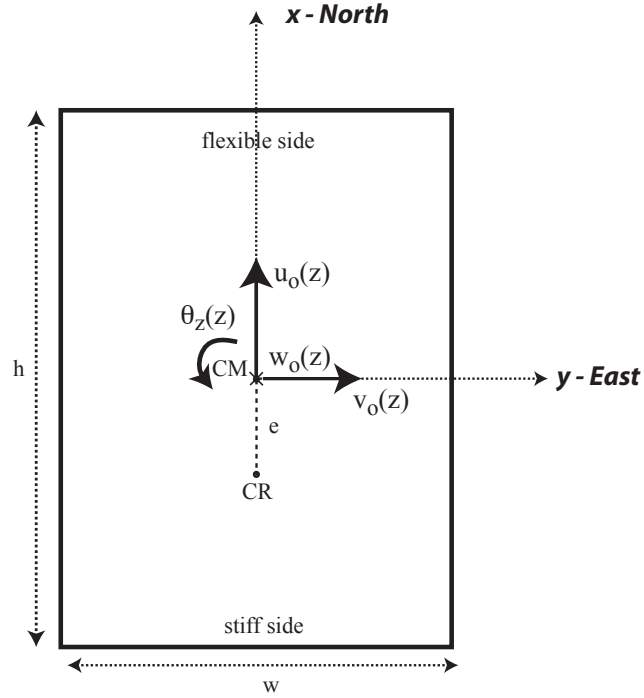


Figure 5.1: Figure shows the schematic representation of the plan of a shear building. For shear buildings, there are 4 degrees of freedom(dof) defined at the CM (center of mass) for each level in the building+foundation system ($u_o(z)$, $v_o(z)$, $w_o(z)$, $\theta_z(z)$). Rocking rotations are restrained. z-axis can be imagined as going "into the the page". CR is the center of resistance, e is the eccentricity, and the CM is located at the center of the rectangle. h and w are the plan dimensions.

We define the material properties of each building type in the following manner. As explained in Chapter 4, the uniform shear building has $\Omega = 1.0$. First, we adjust the value of V_S of the uniform structure so that the actual fixed-base fundamental period of the building model comes close to the nominal one. Then, we design the other associated asymmetric buildings using the procedures explained in Chapter 4 based on the V_S value of the uniform structure. We choose the normalized eccentricity values as $\bar{e}_0 = 0$, $\bar{e}_1 = 0.3$, and $\bar{e}_2 = 0.6$ for Ω_1 ($\Omega = 1.0$). Similarly, we design the symmetric and the corresponding asymmetric structures for Ω_2 ($\Omega = 1.3$) as well. In this case, even the symmetric structure has nonuniform stiffness distribution. The normalized eccentricity values

for Ω_2 are chosen as $\bar{e}_0 = 0$, $\bar{e}_1 = 0.2$, and $\bar{e}_2 = 0.4$. In all cases, we obtain 6 V_S values for the different parts seen in Figure 4.2. Note that these V_S values apply to the homogeneous building which has no stiffness variation along its height. Later, as explained in Chapter 4, these values are used in equation (4.1) in order to find the stiffness values in the corresponding nonhomogeneous structure with a parabolic stiffness distribution with height so that the fundamental modes of the structures are almost linear with height. Material attenuation is considered in the elements of the building models in the form of Rayleigh damping, which is set equal to 5 percent of the critical value for the frequency range used in the simulation Bielak et al. (1999). Table 5.1 shows the height and base dimensions, and the actual fixed base and flexible soil fundamental natural frequencies of the three building models, plus the material properties of the finite elements used to build the block-models. However, material velocity and flexible soil frequency values are given only for the uniform structures in each case, for brevity.

Table 5.1: Dimensions and fundamental period and frequencies of both the rigid-base and flexible-soil building models, and mechanical properties of the finite elements used in the building and foundation blocks. ICB refers to Isolated Control Building. Material velocity and flexible soil frequency values are for the uniform buildings only. r is the radius of gyration of the cross section about the CM. Note that V_P is not given, since it is not applicable for shear buildings.

Type	Height (m)	Found. Depth (m)	Base Size (m × m)	Rigid Base Fund. Nat. Period (s)	Fund. Nat. Freq. (Hz)			V_S (m/s)	ρ (kg/m ³)	r (m)
					Fixed Base	SSI for ICB				
						Orig. Soil	Mod. Soil			
B1	15	5	15 × 10	0.4	2.5	2.45	2.39	138	300	5.20
B2	45	10	30 × 20	1.18	0.85	0.84	0.83	140	300	10.41
B3	150	15	45 × 30	4.0	0.25	0.25	0.24	138	300	15.61
Foundation								750	300	

Also note that V_P becomes irrelevant for these types of shear buildings where bending deformations are restrained. The fundamental translational (f_v) and torsional (f_θ) natural frequencies of each structure type are shown in Table 5.2 for two different Ω values. Different normalized ec-

centricity values considered are summarized in Table 5.3. Table 5.3 can also be viewed as the list of the 6 different buildings considered for each structure type (B1, B2 and B3). When analyzing the results, behavior of different asymmetric structures (structures having different \bar{e} values) are compared for a given Ω and structure type, in order to assess torsional coupling effects.

Table 5.2: Fundamental translational (f_v) and torsional (f_θ) natural frequencies of each structure type for different Ω s (f_θ/f_v).

Building Type	$\Omega_1 = 1.0$		$\Omega_2 = 1.3$	
	f_v (Hz)	f_θ (Hz)	f_v (Hz)	f_θ (Hz)
B1	2.5	2.5	2.5	3.25
B2	0.85	0.85	0.85	1.105
B3	0.25	0.25	0.25	0.325

Table 5.3: Description of the different building eccentricities. \bar{e} is the normalized eccentricity with respect to the radius of gyration of the cross section about the CM (r). $\Omega = f_\theta/f_v$.

Uncoupled Freq. Ratio (Ω)	\bar{e}_0 (e_0/r)	\bar{e}_1 (e_1/r)	\bar{e}_2 (e_2/r)
$\Omega_1 = 1.0$	0	0.3	0.6
$\Omega_2 = 1.3$	0	0.2	0.4

5.2 Earthquake and Regional Simulation

Similar to the first case study, we consider the ground motion of the M_w 6.7 1994 Northridge, California, earthquake as the seismic excitation. In Step I, we simulate the ground motion during the earthquake in a volume domain of $81.92 \text{ km} \times 81.92 \text{ km} \times 40.96 \text{ km}$ that includes the entire San Fernando Valley and some of the Los Angeles metropolitan area. Figure 3.1 of Chapter 3 shows the region of interest, the simulation domain, the fault plane, and the earthquake source model's distribution of the total slip. This model corresponds to the extended kinematic fault rupture pro-

posed by [Graves and Pitarka \(2010\)](#). Using Hercules, we build a FE mesh of the simulation domain tailored to a minimum shear wave velocity, $V_{Smin} = 100$ m/s and a maximum frequency, $f_{max} = 5$ Hz. Here, the elastic material properties of the individual elements were determined from the Community Velocity Model of the Southern California Earthquake Center (CVM-S), version 4.1. Other details related to the earthquake and the regional simulation can be found in section 3.2 of Chapter 3.

5.3 Subregion of Interest and Building Clusters

In Step II, we focus our attention on a subdomain of $1.28 \text{ km} \times 1.28 \text{ km}$, as shown in Figure 5.2. Note that we have changed the location of the DRM region (to Simi Valley) and reduced the domain size significantly. As can be seen in Figure 5.2, shear velocity distribution is fairly uniform throughout this new region. We consider the behavior of various building clusters in the smaller area shown in the Figure 5.2, which consist of regular $N \times N$ buildings, where $N = 1, 3$, and 7 for all the 18 building models described earlier. The special case of a single building, $N = 1$, is hereafter referred to as the isolated control building (ICB), and the clusters with $N = 3, 7$ are identified as C1 and C2, respectively. In addition, each cluster is examined using two different separations, S1, S2, between the buildings. The characteristics of the different building clusters and separations are described in Tables 5.4 and 5.5. Note that buildings are very closely spaced in the clusters with S1 separation. Similar to the first study, Figure 3.3 illustrates a typical building cluster and the simulation domains for Steps I and II. Notice that the center building, denoted here as CB, remains at the same location as the ICB for all the arrangements, but includes the interaction effects with the surrounding structures. The CB and the ICB are used in this study to help differentiate the collective SCI from the individual SSI effects as we vary the building cluster arrangements. We use regular building clusters as opposed to more realistic (random) city-like arrangements, as we are interested mainly in estimating the effect of various parameters such as the number of structures and separation between them on the torsionally coupled response of these systems.

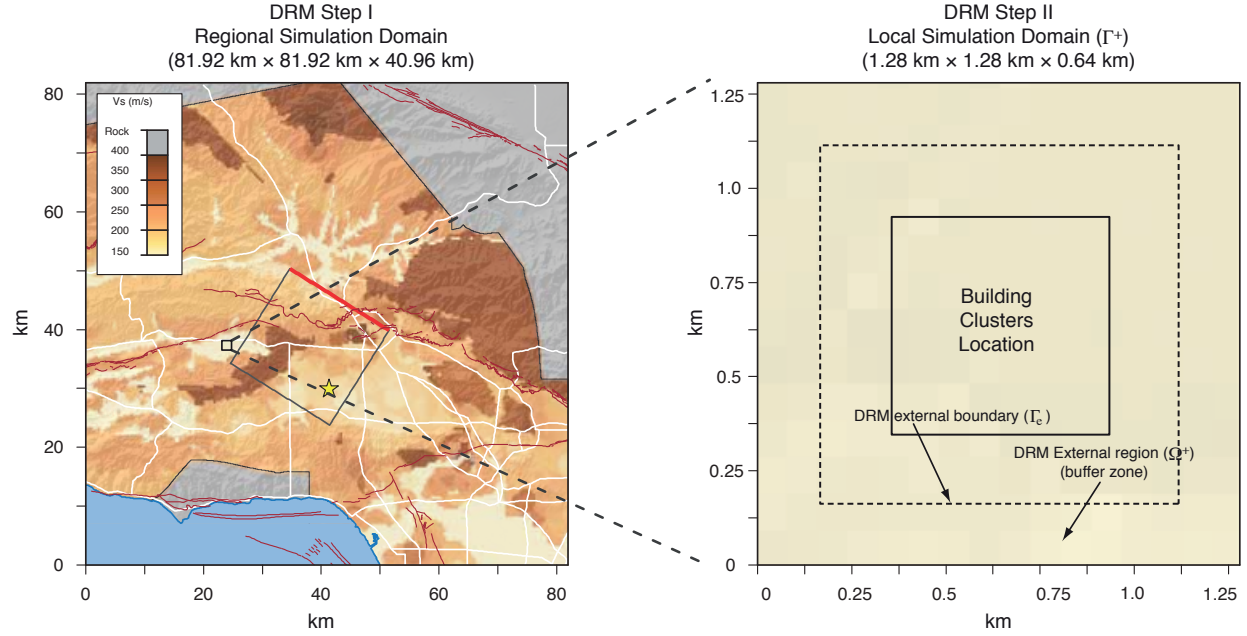


Figure 5.2: (Left) Regional simulation domain used and (right) detail of the local sub-region of interest. The location of the fault plane and the building clusters area are outlined in black lines. The epicenter of the 1994 Northridge earthquake is indicated by a star. The background shows the shear wave velocity at the free surface corresponding to the CVM-S model

Table 5.4: Description of the different building clusters.

Cluster Type	Arrangement	Total Number of Buildings
ICB	1×1	1
C1	3×3	9
C2	7×7	49

Table 5.5: Separation considered for the different spatial distribution of building clusters.

Building Type	Fixed-base		Separation (m)	
	Nat. Period (s)	Nat. Freq. (Hz)	S1	S2
B1	0.40	2.50	1.25	5
B2	1.25	0.80	2.5	10
B3	3.70	0.27	5	20

5.3.1 Softened Soil Conditions

It is widely accepted that the Northridge earthquake produced widespread nonlinear soil behavior in the Los Angeles and San Fernando basins (e.g. [Trifunac and Todorovska, 1996](#); [Field et al., 1997](#); [Beresnev et al., 1998](#)). We were therefore motivated to consider an additional set of simulations under conditions that might resemble the changes in soil stiffness and effective damping due to nonlinearity. This, in turn, will allow us to investigate the effect of the soil properties on the behavior of the individual and collective response of the soil-structure systems and their interaction with the ground motion. To simulate the nonlinear soil behavior, we use equivalent reduced shear moduli and increased damping ratios in soft-soil deposits in the DRM region and perform a second set of simulations only within the reduced domain for all the possible combinations of building models and cluster arrangements. We refer to the first set of simulations that use the CVM-S material properties as the simulations under original soil conditions, and to the second set, which uses the modified shear moduli and damping ratios, as the simulations under modified or softened soil conditions. Other details can be found in section [3.3.1](#).

The differences between the original and softened soil models in terms of the profiles of shear wave velocity and damping ratio beneath the region of interest are illustrated in Figure [5.3](#). The left panel compares the V_S profiles for both models in the first 200 m beneath the free surface in the building cluster area, and the right panel compares the damping. Unlike the region considered in the first case, there is no lateral variation in V_S and damping throughout this new region of interest. Notice that the modifications introduced in the softened soil model only affect the upper 150 m. The maximum reductions in V_S occur near the surface, with average values decreasing from 160 to 100 m/s. Notice, however, that for both soil conditions, V_S falls below 300 m/s only within the top 30 m of soil. Damping is significantly increased at different depths, with values increasing up to 18 percent of the critical damping. Also note that this new region in the Simi Valley has softer soil deposits than the region considered in the first study (San Fernando Valley).

5.3.2 Computational Effort and Performance

Simulations were run in Kraken at the U.S. National Institute for Computational Sciences. Kraken is a Cray XT5 supercomputer with 112,896 cores distributed on 9,408 compute nodes. Details related to the computational effort and performance are included in Table C.1 in the Appendix C.

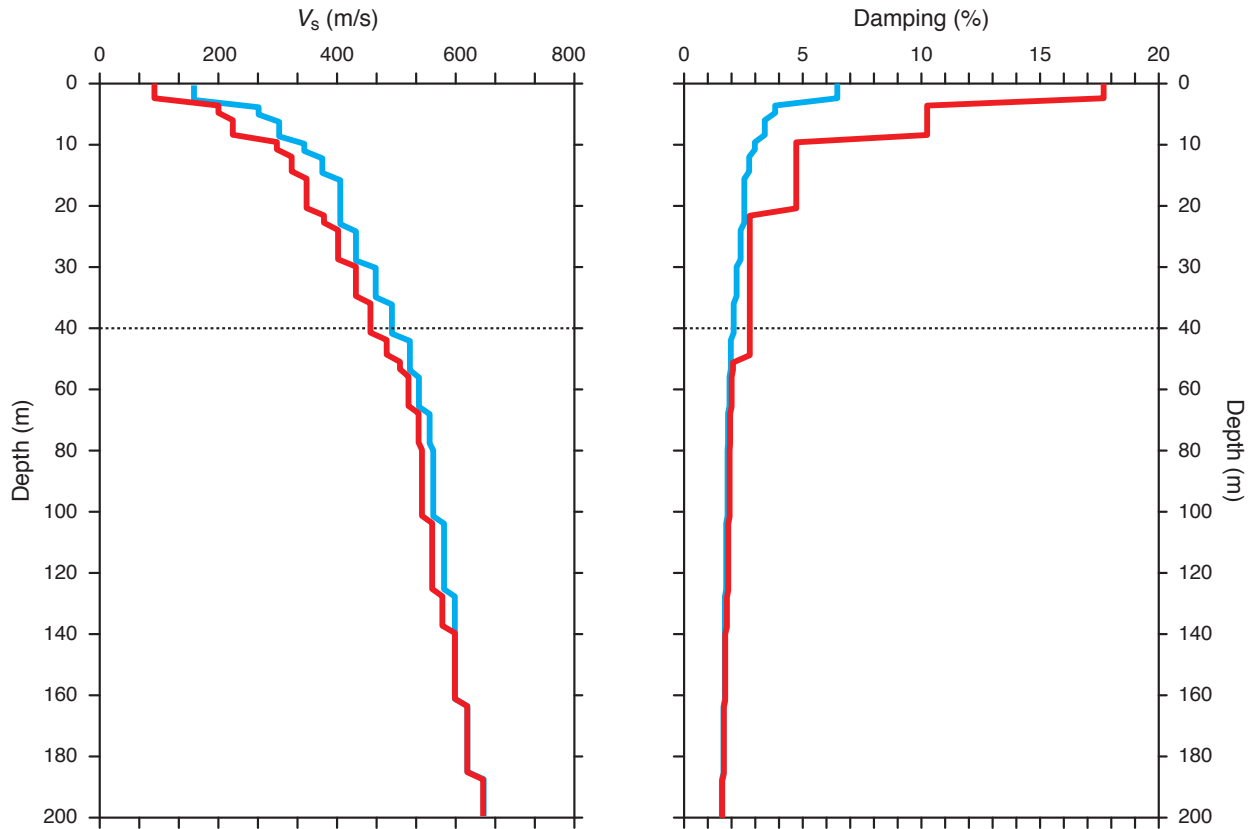


Figure 5.3: Shear wave velocity (V_s) (left) and critical damping ratio (right) profiles for the original (blue) and softened (red) soil models beneath the building clusters area. Notice that there is no variation neither in V_s nor in damping.

5.4 Results and Analysis

5.4.1 Regional Response

Since we performed the same regional-scale simulation as in the first case study, we do not repeat the same information here (see Figure 3.5 for details). In the case of the DRM region, however,

Figure 5.4 shows the peak values of the amplitude of the free-surface horizontal velocity for both the original and the softened soil conditions (obtained from a Step II simulation without building models) in the building clusters region. The peak values vary between about 0.66 and 0.77 m/s, and between 0.7 and 0.84 m/s for the original and softened soil models, respectively. Since uniform soil conditions prevail in this local region, spatial variability of the free-field ground motion seen in the Figure 5.4, although not severe, has to do with the wave propagation and not with the local site conditions.

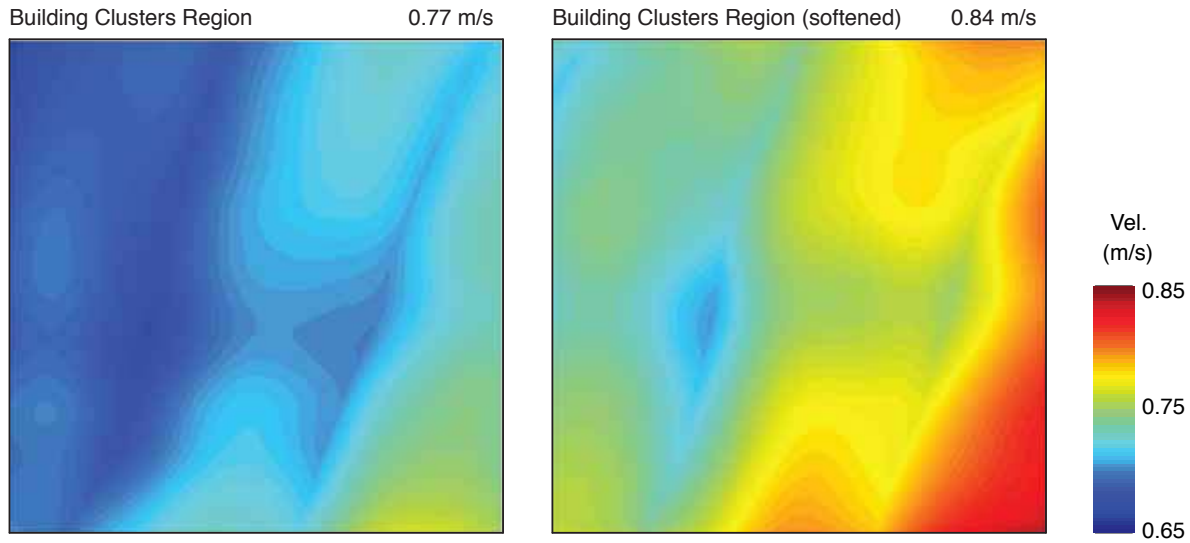


Figure 5.4: Amplitude of the peak free-surface horizontal velocity for the building clusters location within the DRM region of interest using the original velocity model (left) and the softened model (right). Maximum values are indicated at the top of each frame and to the right. The size of the square is $(0.55 \text{ km} \times 0.55 \text{ km})$.

The spatial variability of the free-field motion within the buildings' area (with no buildings present) is illustrated in Figure 5.5, for both the original and softened soil cases. The top panels show synthetic seismograms of the horizontal velocity in the NS and EW directions along 33 stations equally spaced along a diagonal of 0.77 km across the building cluster area. The variability in the amplitude and frequency content of the seismograms along the line is minimal to moderate. The middle panels show the average Fourier transform of the velocities ± 1 standard deviation in a regular grid of 33×33 stations equally spaced at 17.2 m throughout the same area. Notice that for both soil cases, near the peaks, the upper bound of the standard deviation has spectral ordinates that are 1.5 to 2 times as large as the corresponding ordinates of the lower bound. This provides a

measure of the spatial variability of the free-field ground motion, although not as severe as in the first case study, to which the buildings will be exposed. Results in Figure 5.5 help visualize the energy distribution of the ground motion with frequency. For both the original and softened soil cases, the peaks are somewhat broader in the EW than in the NS direction, and the maximum values occur between 0.5 Hz and 1.5 Hz, and between 0.5 Hz and 1.0 Hz, respectively. The energy content decays after 1 Hz and 2 Hz and is lowest between 3.5 Hz and 3.0-5 Hz, respectively. Below 1 Hz, the differences between the original and softened soil models are minimal. By contrast, above this value, relative energies alternate such that the softened soil model exhibits an increase in energy between 2.5 Hz and 3 Hz, whereas the original soil model has higher amplitudes between 3.0 Hz and 3.5 Hz, and around 4.5 Hz. Figure 5.5 also includes the average of the horizontal over vertical (H/V) spectral ratios of the free-field ground motion within the area of $0.55 \text{ km} \times 0.55 \text{ km}$ at the location of the buildings—computed for the ground response without the presence of the structures at the same 17.2 m spaced grid points. H/V ratios are often used to infer the fundamental natural frequency of sites using ambient vibration tests, but they can sometimes be difficult to interpret under strong ground shaking. Here, unlike the first case study, the peaks are much clearer, and have a similar distribution in both directions. This has to do with the uniform nature of the local site conditions. At the bottom-right frame of Figure 5.5, we highlight the presence of some resonant peaks that appear to be associated with the natural frequencies of the site. It is noteworthy that the peak value of the H/V ratio occurs at the same resonant frequencies for the EW and NS directions. The fundamental natural frequency associated with the underlying basin appears to be at 0.45 Hz. Higher resonant peaks visible at about 1.2, 1.9, 2.8, 4 and 4.5 Hz, among several other resonant, but less prominent peaks across the spectrum.

5.4.2 Effects of the Building Clusters on the Ground Motion

The combined effect of SSI and SCI on the ground motion within the region of the building clusters for the softened velocity (soil) model is illustrated in Figure 5.6. This figure shows the changes in the amplitude of the peak free-surface horizontal velocity with the buildings present, with respect

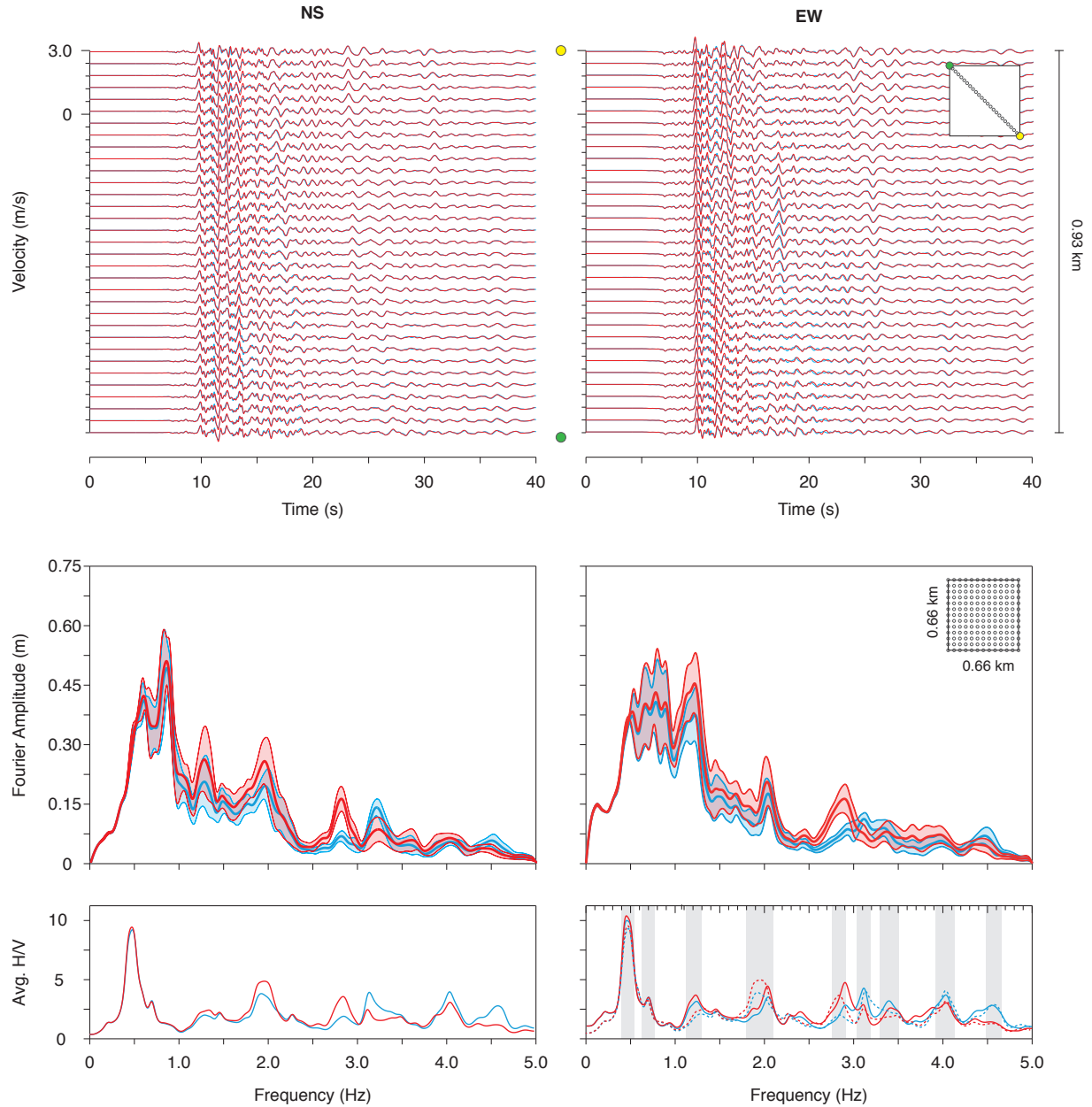


Figure 5.5: Top: velocity time series in both the NS and EW directions for a sequence of stations equidistantly distributed along a diagonal of 0.77 km from the southeast to the northwest corners of the building clusters area (see Figure 5.2). Middle: average Fourier amplitude spectra of the ground velocity within the 0.55 km \times 0.55 km buildings area, ± 1 standard deviation (shaded areas). Bottom: average H/V spectral ratio within the same area. In general, blue lines correspond to the simulation using the original soil model, and red lines to the softened soil model. The average H/V ratios for NS are repeated in the EW frame using dashed lines for cross referencing. In the same frame, the gray shaded areas indicate the presence of coincident resonant peaks in both NS and EW.

to the corresponding free-field ground motion (without buildings) for the various arrangements of the B3 model, with the clusters ranging from the isolated 1×1 (ICB) model to the 7×7 (C2) building cluster, and also for two different eccentricities (e_0, e_2) for $\Omega_1 = 1$. Similar qualitative results were observed for the B1 and B2 model configurations, for other Ω and e values, and also for the original soil conditions. This figure allows us to examine the effect that the building-foundation systems have on the ground motion in the spacing area between the buildings and in the surrounding area, as well as on the base motion of the buildings themselves. The effects are in general similar to what has been observed in the first case study (see Chapter 3). The results for the isolated case buildings (ICBs), which we consider as a baseline for comparison with the results of the various building clusters, show a reduction at the base of the buildings (about 27 percent) and increase in the ground motion around the ICBs about 4 percent for the two sets of structures with different eccentricities. Changes in the ground motion around the clusters become more relevant as the number of buildings increases, and reach 10 percent. There are also noticeable changes in the ground motion between the buildings, which tend to be mostly reductions of about 10-15 percent in this case. However, small amplifications are also visible for the S2 separation cases.

Looking now at the motion of the buildings at ground level, reductions on the order of 15 to 25 percent on average are predominant with respect to the corresponding free-field motion. From the results in Figure 5.6 it appears that the building foundations begin to act as a unit vis-à-vis the seismic motion as the concentration of buildings increases. This results in an effective surface dimension that gets closer to the wavelengths of the incoming waves; this causes an increase in the amount of scattering. For instance, the building clusters B3-C2-S1 for both of the eccentricities has total base dimensions of $435 \text{ m} \times 330 \text{ m}$. The side dimensions are comparable to a wavelength of 444 m that corresponds to a velocity V_{S30} of 400 m/s (see Figure 5.3), and a frequency of 0.9 Hz, for which the peak free-field motion in the NS direction occurs (see Figure 5.5).

Also shown at the bottom of the Figure 5.6, are the difference plots that compare the asymmetric and the corresponding symmetric building clusters in order to isolate torsional coupling effects. That is, they show the changes in the amplitude of the peak surface horizontal velocity of

the clusters of the asymmetric B3 building with e_2 eccentricity, with respect to the clusters of the corresponding symmetric structure (e_0), for the same cluster arrangements considered above. In other words, frames in the row C (bottom row) are obtained by calculating the relative difference between the values that appear in the corresponding frames in rows B and A. By looking at row C, it can be inferred that the differences in the ground motion between the symmetric and the asymmetric structures are minimal. It is noteworthy that, looking at the base motion of the ICB, the amplitudes are higher for the symmetric ICB around the stiff side (of the asymmetric building-see Figure 5.1), and conversely they are higher for the asymmetric ICB around the flexible side. The same pattern can be seen in the C2-S2 case, also in the C2-S1 case to some extent. However, their effects on the total change in the amplitude with respect to the corresponding free-field ground motion is negligible.

5.4.3 Structural Behavior of Buildings

SCI Effects on Structural Response

The response of a single asymmetric building supported on a flexible soil, depends on the input motion, the dynamic properties of the structure (including the eccentricity (e) and the uncoupled frequency ratio (Ω)), and the impedance ratio between the structure, its foundation, and the surrounding soil. In a collection of buildings, however, additional factors, such as the number of buildings and separation between them, influence the response of the individual buildings and of the ensemble. In this section we summarize the overall structural response of the different types of buildings and clusters described in Tables 5.1 to 5.5 in terms of the peak roof response. We recall that all the structures within each cluster are identical, and that we consider three different general structure types with the following fixed-base fundamental translational frequencies: 2.50 Hz (B1), 0.85 Hz (B2), and 0.25 Hz (B3), corresponding approximately to 3-, 13-, and 40-story buildings. We model six buildings with different e and Ω values for each of these general structure types (see Table 5.3). We consider two different building clusters (C1, C2) according to the number of

buildings in each cluster (3×3 , 7×7), and different separations ($S1$, $S2$) as listed in Table 5.5.

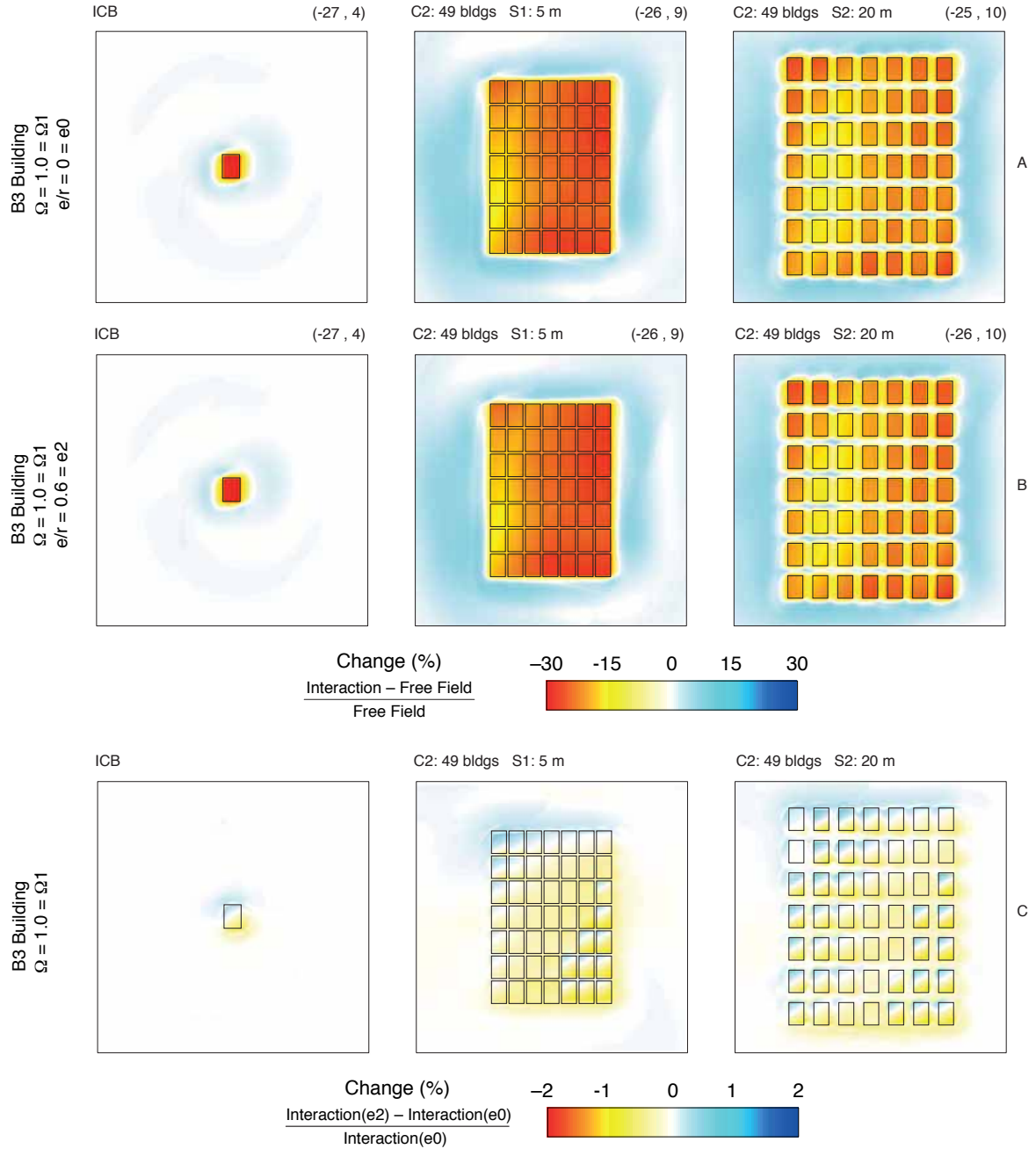


Figure 5.6: (top rows A-B) Change in the peak horizontal-magnitude velocity at the free-field level for the 40-story building (B3) clusters with variable number of buildings (C1, C2) and spacing ($S1$, $S2$) and also for two different eccentricities (e_0 , e_2) for $\Omega = 1$. Only, results for the softened velocity (soil) models are shown. Minimum and maximum values are indicated at the top-left corner of each frame. (bottom row C) The same type of figure but this one shows the change in the peak horizontal-magnitude velocity between the asymmetric (e_2) and the symmetric (e_0) (otherwise identical) clusters. Note that $C = (B - A)/A$.

Figures 5.7 and 5.8 show the variability of the relative roof displacement normalized by the

corresponding building height, F_F/h in Figure 3.11 of Chapter 3, for each cluster configuration, for only the softened soil conditions, and only in the EW direction (where the eccentricity is perpendicular). We refer to this normalized displacement as the relative roof displacement. Figure 5.7 shows the relative roof displacements of the structures with $\Omega = 1$ and Figure 5.8 shows them for the structures with $\Omega = 1.3$. In both figures, buildings with three different eccentricities ($e0$, $e1$, and $e2$) are compared for each of the structure type and the relative displacement values are given at three different points in the structure (at a point on the stiff side, at the center point, and at a point on the flexible side - see Figure 5.1). Also included, for reference, are the values of the corresponding isolated (ICB) and the fixed-base structure (FCB) and those of the buildings at the center of any given cluster (CB). FCB response was obtained separately using as input at the base of the building the free-field horizontal ground motion recorded at the same location of CB during the simulation with the buildings absent. Solid circles denote the minimum and maximum deformation of all the structures within a given cluster; the mean value is indicated with a small horizontal bar. The normalized relative roof displacements of the corresponding CB and FCB are indicated with an open circle and with an asterisk, respectively. Considering the response of a complete cluster of structures located within the same general area allows us to simultaneously analyze the effects of the spatial variability of the ground motion on the structural response, the interaction of each structure with the soil, and the coupling through the soil between the multiple structures. This also enables us to compare the effect of the eccentricity on the normalized relative roof displacement.

Several observations can be made from Figure 5.7.

- (i) For all the buildings with different eccentricity values for a given structure type (B1, B2, and B3), the relative roof displacements for the fixed-base structures (FCB) are bigger than the corresponding CB values. This implies that base flexibility reduces the response in all cases. However, our results in Chapter 3 for the symmetric buildings show that SSI effects are not necessarily conservative. We believe that this difference is due to the base rocking, which is neglected in this study but was included in the first study.

(ii) As mentioned earlier, $e = 0$ corresponds to the symmetric structure. Thus, for this structure, the difference between the responses of the flexible and the stiff sides should be solely due to the rotational components of the ground motion. However, these differences are negligible here as seen in the figure.

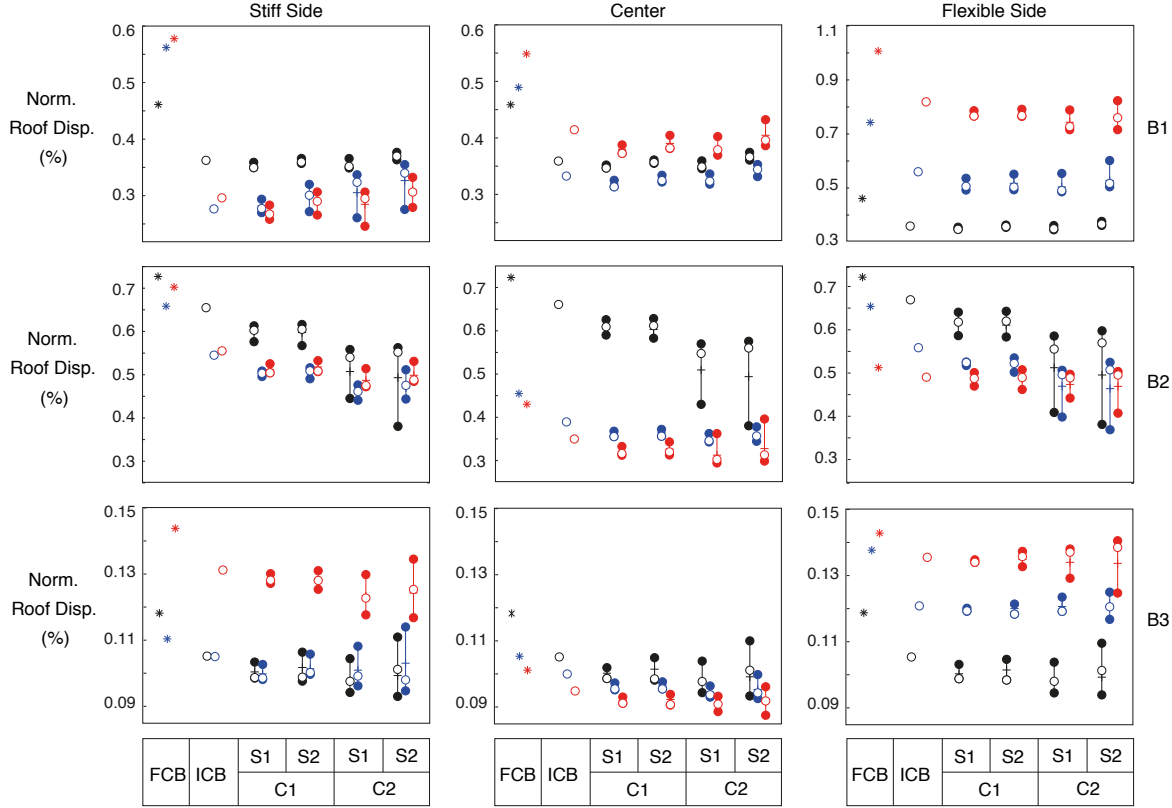


Figure 5.7: Variation in the normalized relative roof displacement for structures with $\Omega = 1$, at three different points (stiff side (left), center (middle), flexible side (right)), for different configurations and for different eccentricity values in the EW direction (where the eccentricity is perpendicular). The three different normalized eccentricity (\bar{e}) values are; 0 (black), 0.3 (blue) and 0.6 (red). Only results for the soft soil model are given. Filled symbols show the ranges (minimum to maximum); the average is indicated with a small horizontal bar. Open symbols indicate the normalized relative roof displacement of the center building (CB). Asterisk symbols indicate the normalized relative roof displacement of the fixed-base building (FCB).

(iii) On the other hand, for the asymmetric buildings ($e1$ and $e2$), maximum, minimum, and the mean values in the clusters and also the response of the CBs tend to be bigger both on the flexible and stiff sides than those at the center. There is, however, one exception. For the B1-type structures, both of the asymmetric buildings have bigger values at the center than on the stiff side. Also notice that the relative displacements on the flexible side of the B1-type

asymmetric structures (B1- e_1 , B1- e_2) are 1.5 to 2 times higher than those at the center.

- (iv) For the stiff side of the B1-type and the center of the B3-type buildings, and also for all the B2 buildings, the relative displacements in the clusters tend to be bigger in the symmetric building than the asymmetric ones. For all the other structures, buildings with the e_2 eccentricity have the biggest values.
- (v) The other important effect is the difference, although not as pronounced as the first case study, that can occur between the minimum and maximum relative roof displacement for the various structures in a given cluster. This is due in large part to the spatial variability of the ground motion.
- (vi) For a given cluster, the spread in the normalized relative roof displacement increases with the separation between the structures.

The above-mentioned observations are also applicable to Figure 5.8. There are, however, other observations that can be made from this figure.

- (i) For the asymmetric buildings, maximum, minimum, and the mean values in the clusters and also the response of the CBs on the flexible side are systematically larger than those at the center, whereas the values on the stiff side are the smallest among three. This behaviour has also been observed by others (e.g. Hejal, 1987).
- (ii) For the B1-type structures, on the flexible side and at the center, the relative roof displacements increase with the eccentricity ($e_2 > e_1 > e_0$). However, this relationship reverses for those of the values on the stiff side ($e_0 > e_1 > e_2$). The same pattern mostly holds true for the B2-type and the B3-type structures with one exception. That is, at the center of the B2-type structures, buildings with the e_2 eccentricity have the smallest values.

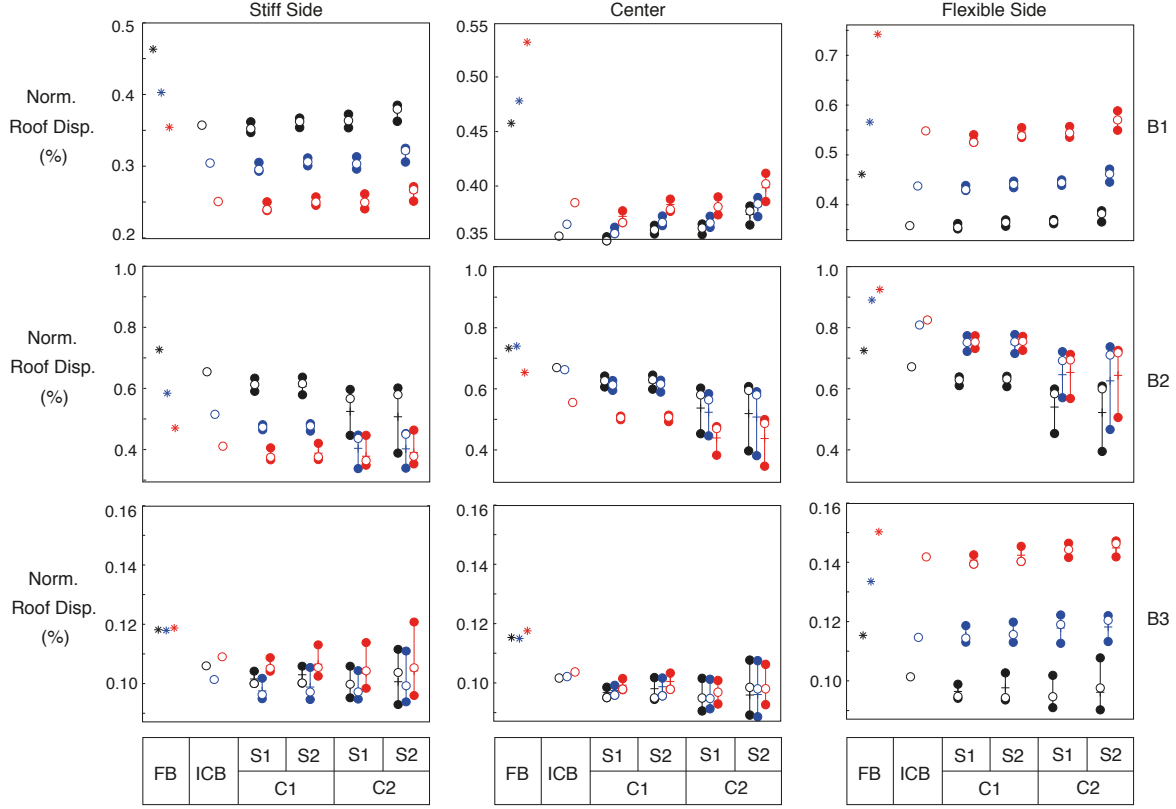


Figure 5.8: Variation in the normalized relative roof displacement for structures with $\Omega = 1.3$, at three different points (stiff side (left), center (middle), flexible side (right)), for different configurations and for different eccentricity values in the EW direction (where the eccentricity is perpendicular). The three different normalized eccentricity (\bar{e}) values are; 0 (black), 0.2 (blue) and 0.4 (red). Only results for the soft soil model are given. Filled symbols show the ranges (minimum to maximum); the average is indicated with a small horizontal bar. Open symbols indicate the normalized relative roof displacement of the center building (CB). Asterisk symbols indicate the normalized relative roof displacement of the fixed-base building (FCB).

To examine the influence of SCI effects, we now compare the results of the CB with those of the corresponding ICB model. Since these two models, namely CB and ICB, are identical, and are placed at the same location, any change in the response between the two structures is due entirely to SCI effects. Figure 5.9 shows the changes in the peak relative roof displacement of the center building due to the changes only due to site-city interaction. They only include the interaction effects due to the presence of the surrounding buildings. Therefore, the change due to SCI effects alone in Figure 5.9 is zero for the ICB cases as there are no additional surrounding structures. In all other cases, however, we observe changes with respect to the ICB, as follows:

- (i) Our results in Chapter 3 show that pure SCI effects always decrease the level of deformation in the structure. That is, all the values in Figure 3.13b are negative. However, for this case study, both positive and negative values are present, which implies that SCI effects are not always conservative. For instance, for the B1-type buildings with $\Omega = 1$ and $e2$, pure SCI effects increase the relative roof displacement by more than 20 percent on the stiff side.
- (ii) Net SCI effects do not show a clear link with the eccentricity value. For some cases ($\Omega2$ -B2-flexible side) net SCI effects systematically increase with the eccentricity value, but for other cases ($\Omega1$ -B2-center) the biggest net SCI effects are observed for the symmetric structures.
- (iii) The range of the values and the patterns are generally similar for all the three different points considered for a given structure type and a Ω value.

Transfer Functions in the Presence of Site-City Interaction

All the numerical results of the present study have been based on the simulation of a single earthquake. As we have seen, the results can help provide insight into the behavior of the individual structures within a cluster and of the extent of coupling between them. However, so far, they do not explicitly provide any information regarding the possible response that might occur under a different earthquake. While from this single simulation it is not possible to extrapolate the results to an arbitrary earthquake, we can nonetheless extract several transfer functions of interest in order to examine the dynamics of the cluster's response for an earthquake source of similar general characteristics (fault, epicenter, asperities, and rupture velocity), but independent of the particular frequency distribution of the free-field ground motion at a given site. In this section we examine two types of transfer functions. These transfer functions are obtained by dividing the amplitude of the Fourier transform of a given quantity as a function of frequency by the corresponding amplitude of the Fourier transform of the free-field ground motion at the same location. This is done for the total lateral motion at the base of each structure at three different points (flexible side, center, stiff side), and for the relative roof response at the same three points.

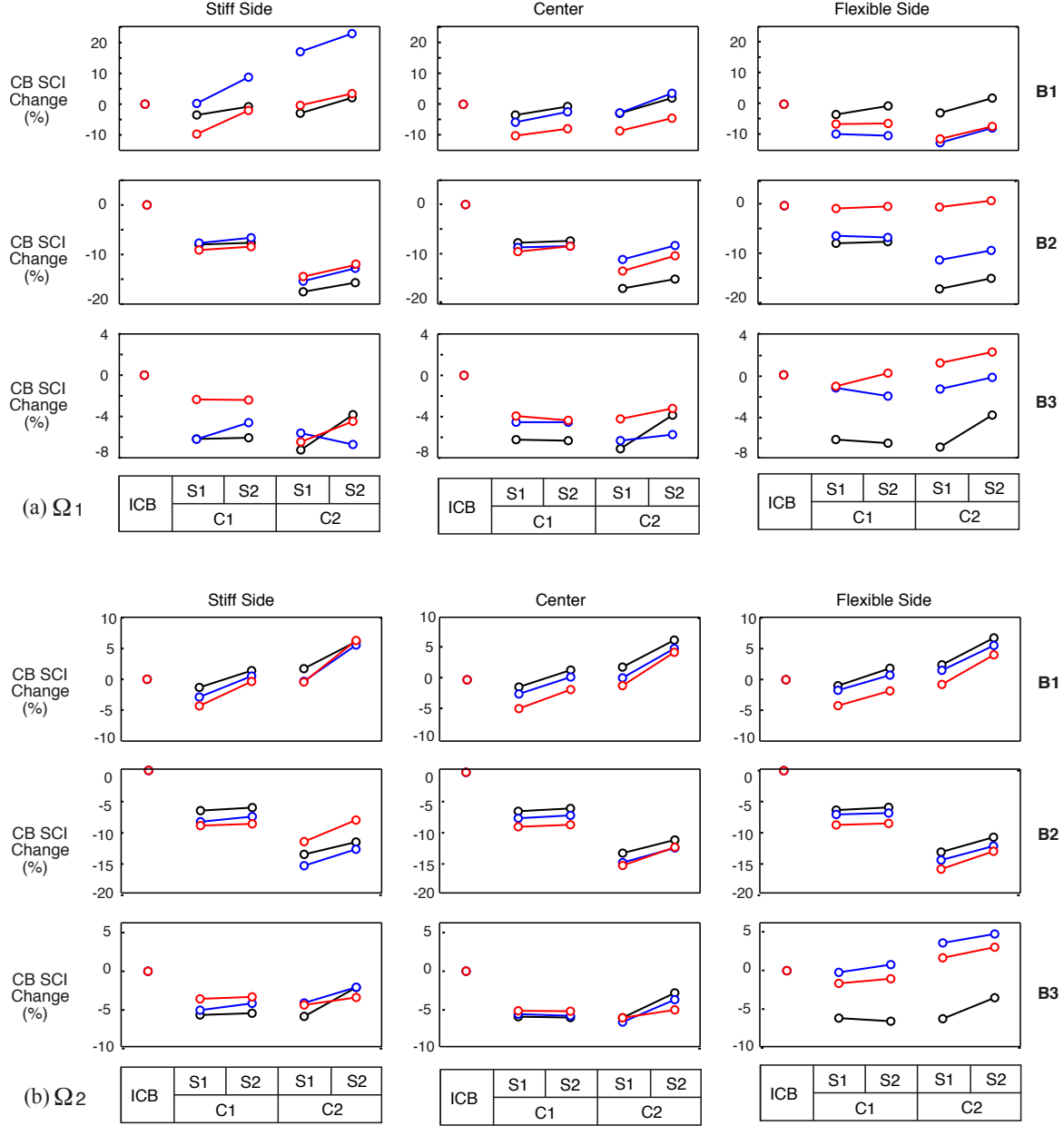


Figure 5.9: Change in the normalized relative roof displacement of the center building (CB) due to interaction effects for the different configurations in the EW direction and the softened soil conditions. (a) Changes in the normalized displacement of the CB due solely to site-city (SCI) interaction effects, relative to the ICB for the structures with $\Omega = 1$. The three different normalized eccentricity (\bar{e}) values are; 0 (black), 0.3 (blue) and 0.6 (red) (b) Changes in the normalized displacement of the CB due solely to site-city (SCI) interaction effects, relative to the ICB for the structures with $\Omega = 1.3$. The three different normalized eccentricity (\bar{e}) values are; 0 (black), 0.2 (blue) and 0.4 (red).

Figure 5.10 shows the transfer functions between the relative roof and the free-field motions of the fixed-base structures for all the building models and eccentricities considered in this study.

Results are shown for the points on the flexible and on the stiff sides, and also for the center point. Torsional coupling effects are most noticeable for the B1-type structures. Notice that the symmetric structure ($e0$) has identical transfer functions at all the three points. For B1 buildings with $\Omega = 1$, the uncoupled translational frequency is the same as the torsional one, and is equal to 2.5 Hz. With the eccentricity, at the center point, the peak at 2.5 Hz is split in two smaller peaks, and these peaks depart from each other as the eccentricity value increases. However, at the point on the stiff side, transfer function is shifted to the right and a large peak appears at the same frequency of the second peak of the center point. On the flexible side the opposite is true; the transfer function is shifted to the left with the eccentricity and a large peak appears at the same frequency of the first peak of the center point. Also notice that on the flexible side, there is another peak that appears at around 4.5 Hz, which is probably due to the coupling of the second fundamental frequency of the structure. For B1 buildings with $\Omega = 1.3$, on the other hand, torsional coupling effects are minimal at the center point. The peak at 2.5 Hz is reduced in the amplitude and shifted to the left with the eccentricity. On the stiff and the flexible sides, however, coupling effects are more pronounced. On the stiff side, the peak at 2.5 Hz is significantly reduced in amplitude and shifted to the left for the asymmetric structures. There, in addition, appears a second peak at the right of the uncoupled torsional frequency (3.25 Hz). The amplitude of this second peak is even larger than the first one for the asymmetric structure with the $e2$ eccentricity. On the flexible side, with the eccentricity, the peak at 2.5 Hz increases in amplitude, but the second peak that is close to the uncoupled torsional frequency is not as pronounced as that on the stiff side. This increase in the amplitude of the first peak is probably the reason why the relative roof displacements are the highest on the flexible side in Figure 5.8. Similar effects of torsional coupling can be observed for the other structure types (B2 and B3). Note that higher translation and torsional modes are also present (and coupled) for these buildings.

Figures 5.11 and 5.12 show the average base and roof transfer functions for all the B1 building models considered in this study for the various eccentricity and Ω values. These figures include the results of the softened soil model, and show the ranges between the minimum and maximum

envelopes of all the transfer functions. For reference, these figures also show the first few natural frequencies of vibration of the corresponding rigid-base building model. Recall that for all the systems considered in each set, the foundation-building model is the same. Therefore, the variability observed in the transfer functions in Figures 5.11 and 5.12 involves the changes in the ground motion depending on the location of any given building in the cluster, and the combined action of the individual SSI and the collective SCI effects.

Figure 5.11 shows the variability of the transfer functions of the base motion for the B1-type structures for different e and Ω values. In each case, the shape of the average transfer functions exhibits the blips and reductions around the natural frequencies as discussed before in Chapter 3. Both the inertial and kinematic interactions play a role in influencing the base motion and filtering out higher frequencies. On average, the base response experiences a rapid reduction above each natural frequency. Notice also that, in all cases, the variability increases with the frequency. For brevity, results for the B2-type and B3-type buildings are included in Appendix D.

Figure 5.12 focuses on the variability of the transfer functions for the relative roof response of the B1-type structures with different eccentricities and Ω s. These results are compared to the transfer functions of the corresponding rigid-base structure. As expected, the natural frequencies of the flexible-soil systems are smaller than those of the rigid-base reference models, and the effective damping increases (as reflected by the smaller resonance amplitudes). These are well-known SSI effects (e.g. Jennings and Bielak, 1973; Veletsos and Meek, 1974). However, the frequency shifts in this case are somewhat smaller than the ones that are observed in Chapter 3. We believe that this is mainly due to the fact that base rocking is restrained in this study. Similar results for the B2-type and B3-type building are included in Appendix D. Another aspect of interest captured by the transfer functions shown in Figures 5.11 and 5.12 is the increased response and variability with frequency. This behavior is already investigated in detail in Chapter 3.

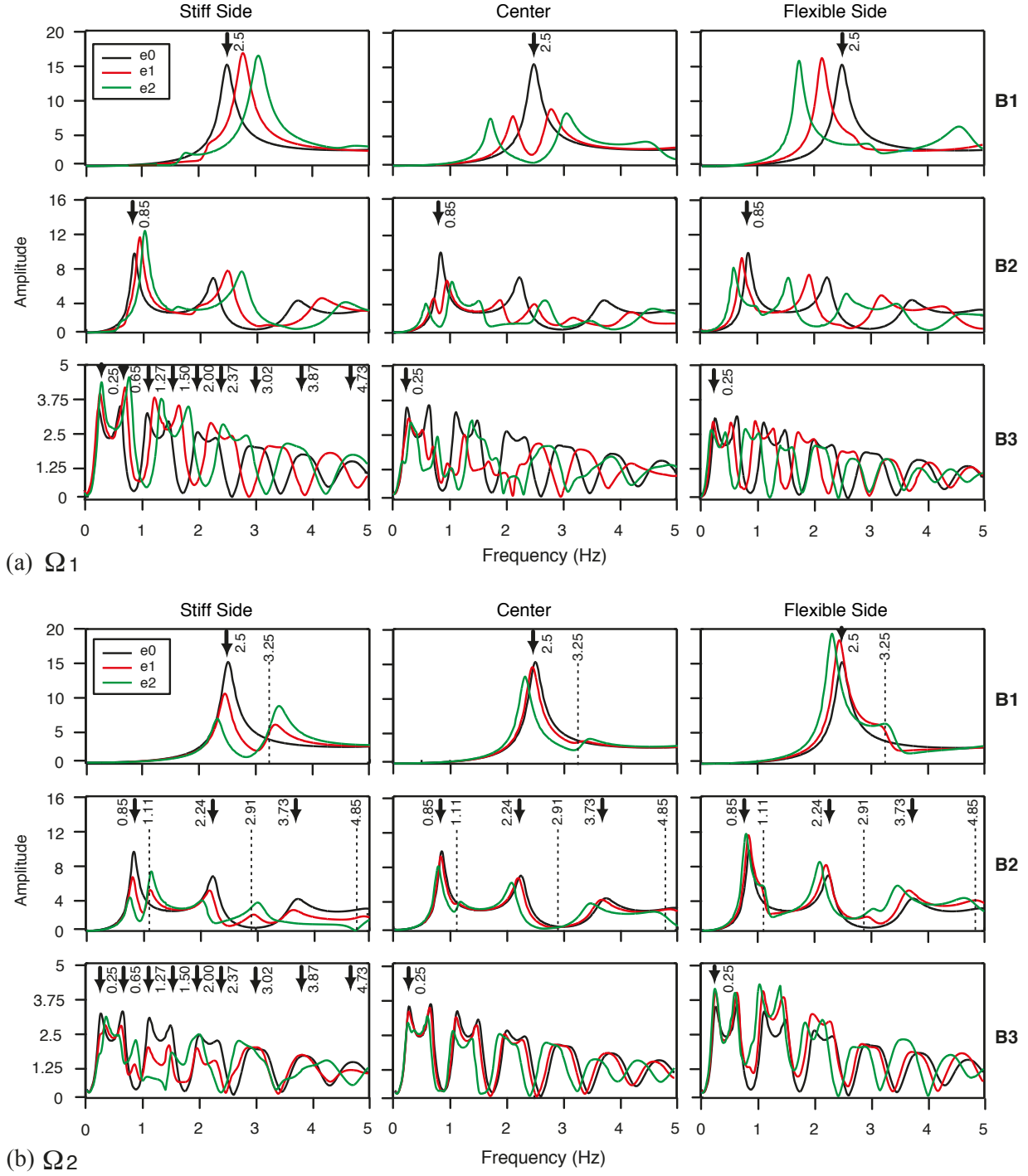
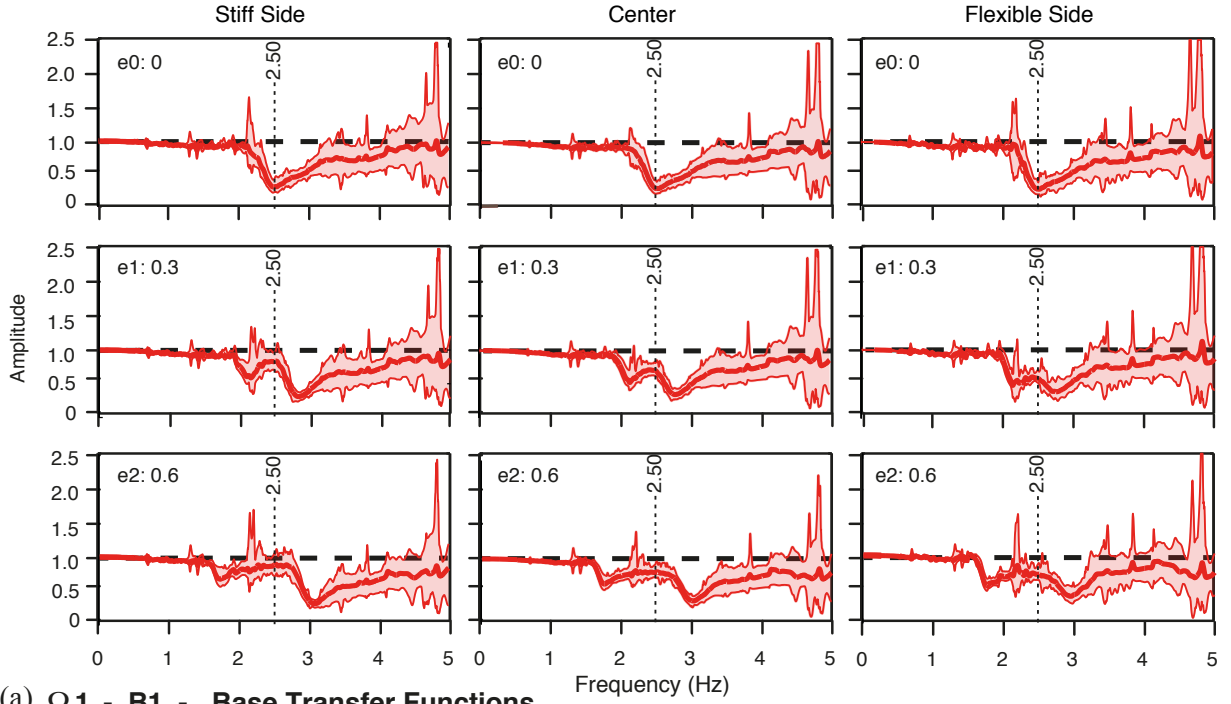
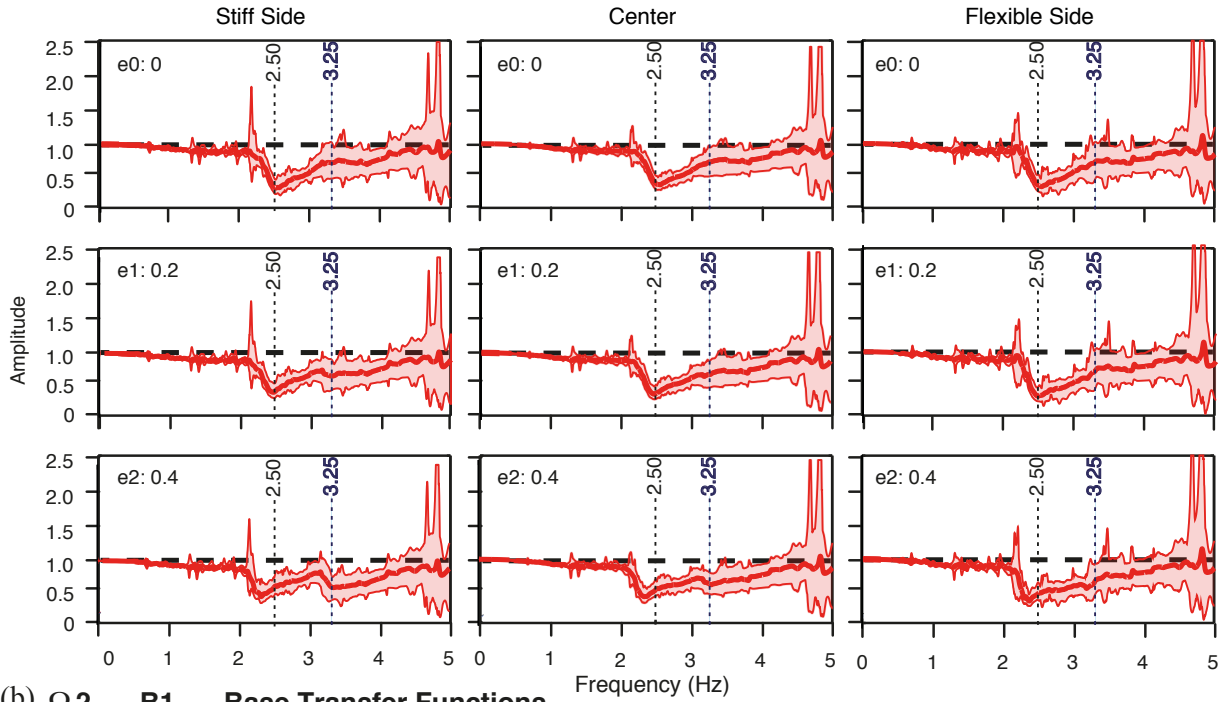


Figure 5.10: Transfer functions of the fixed-base structures between the relative roof and the free-field motions for all the building models and eccentricities. The black arrows in each frame indicate the uncoupled translational frequencies of the rigid-base models. (a) For $\Omega = 1$. (b) For $\Omega = 1.3$. In each frame, the vertical dotted lines mark the uncoupled torsional frequencies of vibration of the rigid-base model for each type of building.

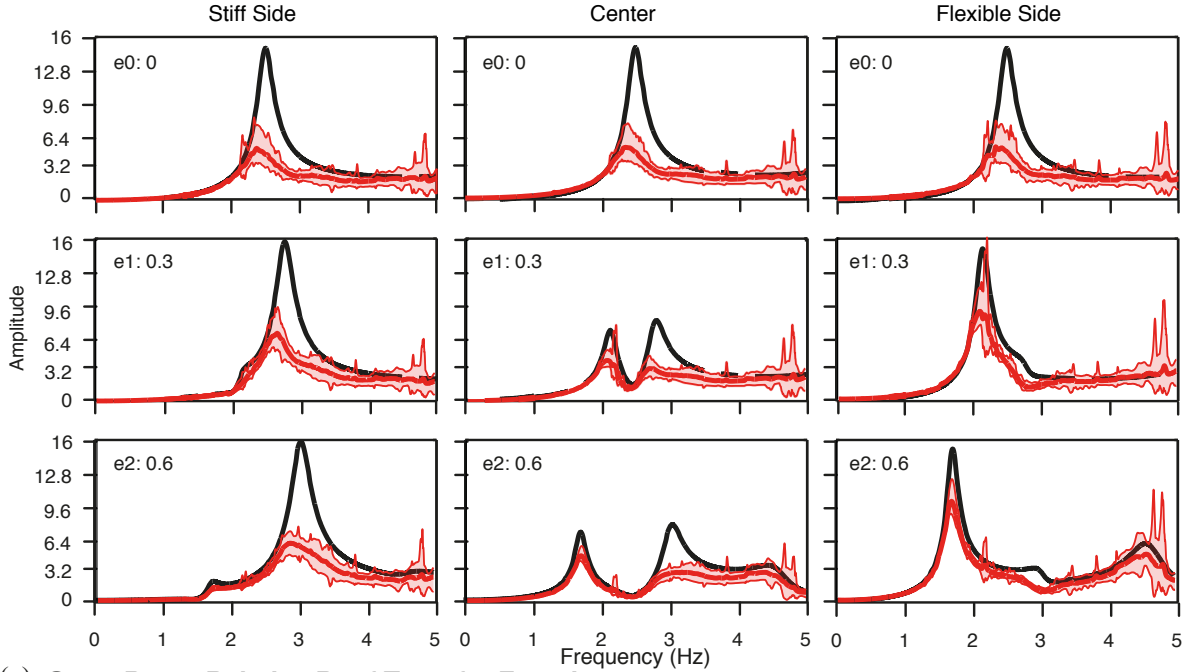


(a) Ω_1 - B1 - Base Transfer Functions

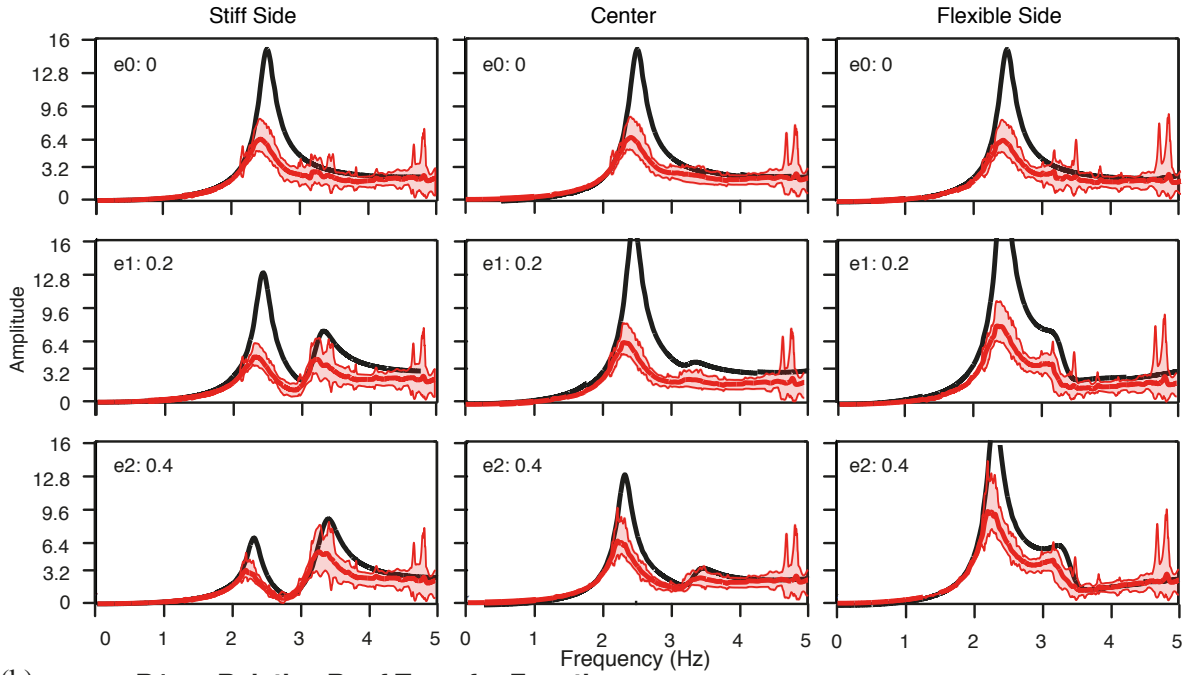


(b) Ω_2 - B1 - Base Transfer Functions

Figure 5.11: Average (thick lines) and maximum and minimum envelopes (thin lines) of the transfer functions between the base and the free-field motions for all the B1-type buildings with different e_s and Ω_s in the various cluster and spacing arrangements in the EW direction. Only results for the softened soil conditions are presented. Filled areas cover the range from the minimum to the maximum envelopes. The black dashed line indicates the case of no interaction. In each frame, the vertical dotted lines mark the uncoupled translational and torsional (bold lines) frequencies of vibration.



(a) $\Omega 1$ - B1 - Relative Roof Transfer Functions



(b) $\Omega 2$ - B1 - Relative Roof Transfer Functions

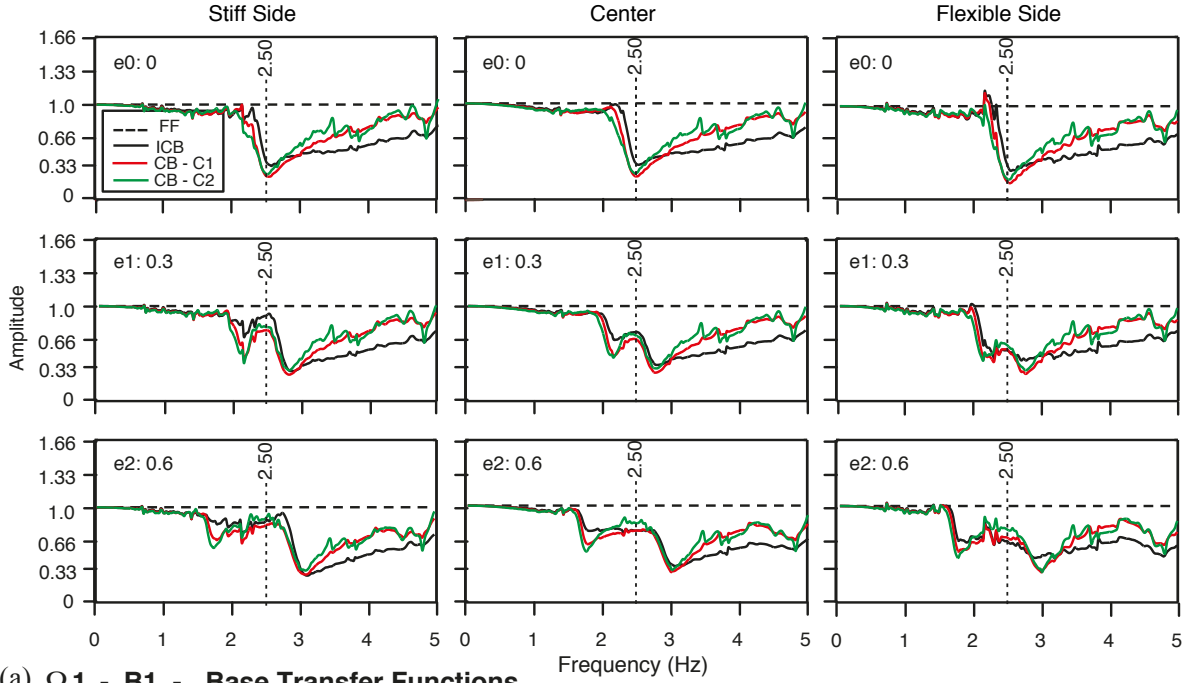
Figure 5.12: Same as Figure 5.11 but for the transfer functions between the relative roof and the free-field motions. Here, the black lines correspond to the transfer functions of the rigid-base models.

SCI Effects on the Transfer Functions of the Control Building

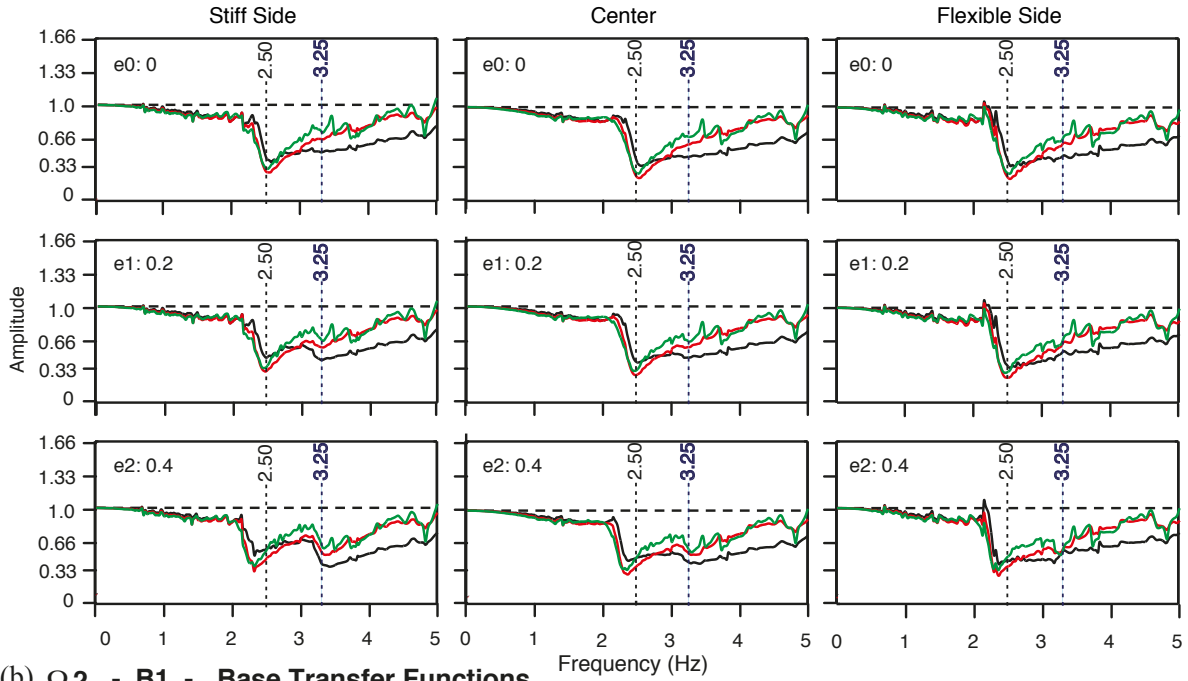
We focus now on the changes due to the collective SCI effects, as opposed to those caused by SSI alone, using the response of the center building (CB) of each cluster. We compare its behavior with that of the corresponding ICB case; that is, the same building but without any other buildings around it. Figures 5.13 and 5.14 show, respectively, the base and relative roof transfer functions with respect to the free-field motion at the same location of the CB for the B1-S1 structures with different e s, Ω s, and cluster arrangements, including the corresponding transfer functions of the ICB. These results correspond to the simulations done using the softened soil model.

Detailed analysis of the cluster effects on the symmetric structures have been presented in Chapter 3. In this section, torsional coupling effects are investigated as well. The observations made from Figure 5.13 are as follows:

- (i) For the buildings with $\Omega 2$, looking at the responses of the ICBs on the stiff side, it is noticeable that the transfer functions tend to have a second rapid reduction near the corresponding uncoupled torsional frequency. This is especially evident for the case of $\Omega 2 - e 2$. In addition, for the asymmetric ICBs with $\Omega 1$, frequencies where the reductions occur shift to the right with the increasing eccentricity values.
- (ii) Looking now at the center points of the ICBs with $\Omega 1$, rapid reductions occur at two different frequencies, and these frequencies move apart with the increasing eccentricity values. For the ICBs with $\Omega 2$, on the other hand, the changes between the buildings with different eccentricities are less significant.
- (iii) For the ICB responses on the flexible side, the patterns are similar to those seen at the center point, for both Ω values.
- (iv) Irrespective of the values of Ω and e , the SCI effects on the CBs decrease the amplitudes of the blips and the rapid reductions. At frequencies larger than 3 Hz, however, the transfer functions of the CBs have higher amplitudes than those of the corresponding ICBs.

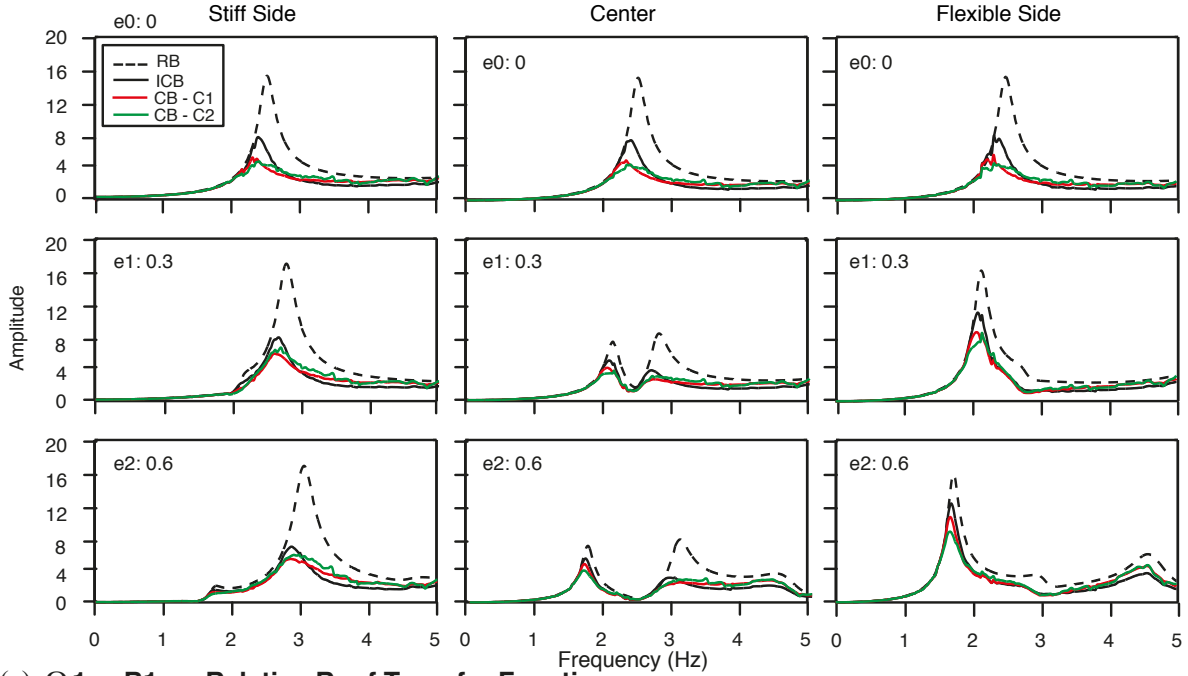


(a) $\Omega 1$ - B1 - Base Transfer Functions

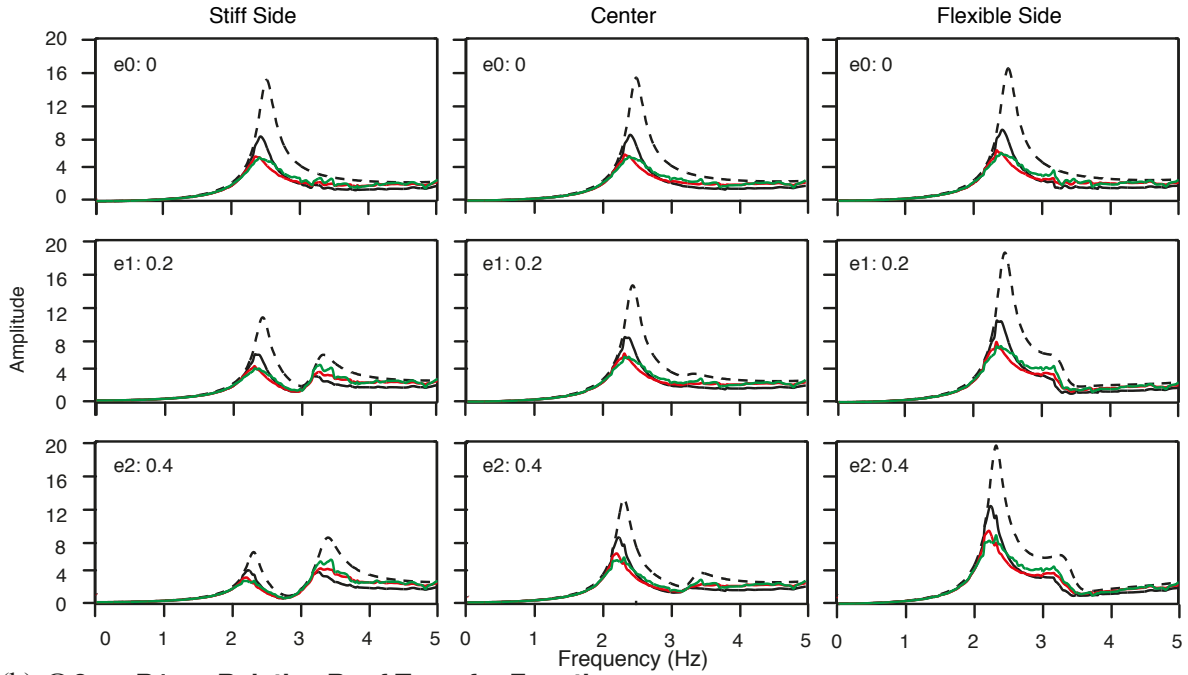


(b) $\Omega 2$ - B1 - Base Transfer Functions

Figure 5.13: Comparisons between the base transfer function of the isolated control building (ICB) (black) and the various transfer functions corresponding to the same building at the center of each cluster (CB) for the arrangements C1 (red) and C2 (green) for the B1-S1 structures with different e and Ω values. The horizontal dashed line indicates no change with respect to the free-field motion. These results correspond to the motion in the EW direction and to the softened soil system and are given at three points in the structure located; on the stiff side (left), at the center (middle), on the flexible side (right). In each frame, the vertical dotted lines mark the uncoupled translational and torsional (bold lines) frequencies of vibration.



(a) $\Omega 1$ - B1 - Relative Roof Transfer Functions



(b) $\Omega 2$ - B1 - Relative Roof Transfer Functions

Figure 5.14: Comparisons between the system's relative roof transfer function (with respect to the free-field) of the isolated control building (ICB) (black) and the various transfer functions corresponding to the same building at the center of each cluster (CB) for the arrangements, C1 (red) and C2 (green) or the B1-S1 structures with different e and Ω values. The dashed line corresponds to the relative roof transfer function of the rigid-base (RB) system. These results correspond to the motion in the EW direction and to the softened soil system and are given at three points in the structure located; on the stiff side (left), at the center (middle), on the flexible side (right).

- (v) Other cluster effects that are observed in Chapter 3 are applicable here as well. Yet, the blips are not as pronounced as they are in Figure 3.16, probably due to the restraint on base rocking. Similar results for the B2-type and B3-type building are included in Appendix D.

The coupled interaction effects of the various building models and arrangements also have an impact on the structural response of the building models. Figure 5.14 shows the relative roof transfer functions of the CB in each cluster with respect to that of the corresponding ICB and the rigid-base model for the B1-S1 buildings with different Ω and e values. The trends that are observed in Chapter 3 for the symmetric structures mostly hold true in this study as well. There are, however, additional observations worth mentioning:

- (i) Natural frequency shifts due to the flexibility of the soil are not as pronounced as those seen in Figure 3.17. Moreover, the spikes that appear at the higher frequencies in Figure 3.17 are not significant in this figure (see also Appendix D for the transfer functions of the B2-type and B3-type buildings). Based on these observations, we believe that base rocking plays a significant role in the first case study, by widening the frequency shifts, and also by enhancing the presence of the spikes at higher frequencies.
- (ii) Torsional coupling effects can be examined by comparing the transfer functions of the symmetric and different asymmetric structures for a given Ω value at a particular point. The trends seen in the transfer functions of the ICBs are very similar to those of the rigid-base buildings. Therefore, the observations in section 5.4.3 for Figure 5.10 are applicable here as well.
- (iii) The peak amplitudes in the transfer functions of the CBs decrease with the cluster effects as compared to those of the ICBs. At frequencies higher than 3 Hz, however, the transfer functions of the CBs have higher amplitudes than the corresponding ICBs. This is especially pronounced for the structures with $e2$. These amplifications at high frequencies, in turn, help to increase the relative roof responses of the CBs with $e2$ as compared to the corresponding ICBs, as seen in Figure 5.9.

CHAPTER 6

Conclusion

We presented results from a series of numerical simulations designed to analyze the soil-structure interaction and coupling effects of various arrangements of regular building clusters during earthquakes. In the first case study, where we consider only symmetric structures, our results suggest that the ground motion in and around building clusters, and the base motion of the structures themselves change due to the combined action of local site conditions and individual SSI and collective SCI effects. The changes in the peak ground velocities between and around the buildings oscillate between reductions of the order of 30 percent and amplifications of about 10 percent with respect to the free-field ground motion (without buildings); and the peak horizontal velocities of the buildings' base motion can decrease by as much as 40 percent with respect to that of the free field for soft soils. In addition, we have shown that there is a large reduction in the spectral base motion at frequencies above the fundamental and higher natural frequencies of vibration, even for a single structure; and that its behavior is susceptible to the presence of additional structures—as inferred from our comparisons of the behavior of the building at the center of a cluster with respect to the corresponding response for the building in isolation. These changes, due to the kinematic and inertial interaction effects of the soil-structure systems, are also reflected in the structural response of the buildings. It is well known that soil-structure interaction effects introduce changes in the frequencies and amplitudes of the structural response near the systems fundamental natural frequencies of vibration. What is not equally recognized is that these changes can be significantly

stronger at the higher frequencies, and that the presence of neighboring structures can also have significant effects on the response of individual buildings. Our results indicate that the amplitude associated with the resonant frequencies can be modified by as much as 40 percent for the systems considered. SSI effects are usually expected to result in a reduction of the response with respect to that of the corresponding structure on a rigid base. In the first case study we found this to be generally the case. However, in a number of situations the peak response increased due to the combined effects of SSI and SCI. Using the response of an isolated building with and without interaction effects as reference, we were able to identify that, in some situations, SCI may be of as much as 75 percent of the total combined effects of SSI and SCI. This contribution is likely to be lesser in the case of irregular buildings with random distributions. Ultimately, whether the combined effects of SSI and SCI are significant or not in terms of the overall response of individual structures will depend, to an important extent, on the specific conditions of resonance and impedance between the soil and the structure-foundation systems. This will determine whether the effects of SCI add or subtract to the effects of SSI. This can have implications in the design of structures, especially if one considers that SSI is generally regarded as having a beneficial effect, and seismic design provisions for SSI reflect this understanding. We recognize that our results are based on a simulation of a single earthquake, the 1994 Northridge earthquake, and highly idealized linear structural models. They represent only an initial step toward the 3D analysis of site-city interaction under realistic geological and source conditions. Nonetheless, the behavior of the structural models, judged by the characteristics of the individual response of the isolated models, matches well the typical linear behavior of analytical and experimental studies of soil-structure systems, and illustrates the potential effects of SCI. Overall, we found that SCI effects increase as the number of structures increases and the separation between the buildings decreases. The presence of additional buildings also contributes to the occurrence of coupling and interference between buildings, especially when the buildings' natural frequencies are close to the natural frequency of the site, and even more when both are enhanced by the dominant frequency of the ground motion. For the case of the San Fernando Valley region and models considered in this study, both SSI and SCI were found to be

moderate—except for the soft area at the northeast corner of the region of interest for the symmetric structures. This is understandable considering that the shear wave velocity in the underlying soil structure within the region of consideration assumes values below 300 m/s only within the top 5 m. These effects may also be of considerable importance in other regions of the world with soft soil deposits, like Mexico City.

As a second case study, we investigated torsional coupling of the asymmetric structures under the action of SSI and SCI effects. For this, we have modified our structure models so that they act as 3D shear buildings. Our results suggest that peak responses of the asymmetric structures in the clusters differ considerably than those of the symmetric buildings. These differences are also revealed by comparing the transfer functions. Torsional coupling effects on the changes in the peak ground velocities between and around the buildings, however, seem negligible. Base rocking is restrained for this study. As a future work, by using shear buildings that allow base rocking, it will be possible to isolate the relative influence of base rocking and base lateral translation on SSI.

We believe that our results underline the importance of studying site-city interaction effects, and highlight their relevance in highly dense urban areas and regions characterized by the presence of soft-soil deposits, where these effects may be highly significant. Future studies should endeavor to assess the extent and practical importance of these effects based on available data from instrumented buildings or full-scale experiments. It would also be beneficial to give additional attention to the influence that individual and collective interaction effects can have on the contribution from the higher modes of vibration on the structural response. In the future, studies based on simplified models, like the present one, can be used to define the resulting base motion of building clusters, and then such modified base motion can be used to examine in detail the response of more realistic individual building models, including nonlinearities. This would require some level of model calibration, but could provide a path to incorporating SSI and SCI effects in practice.

Bibliography

- Ayre, R. S. (1938). Interconnection of translational and torsional vibrations in buildings. *Bulletin of the Seismological Society of America*, 28(2):89–130. [1.1.3](#)
- Ayre, R. S. (1943). Experimental response of an asymmetric, one-story building model to an idealized, transient ground motion. *Bulletin of the Seismological Society of America*, 33(2):91–119. [1.1.3](#)
- Balendra, T., Tat, C. W., and Lee, S.-L. (1982). Modal damping for torsionally coupled buildings on elastic foundation. *Earthquake Engineering & Structural Dynamics*, 10(5):735–756. [1.1.3](#)
- Bao, H., Bielak, J., Ghattas, O., Kallivokas, L. F., O’Hallaron, D. R., Shewchuk, J. R., and Xu, J. (1998). Large-scale simulation of elastic wave propagation in heterogeneous media on parallel computers. *Computer Methods in Applied Mechanics and Engineering*, 152:85 – 102. [2.2](#)
- Bard, P.-Y. (1988). The importance of rocking in building motion: An experimental evidence. *Proceedings of Ninth World Conference on Earthquake Engineering August 2-9. 1988. Tokyo-Kyoto. JAPAN*, VolLVIII:333–338. [1.1.1](#)
- Bazan, E., Bazan-Arias, N. C., and Bielak, J. (1998). Three dimensional seismic response of building foundation systems. *Proceedings UJNR Workshop on Soil-Structure Interaction, Menlo Park, California*, September 22-23, 1998. [1.1.3](#)
- Beresnev, I. A., Field, E. H., Van Den Abeele, K., and Johnson, P. A. (1998). Magnitude of nonlinear sediment response in Los Angeles basin during the 1994 Northridge, California, earthquake. *Bulletin of the Seismological Society of America*, 88(4):1079–1084. [3.3.1](#), [5.3.1](#)
- Bielak, J. (1969). Base moment for a class of linear systems. *Journal of the Engineering Mechanics Division*, September/October 1969, Vol. 95, No. 5:pp. 1053–1062. [4.1.2](#)
- Bielak, J. (1971). *Earthquake response of building-foundation systems*. PhD thesis, Caltech. [1.1.1](#), [3.4.3](#)
- Bielak, J. (1975). Dynamic behaviour of structures with embedded foundations. *Earthquake Engineering & Structural Dynamics*, 3(3):259–274. [1.1.1](#)
- Bielak, J., Graves, R. W., Olsen, K. B., Taborda, R., Ramirez-Guzman, L., Day, S. M., Ely, G. P., Roten, D., Jordan, T. H., Maechling, P. J., Urbanic, J., Cui, Y., and Juve, G. (2010). The ShakeOut earthquake scenario: Verification of three simulation sets. *Geophysical Journal International*, 180(1):375–404. [2.2](#), [3.2](#)
- Bielak, J., Karaoglu, H., and Taborda, R. (2011). Memory-efficient displacement-based internal friction for wave propagation simulation. *Geophysics*, 76(6):T131–T145. [2.2](#)
- Bielak, J., Loukakis, K., Hisada, Y., and Yoshimura, C. (2003). Domain reduction method for three-dimensional earthquake modeling in localized regions, part i: Theory. *Bulletin of the Seismological Society of America*, 93(2):817–824. [1.2](#), [2](#), [2.3](#), [2.3](#)
- Bielak, J., Xu, J., and Ghattas, O. (1999). Earthquake ground motion and structural response in

- alluvial valleys. *Journal of Geotechnical and Geoenvironmental Engineering*, 125(5):413–423. [3.1](#), [5.1](#)
- Boutin, C. and Roussillon, P. (2004). Assessment of the urbanization effect on seismic response. *Bulletin of the Seismological Society of America*, 94(1):251–268. [1.1.2](#), [iii](#)
- Bouwkamp, J. G. and Blohm, J. K. (1966). Dynamic response of a two-story steel frame structure. *Bulletin of the Seismological Society of America*, 56(6):1289–1303. [1.1.3](#)
- Chandler, A. and Hutchinson, G. (1987). Parametric earthquake response of torsionally coupled buildings with foundation interaction. *Soil Dynamics and Earthquake Engineering*, 6(3):138 – 148. [1.1.3](#)
- Chandler, A. M. and Duan, X. N. (1991). Evaluation of factors influencing the inelastic seismic performance of torsionally asymmetric buildings. *Earthquake Engineering & Structural Dynamics*, 20(1):87–95. [1.1.3](#)
- Clough, R. W. and Penzien, J. (2003). *Dynamics of Structures - 3rd Edition*. Computers & Structures, Inc. [4.2](#)
- Clouteau, D. and Aubry, D. (2001). Modifications of the ground motion in dense urban areas. *Journal of Computational Acoustics*, 09(04):1659–1675. [1.1.2](#), [1.2](#), [3.4.3](#), [3.4.3](#), [iii](#)
- Crouse, C. B. and Jennings, P. C. (1975). Soil-structure interaction during the San Fernando earthquake. *Bulletin of the Seismological Society of America*, 65(1):13–36. [1.1.1](#)
- De Llera, J. C. L. and Chopra, A. K. (1995). Understanding the inelastic seismic behaviour of asymmetric-plan buildings. *Earthquake Engineering & Structural Dynamics*, 24(4):549–572. [1.1.3](#)
- Duke, C. M., Luco, J. E., Carriveau, A. R., Hradilek, P. J., Lastrico, R., and Ostrom, D. (1970). Strong earthquake motion and site conditions: Hollywood. *Bulletin of the Seismological Society of America*, 60(4):1271–1289. [3.4.3](#), [3.4.3](#)
- Fenves, G. L. and Serino, G. (1990). Soil-structure interaction in buildings from earthquake records. *Earthquake Spectra*, 6(4):641–655. [1.1.1](#)
- Fernandez-Ares, A. and Bielak, J. (2004). Interaction between earthquake ground motion and multiple buildings in urban regions. *Proceedings Third UJNR Workshop on Soil-Structure Interaction*, M. Celebi (USGS) M.I. Todorovska (USC), I. Okawa (BRI) and M. Iiba (NILIM) (editors), Menlo Park, California:1–11. [1.2](#), [2.3](#)
- Field, E. H., Johnson, P. A., Beresnev, I. A., and Zeng, Y. (1997). Nonlinear ground-motion amplification by sediments during the 1994 Northridge earthquake. *Nature*, 390(6660):599–602. [3.3.1](#), [5.3.1](#)
- Frankel, A. and Vidale, J. (1992). A three-dimensional simulation of seismic waves in the Santa Clara Valley, California, from a Loma Prieta aftershocks. *Bulletin of the Seismological Society of America*, 82(5):2045–2074. [2.2](#)
- Graves, R. W. (1996). Simulating seismic wave propagation in 3d elastic media using staggered-grid finite differences. *Bulletin of the Seismological Society of America*, 86(4):1091–1106. [2.2](#)
- Graves, R. W. and Pitarka, A. (2010). Broadband ground-motion simulation using a hybrid approach. *Bulletin of the Seismological Society of America*, 100(5A):2095–2123. [3.2](#), [3.1](#), [3.2](#), [5.2](#)
- Groby, J.-P., Tsogka, C., and Wirgin, A. (2005). Simulation of seismic response in a city-like environment. *Soil Dynamics and Earthquake Engineering*, 25:487 – 504. [1.1.2](#)
- Gueguen, P., Bard, P.-Y., and Chavez-Garcia, F. J. (2002). Site-city seismic interaction in Mexico City-like environments: An analytical study. *Bulletin of the Seismological Society of America*,

- 92(2):794–811. [1.1.2](#), [3.4.2](#)
- Gueguen, P., Bard, P.-Y., and Oliveira, C. S. (2000a). Experimental and numerical analysis of soil motions caused by free vibrations of a building model. *Bulletin of the Seismological Society of America*, 90(6):1464–1479. [1.1.1](#)
- Gueguen, P., Bard, P.-Y., and Semblat, J.-F. (2000b). From soil-structure interaction to site-city interaction. *Proceedings, 12th World Conf. Earthquake Eng.*, paper 0555, Auckland, New Zealand, 7 pp. [1.1.2](#)
- Hartzell, S., Leeds, A., Frankel, A., and Michael, J. (1996). Site response for urban Los Angeles using aftershocks of the Northridge earthquake. *Bulletin of the Seismological Society of America*, 86(1B):S168–S192. [3.3](#), [3.3.1](#)
- Hejal, R. (1987). *Earthquake response of torsionally buildings*. PhD thesis, University of California at Berkeley. [4.1.3](#), [i](#)
- Hejal, R. and Chopra, A. (1989). Earthquake response of torsionally coupled, frame buildings. *Journal of Structural Engineering*, 115(4):834–851. [1.1.3](#)
- Hoerner, J. B. (1971). *Modal coupling and earthquake response of tall buildings*. PhD thesis, California Institute of Technology. [1.1.3](#), [4.2](#), [4.2.2](#)
- Housner, G. W. (1957). Interaction of building and ground during an earthquake. *Bulletin of the Seismological Society of America*, 47(3):179–186. [1.1.1](#)
- Housner, G. W. and Outinen, H. (1958). The effect of torsional oscillations on earthquake stresses. *Bulletin of the Seismological Society of America*, 48(3):221–229. [1.1.3](#)
- Ishibashi, I. and Zhang, X. (1993). Unified dynamic shear moduli and damping ratios of sand and clay. *Soils and Foundations*, 33(1):182–191. [3.3.1](#)
- J.A. Santos, A. G. C. (2000). Shear modulus of soils under cyclic loading at small and medium strain level. *Proceedings, 12th World Conf. Earthquake Eng.*, paper 0530, Auckland, New Zealand, 8 pp. [3.3.1](#)
- Jennings, P. C. (1969). Spectrum techniques for tall buildings. *Proc. Fourth World Conf. Earthq. Eng.*, Vol 2 Section A-3:pp 61–74. [4.1.2](#)
- Jennings, P. C. (1970). Distant motions from a building vibration test. *Bulletin of the Seismological Society of America*, 60(6):2037–2043. [1.1.1](#)
- Jennings, P. C. and Bielak, J. (1973). Dynamics of building-soil interaction. *Bulletin of the Seismological Society of America*, 63(1):9–48. [1.1](#), [1.1.1](#), [3.4.3](#), [3.4.3](#), [3.4.3](#), [5.4.3](#)
- Jennings, P. C. and Kuroiwa, J. H. (1968). Vibration and soil-structure interaction tests of a nine-story reinforced concrete building. *Bulletin of the Seismological Society of America*, 58(3):891–916. [1.1.1](#)
- Jeremic, B., Jie, G., Preisig, M., and Tafazzoli, N. (2009). Time domain simulation of soil-foundation-structure interaction in non-uniform soils. *Earthquake Engineering & Structural Dynamics*, 38(5):699–718. [2.3](#)
- Kan, C. L. and Chopra, A. K. (1977). Elastic earthquake analysis of torsionally coupled multistorey buildings. *Earthquake Engineering & Structural Dynamics*, 5(4):395–412. [1.1.3](#)
- Kanamori, H., Mori, J., Anderson, D. L., and Heaton, T. H. (1991). Seismic excitation by the space shuttle Columbia. *Nature*, 349(6312):781–782. [1.1.1](#)
- Kausel, E. (2007). Comments on soil-structure interaction. *The 4th UJNR Workshop on Soil-Structure Interaction, Tsukuba Japan*, March 2007. [1.1](#)
- Kham, M., Semblat, J.-F., Bard, P.-Y., and Dangla, P. (2006). Seismic site-city interaction: Main governing phenomena through simplified numerical models. *Bulletin of the Seismological Society of America*, 96(2):451–461. [1.1.1](#)

- ety of America, 96(5):1934–1951. [1.1.2](#), [1.2](#), [3.1](#), [3.4.2](#), [iii](#), [4](#)
- Kuo, P. (1974). *Torsional effects in structures subjected to dynamic excitations of the ground*. PhD thesis, Rice University. [1.1.3](#), [4.2](#), [4.2.2](#)
- Lombaert, G. and Clouteau, D. (2006). Resonant multiple wave scattering in the seismic response of a city. *Waves in Random and Complex Media*, 16(3):205–230. [1.2](#), [3.4.3](#)
- Lombaert, G. and Clouteau, D. (2009). Elastodynamic wave scattering by finite-sized resonant scatterers at the surface of a horizontally layered halfspace. *The Journal of the Acoustical Society of America*, 125(4):2041–2052. [1.2](#)
- Lou, M., Wang, H., Chen, X., and Zhai, Y. (2011). Structure-soil-structure interaction: Literature review. *Soil Dynamics and Earthquake Engineering*, 31(12):1724 – 1731. [1.1](#), [1.1.1](#)
- Luco, J. E. (1969). Dynamic interaction of a shear wall with the soil. *Journal of the Engineering Mechanics Division*, March/April 1969 Vol. 95, No. 2:333–346. [1.1.1](#)
- Luco, J. E. (1976). Torsional response of structures to obliquely incident seismic SH waves. *Earthquake Engineering & Structural Dynamics*, 4(3):207–219. [1.1.3](#)
- Luco, J. E. and Contesse, L. (1973). Dynamic structure-soil-structure interaction. *Bulletin of the Seismological Society of America*, 63(4):1289–1303. [1.1.1](#), [3.4.3](#)
- Luco, J. E., Trifunac, M. D., and Wong, H. L. (1987). On the apparent change in dynamic behavior of a nine-story reinforced concrete building. *Bulletin of the Seismological Society of America*, 77(6):1961–1983. [3.4.3](#)
- Luco, J. E., Trifunac, M. D., and Wong, H. L. (1988). Isolation of soil-structure interaction effects by full-scale forced vibration tests. *Earthquake Engineering & Structural Dynamics*, 16(1):1–21. [1.1.1](#)
- Lysmer, J., Kuhlemeyer, R., of Transportation, I., Engineering, T., University of California, B. S. M., Laboratory, B. M. R., and University of California, B. G. E. G. (1969). *Finite Dynamic Model for Infinite Media*. Reprint (University of California). Department of Civil Engineering, University of California, Institute of Transportation and Traffic Engineering, Soil Mechanics Laboratory. [2.2](#)
- Magistrale, H., Day, S., Clayton, R. W., and Graves, R. (2000). The SCEC Southern California reference three-dimensional seismic velocity model version 2. *Bulletin of the Seismological Society of America*, 90(6B):S65–S76. [3.2](#)
- Magistrale, H., McLaughlin, K., and Day, S. (1996). A geology-based 3d velocity model of the Los Angeles basin sediments. *Bulletin of the Seismological Society of America*, 86(4):1161–1166. [3.2](#)
- Meremonte, M., Frankel, A., Cranswick, E., Carver, D., and Worley, D. (1996). Urban seismology-Northridge aftershocks recorded by multi-scale arrays of portable digital seismographs. *Bulletin of the Seismological Society of America*, 86(5):1350–1363. [3.3](#), [3.4.1](#)
- Merritt, R. G. and Housner, G. W. (1954). Effect of foundation compliance on earthquake stresses in multistory buildings. *Bulletin of the Seismological Society of America*, 44(4):551–569. [1.1.1](#)
- Miranda, E. and Reyes, C. (2002). Approximate lateral drift demands in multistory buildings with nonuniform stiffness. *Journal of Structural Engineering*, 128(7):840–849. [4.1.2](#)
- Newmark, N. M. (1969). Torsion in symmetrical buildings. *Fourth World Conference on Earthquake Engineering, Vol II, Santiago, Chile, 1969*, pages pp. A3–19 to A3–32. [1.1.3](#), [4](#), [4.2.2](#)
- Olsen, K., Day, S., Dalgner, L., Mayhew, J., Cui, Y., Zhu, J., Cruz-Atienza, V., Roten, D., Maechling, P., Jordan, T., et al. (2009). Shakeout-d: Ground motion estimates using an ensemble of large earthquakes on the southern San Andreas fault with spontaneous rupture propagation.

- Geophys. Res. Lett.*, 36(4):126. 2.2, 3.2
- Rosenblueth, E. and Meli, R. (1986). The 1985 earthquake: causes and effects in Mexico City. *Concrete International*, May 1986:23 – 35. 1.1.3
- Sadek, A. and Tso, W. (1989). Strength eccentricity concept for inelastic analysis of asymmetrical structures. *Engineering Structures*, 11(3):189 – 194. 1.1.3
- Semblat, J.-F., Kham, M., and Bard, P.-Y. (2008). Seismic-wave propagation in alluvial basins and influence of site-city interaction. *Bulletin of the Seismological Society of America*, 98(6):2665–2678. 1.1.2, 3.4.2, iii
- Shakib, H. and Fuladgar, A. (2004). Dynamic soil-structure interaction effects on the seismic response of asymmetric buildings. *Soil Dynamics and Earthquake Engineering*, 24(5):379 – 388. 1.1.3
- Shepherd, R. and Donald, R. (1967). Seismic response of torsionally unbalanced buildings. *Journal of Sound and Vibration*, 6(1):20 – 37. 1.1.3
- Sivakumaran, K., Lin, M.-S., and Karasudhi, P. (1992). Seismic analysis of asymmetric building-foundation systems. *Computers & Structures*, 43(6):1091 – 1103. 1.1.3
- Stewart, J., Seed, R., and Fenves, G. (1999). Seismic soil-structure interaction in buildings. ii: Empirical findings. *Journal of Geotechnical and Geoenvironmental Engineering*, 125(1):38–48. 1.1.1, i
- Taborda, R. (2010). *Three dimensional nonlinear soil and site-city effects in urban regions*. PhD thesis, Carnegie Mellon University, Pittsburgh, PA, USA. AAI3438461. 1.2, 2, 2.2, 2.1, 2.2.1, 3, 4, 4.1.1
- Taborda, R. and Bielak, J. (2011a). Full 3d integration of site-city effects in regional scale earthquake simulations. *Proceedings of the 8th International Conference on Structural Dynamics, EURODYN*, G. De Roeck, G. Degrande, G. Lombaert, G. Muller (eds.):511–518. 1.2, 3, 3.3, 4
- Taborda, R. and Bielak, J. (2011b). Large-scale earthquake simulation: Computational seismology and complex engineering systems. *Computing in Science Engineering*, 13(4):14–27. 1.2, 3, 3.3, 4
- Taborda, R. and Bielak, J. (2013). Ground-motion simulation and validation of the 2008 Chino Hills, California, earthquake. *Bulletin of the Seismological Society of America*, 103(1):131–156. 2.2, 3.2
- Taborda, R., Karaoglu, H., Lopez, J., Urbanic, J., and Bielak, J. (2010). Speeding up finite element wave propagation for large-scale earthquake simulations. *Technical Report CMU-PDL-10-109*, Carnegie Mellon University, Parallel Data Lab:23 pp. 2.2.1
- Tezcan, S. S. and Alhan, C. (2001). Parametric analysis of irregular structures under seismic loading according to the new Turkish earthquake code. *Engineering Structures*, 23(6):600 – 609. 1.1.3
- Trifunac, M. and Todorovska, M. (1996). Nonlinear soil response-1994 Northridge, California, earthquake. *Journal of geotechnical engineering*, 122(9):725–735. 3.3.1, 5.3.1
- Trifunac, M., Todorovska, M., and Ivanovic, S. (1996). Peak velocities and peak surface strains during Northridge, California, earthquake of 17 January 1994. *Soil Dynamics and Earthquake Engineering*, 15(5):301 – 310. 3.3.1
- Trifunac, M., Todorovska, M. I., and Hao, T.-Y. (2001). Full scale experimental studies of soil-structure interaction - a review. *The 2nd UJNR Workshop on Soil-Structure Interaction, Tsukuba Japan*, March 6 to 8, 2001. 1.1.1, 3.4.3, A.1, A.2
- Trifunac, M. D., Todorovska, M. I., and Lee, V. W. (1998). The Rinaldi strong motion ac-

- celerogram of the Northridge, California earthquake of 17 January 1994. *Earthquake Spectra*, 14(1):225–239. [3.4.1](#)
- Tsionas, T. G. and Hutchinson, G. L. (1984). Soil-structure interaction effects on the steady-state response of torsionally coupled buildings. *Earthquake Engineering & Structural Dynamics*, 12(2):237–262. [1.1.3](#)
- Tso, W. K. and Dempsey, K. M. (1980). Seismic torsional provisions for dynamic eccentricity. *Earthquake Engineering & Structural Dynamics*, 8(3):275–289. [1.1.3](#), [4.2](#), [4.2.2](#)
- Tsogka, C. and Wirgin, A. (2003). Simulation of seismic response in an idealized city. *Soil Dynamics and Earthquake Engineering*, 23(5):391 – 402. [1.1.2](#), [3.1](#), [4](#)
- Tu, T., Yu, H., Ramirez-Guzman, L., Bielak, J., Ghattas, O., Ma, K.-L., and O’Hallaron, D. R. (2006). From mesh generation to scientific visualization: An end-to-end approach to parallel supercomputing. In *SC 2006 Conference, Proceedings of the ACM/IEEE*, page 12. [2](#), [2.2](#), [2.2](#)
- Veletsos, A. S. and Meek, J. W. (1974). Dynamic behaviour of building-foundation systems. *Earthquake Engineering & Structural Dynamics*, 3(2):121–138. [1.1](#), [1.1.1](#), [3.4.3](#), [5.4.3](#)
- Wirgin, A. and Bard, P.-Y. (1996). Effects of buildings on the duration and amplitude of ground motion in Mexico city. *Bulletin of the Seismological Society of America*, 86(3):914–920. [1.1](#), [1.1.1](#), [1.1.2](#), [3.1](#), [4](#)
- Wong, H. L. and Trifunac, M. D. (1975). Two-dimensional, antiplane, building-soil-building interaction for two or more buildings and for incident plane SH waves. *Bulletin of the Seismological Society of America*, 65(6):1863–1885. [1.1.1](#)
- Wu, W.-H., Wang, J.-F., and Lin, C.-C. (2001). Systematic assessment of irregular building-soil interaction using efficient modal analysis. *Earthquake Engineering & Structural Dynamics*, 30(4):573–594. [1.1.3](#)
- Yoshimura, C., Bielak, J., Hisada, Y., and Fernandez, A. (2003). Domain reduction method for three-dimensional earthquake modeling in localized regions, part ii: Verification and applications. *Bulletin of the Seismological Society of America*, 93(2):825–841. [2.3](#)

APPENDIX A

Hollywood Storage Building

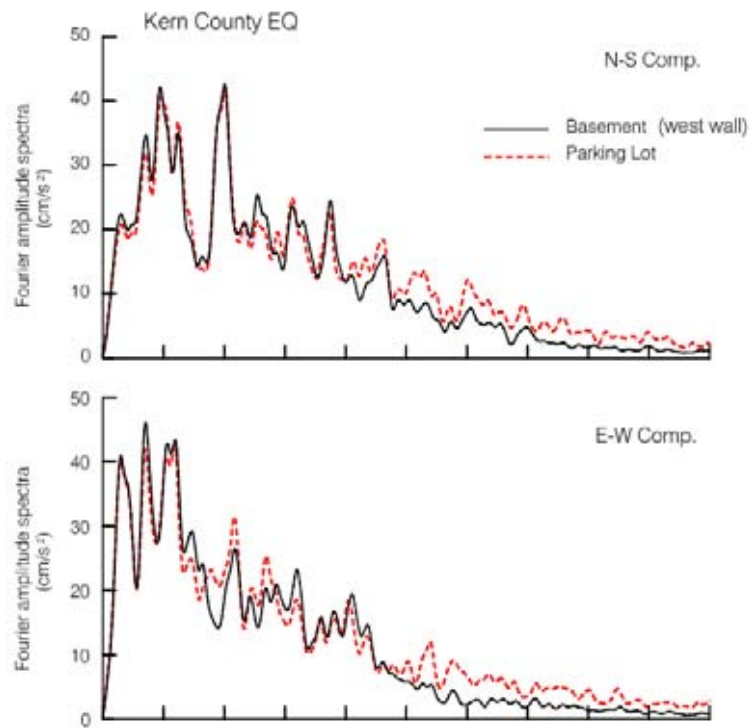


Figure A.1: Comparison of the Fourier amplitude spectra for the Hollywood Storage Building between the base and the free-field motions during the Kern County Earthquake, after [Trifunac et al. \(2001\)](#).

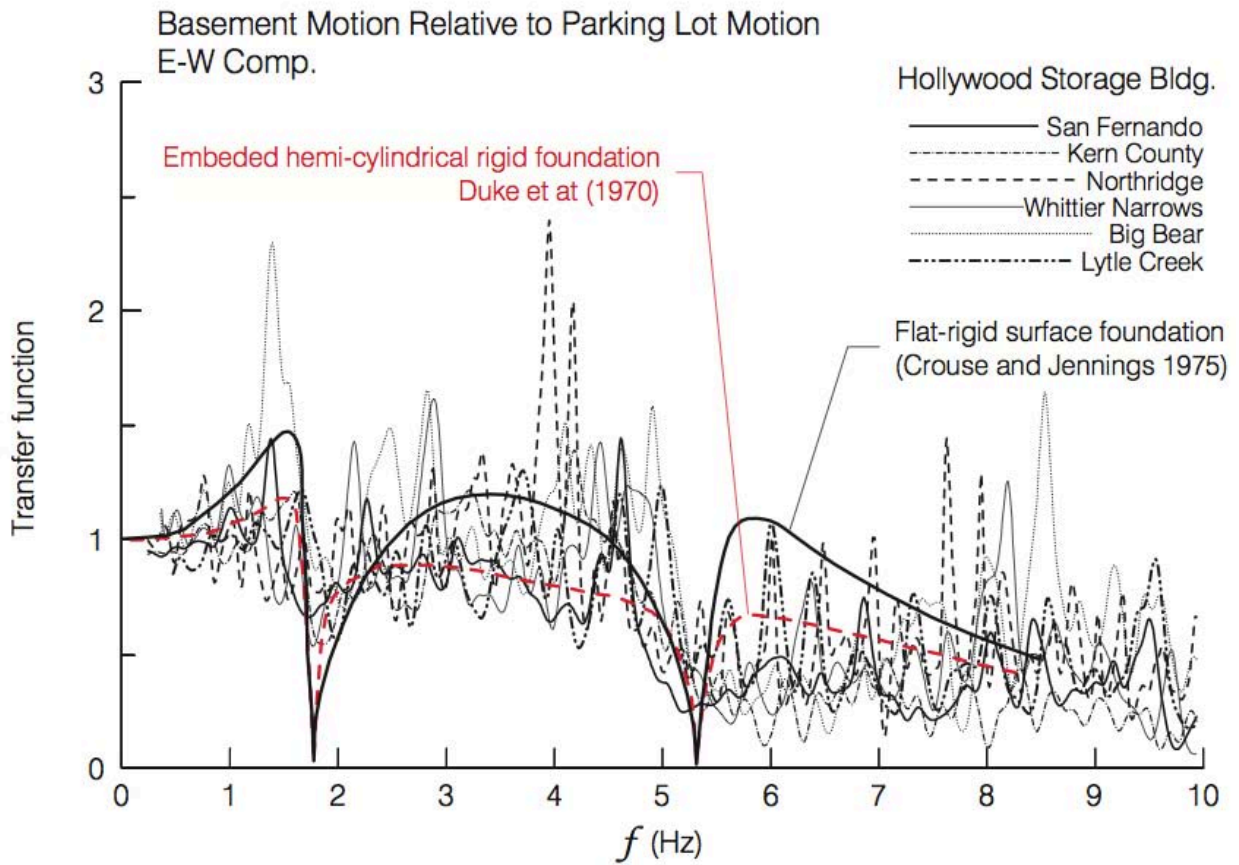


Figure A.2: Transfer functions between the motion recorded at the base of the Hollywood Storage Building and the "free field" motion recorded in the parking lot during six earthquakes. The black continuous line and the red dash line correspond to the theoretical curves, after [Trifunac et al. \(2001\)](#).

APPENDIX B

Computational Effort and Performance

- Case I

Simulations were run in Kraken at the U.S. National Institute for Computational Sciences. Kraken is a Cray XT5 supercomputer with 112,896 cores distributed on 9,408 compute nodes. For these simulations I used only a fraction of the total available cores. By using the DRM I obtain a substantial reduction in the computational cost (service units) from Step I to Step II, even for the case of softened soil conditions, which is more demanding than the original model since the lower shear wave velocities require a finer FE mesh. In total, performing the simulations required for the 60 variations in Step II was still much less expensive than the original regional simulation, even though the local area I selected is $5.12 \text{ km} \times 5.12 \text{ km}$, which is significantly larger than what was needed just for the cluster arrangements considered here. Other details related to the computational effort and performance are included in Table [B.1](#).

Table B.1: Simulation domain characteristics and properties for case I, and simulation performance for the DRM steps I and II for both the soft and hard soil cases. All simulations were run in Kraken, the Cray XT5 parallel supercomputer at the National Institute for Computational Science.

Analytics	Step I	Step II	Step II
		Original Model	Softened Model
Max. Frequency (Hz)	5	5	5
Min. Vs (m/s)	200	200	100
Number of Buildings	0	up to 81	up to 81
Domain Size (km ³)	81.92×81.92×40.96	5.12×5.12×1.28	5.12×5.12×1.28
Number of Elements	2.5 billion	11 million	23 million
Number of Cores	18,000	960	960
Total Simulation Time	15 hrs 2 min	49 min	1 hr 22 min
Service Units / Sim.	270,600	784	1,312
Number of Simulations	1	30	30
Total Service Units	270,600	23,520	39,360

APPENDIX C

Computational Effort and Performance

- Case II

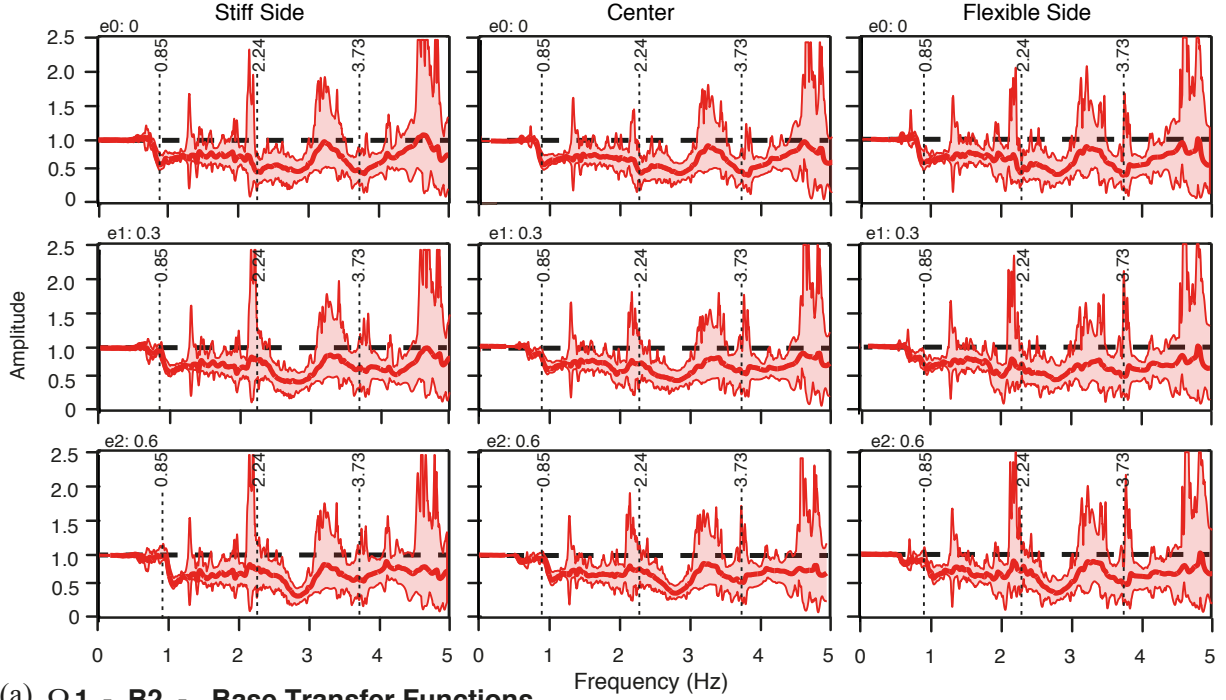
For the second case study, local area is selected as $1.28 \text{ km} \times 1.28 \text{ km}$. This is much smaller than the area considered in the first study, thus helps decreasing the total service units in the step II simulations. On the other hand, calculating the constrained displacements in the buildings entails knowing the displacements of all the nodes at any given level. For this, MPI communications are established between processors to calculate and update the constrained displacement values at each time step. Also note that, the constrained building models are composed of the same sized elements (see Chapter 4) which are generally the smallest in the simulation domain (this may also necessitate to decrease the time step). These two factors, in turn, increase the total number of elements and also the total simulation time. Other details related to the computational effort and performance are included in Table C.1.

Table C.1: Simulation domain characteristics and properties for case II, and simulation performance for the DRM steps I and II for both the soft and hard soil cases. All simulations were run in Kraken, the Cray XT5 parallel supercomputer at the National Institute for Computational Science.

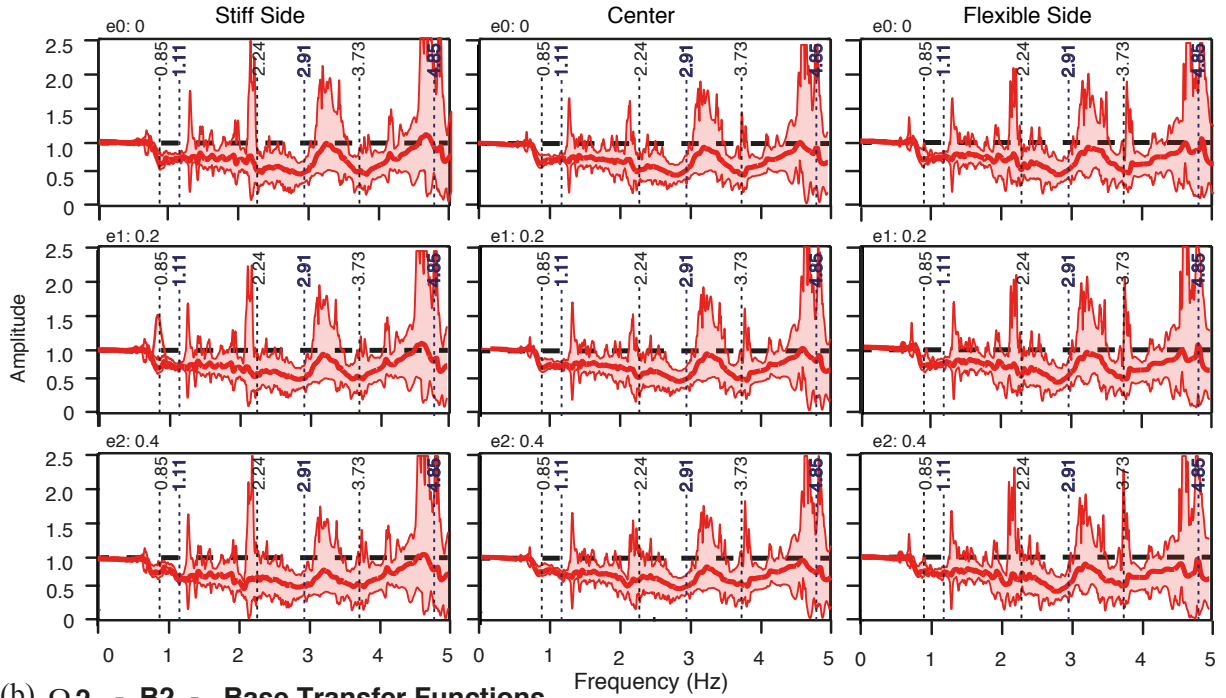
Analytics	Step I	Step II	Step II
		Original Model	Softened Model
Max. Frequency (Hz)	5	5	5
Min. Vs (m/s)	100	100	100
Number of Buildings	0	up to 49	up to 49
Domain Size (km ³)	81.92×81.92×40.96	1.28×1.28×0.64	1.28×1.28×0.64
Number of Elements	2.7 billion	2.6 million	2.9 million
Number of Cores	20,400	480	480
Total Simulation Time	14 hrs 12 min	2 hr 10 min	2 hr 20 min
Service Units / Sim.	290,000	1,040	1,120
Number of Simulations	1	91	91
Total Service Units	290,000	94,640	101,920

APPENDIX D

Additional Figures for Case II

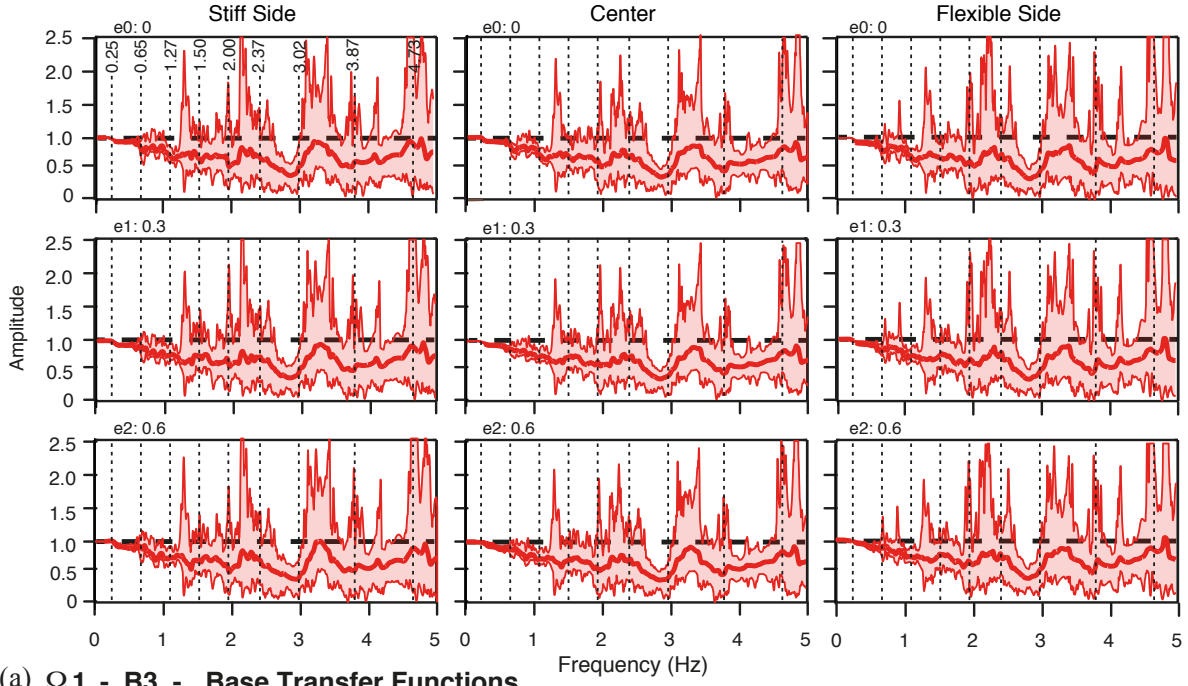


(a) Ω_1 - B2 - Base Transfer Functions

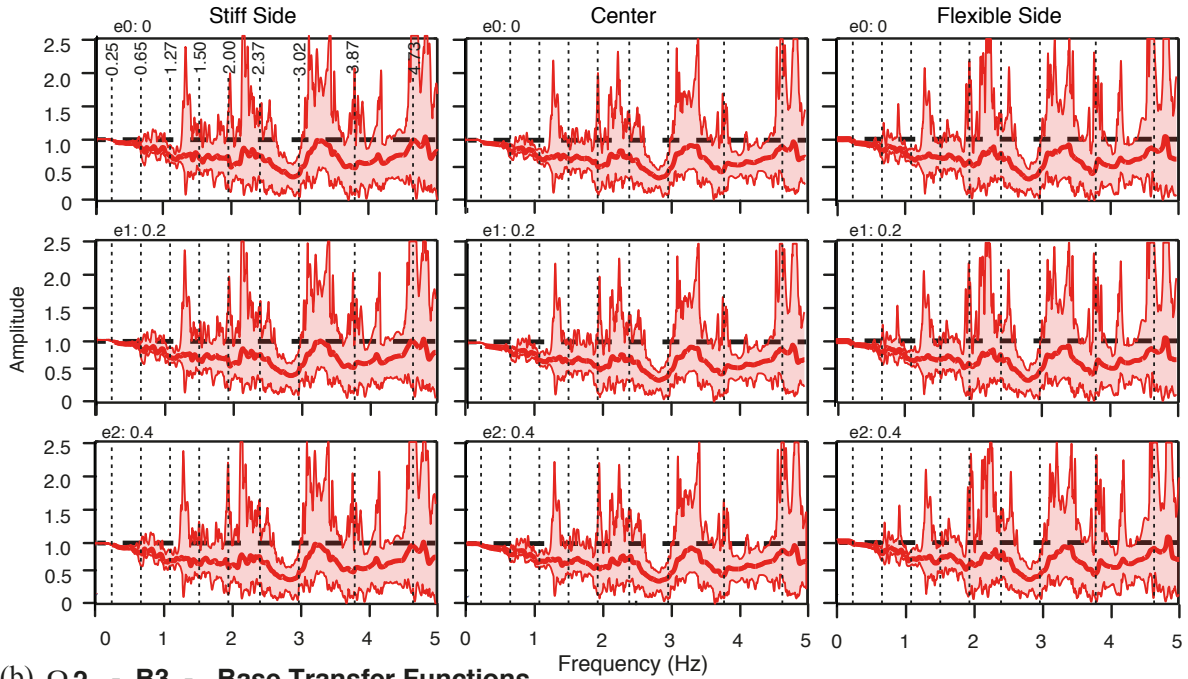


(b) Ω_2 - B2 - Base Transfer Functions

Figure D.1: Average (thick lines) and maximum and minimum envelopes (thin lines) of the transfer functions between the base and the free-field motions for all the B2 type of buildings with different e_s and Ω_s in the various cluster and spacing arrangements in the EW direction. Only results for the softened soil conditions are presented. Filled areas cover the range from the minimum to the maximum envelopes. The black dashed line indicates the case of no interaction. In each frame, the vertical dotted lines mark the uncoupled translational and torsional (bold lines) frequencies of vibration.

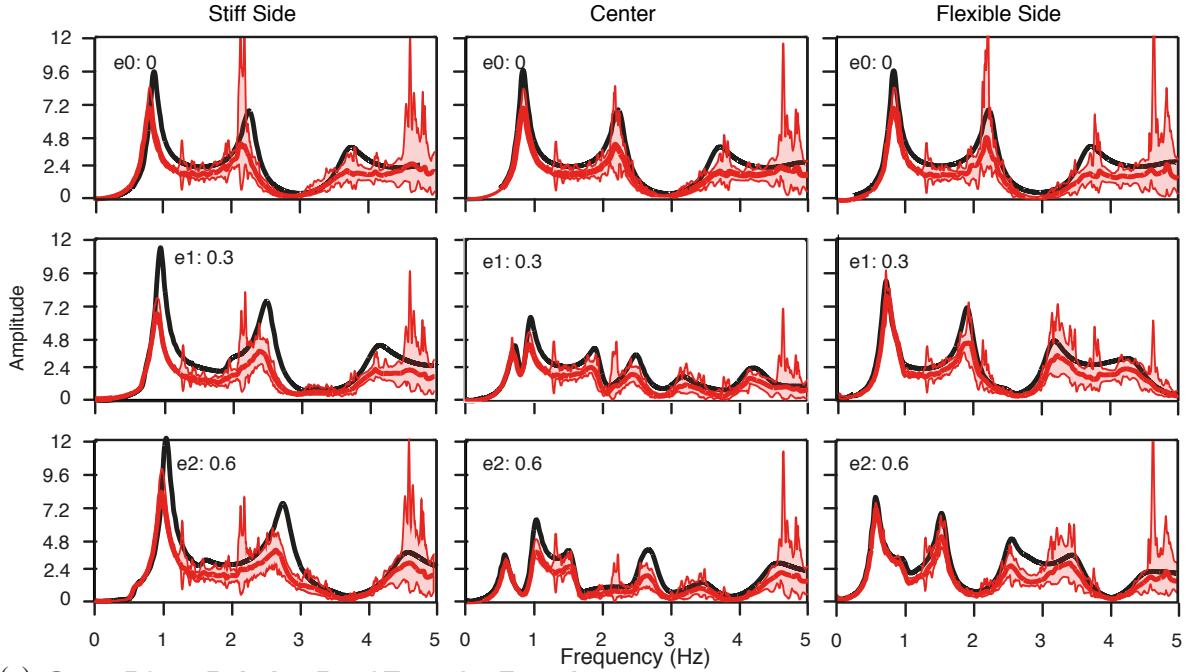


(a) Ω_1 - B3 - Base Transfer Functions

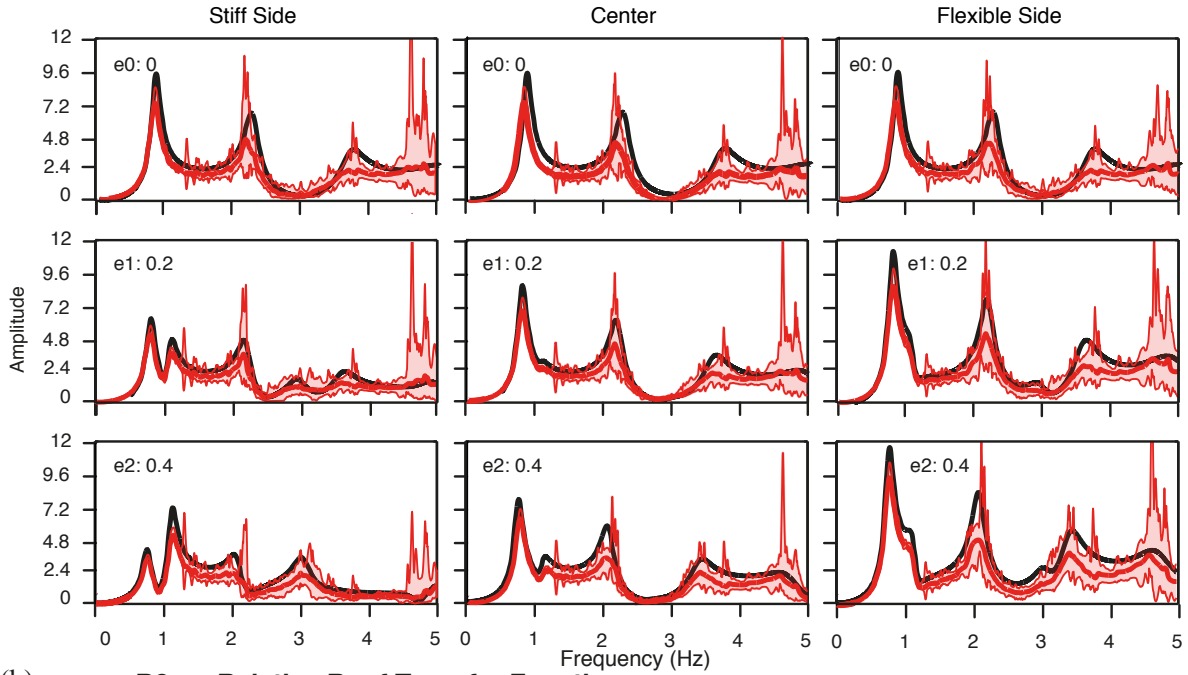


(b) Ω_2 - B3 - Base Transfer Functions

Figure D.2: Average (thick lines) and maximum and minimum envelopes (thin lines) of the transfer functions between the base and the free-field motions for all the B3 type of buildings with different e_s and Ω_s in the various cluster and spacing arrangements in the EW direction. Only results for the softened soil conditions are presented. Filled areas cover the range from the minimum to the maximum envelopes. The black dashed line indicates the case of no interaction. In each frame, the vertical dotted lines mark the uncoupled translational frequencies of vibration.

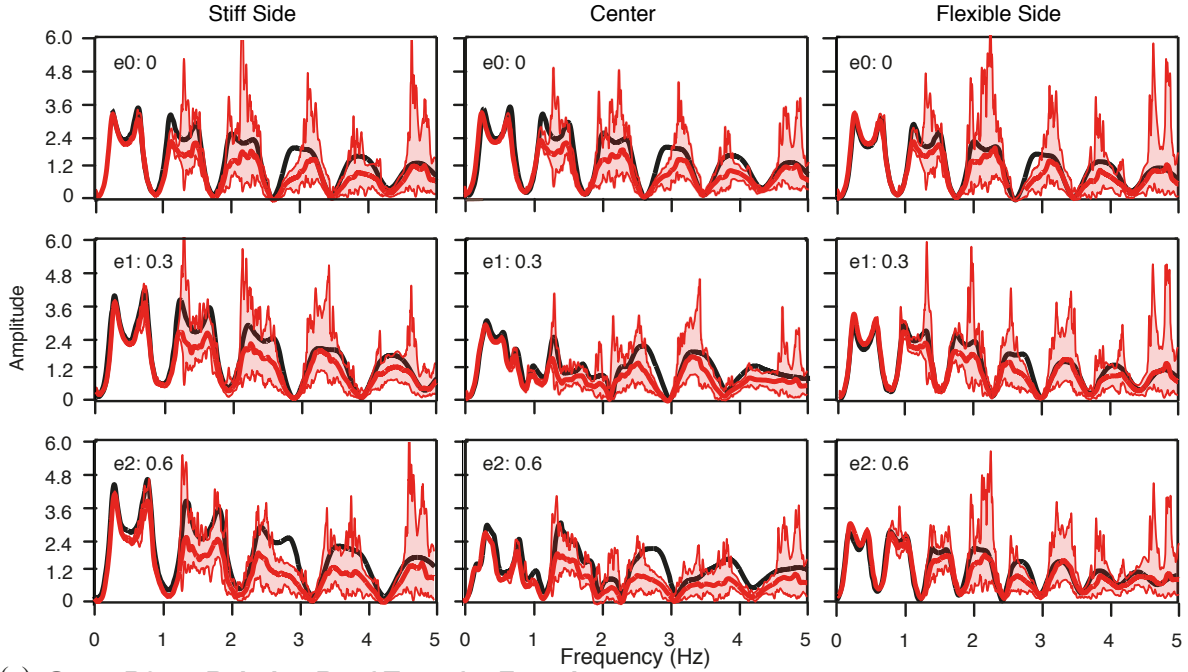


(a) $\Omega 1$ - B2 - Relative Roof Transfer Functions

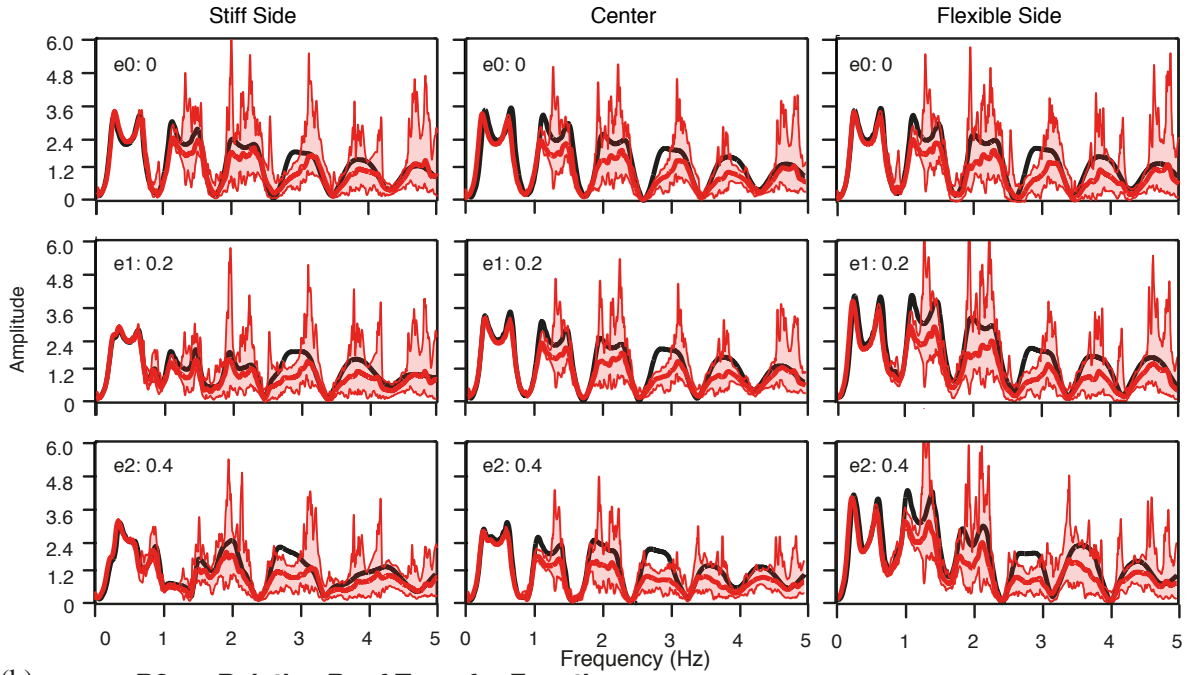


(b) $\Omega 2$ - B2 - Relative Roof Transfer Functions

Figure D.3: Same as Figure D.1 but for the transfer functions between the relative roof and the free-field motions. Here, the black lines correspond to the transfer functions of the rigid-base models.

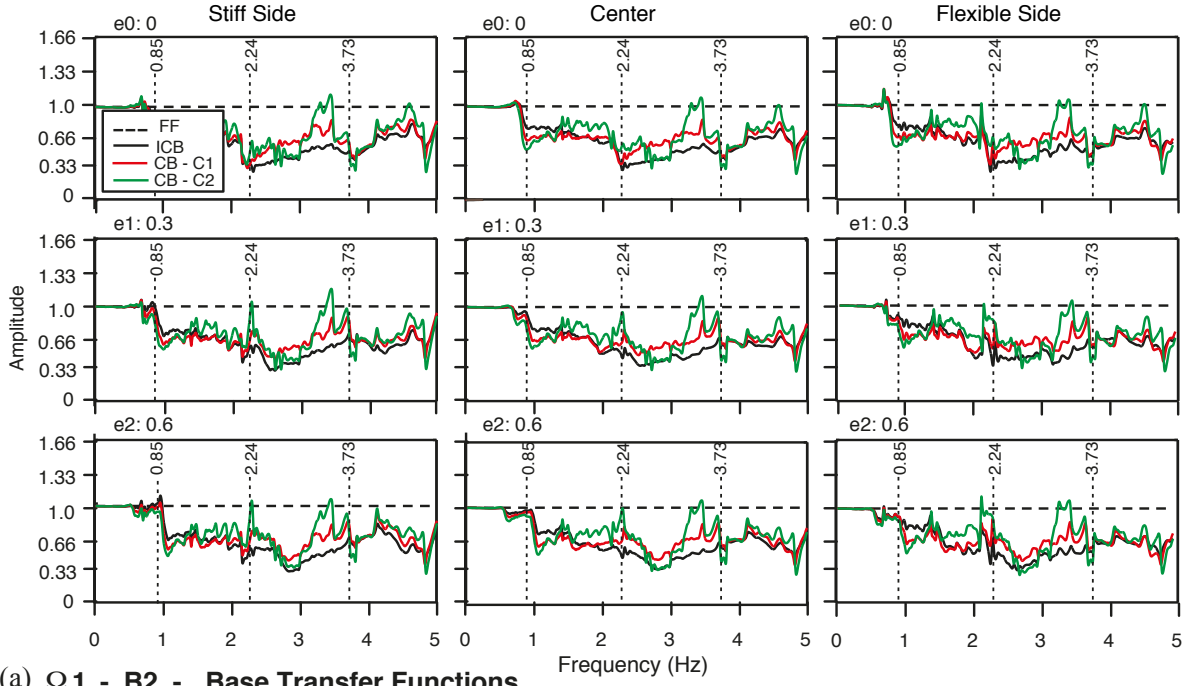


(a) Ω_1 - B3 - Relative Roof Transfer Functions

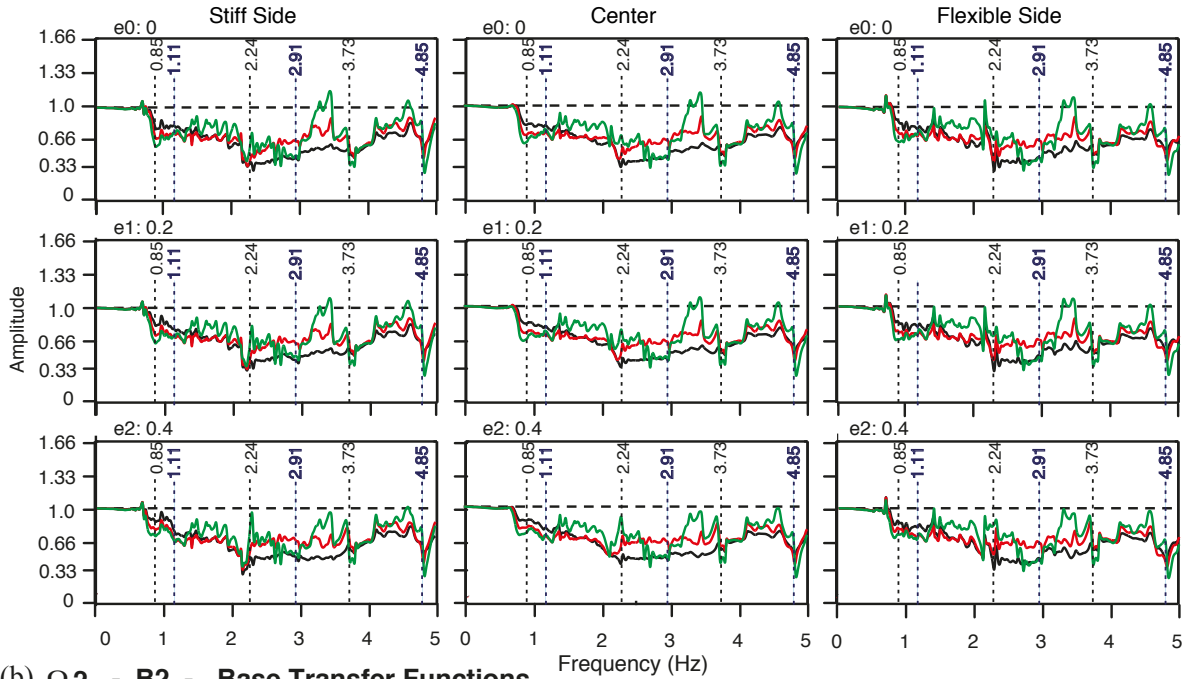


(b) Ω_2 - B3 - Relative Roof Transfer Functions

Figure D.4: Same as Figure D.2 but for the transfer functions between the relative roof and the free-field motions. Here, the black lines correspond to the transfer functions of the rigid-base models.

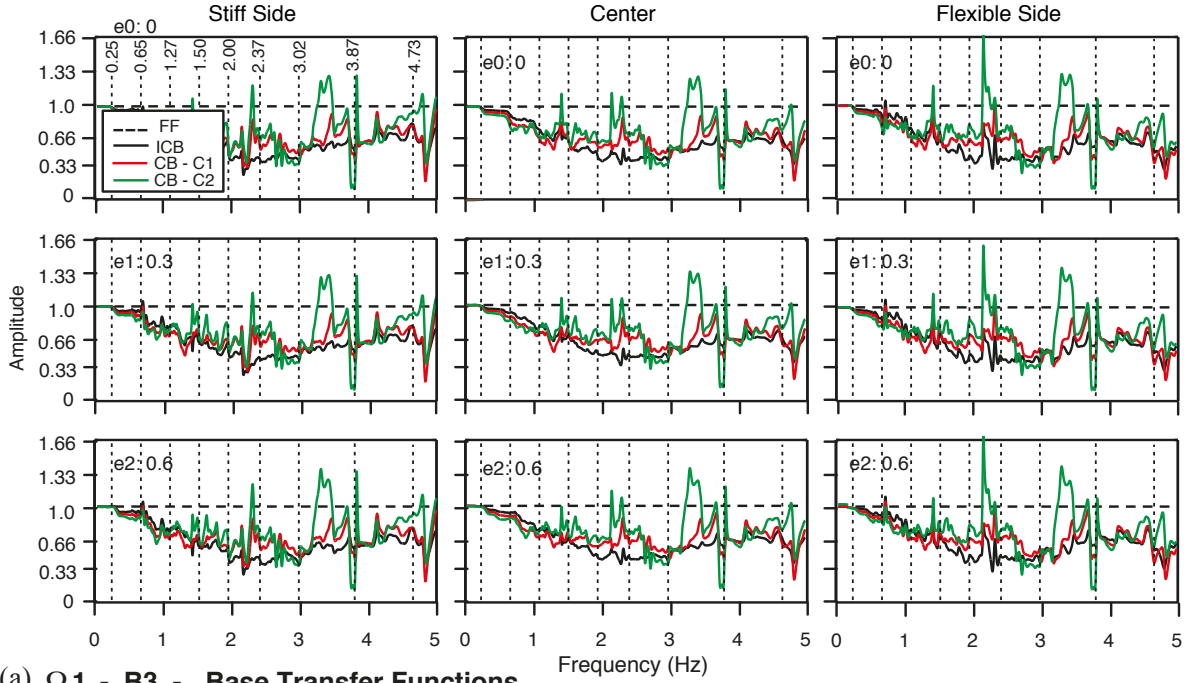


(a) $\Omega 1$ - B2 - Base Transfer Functions

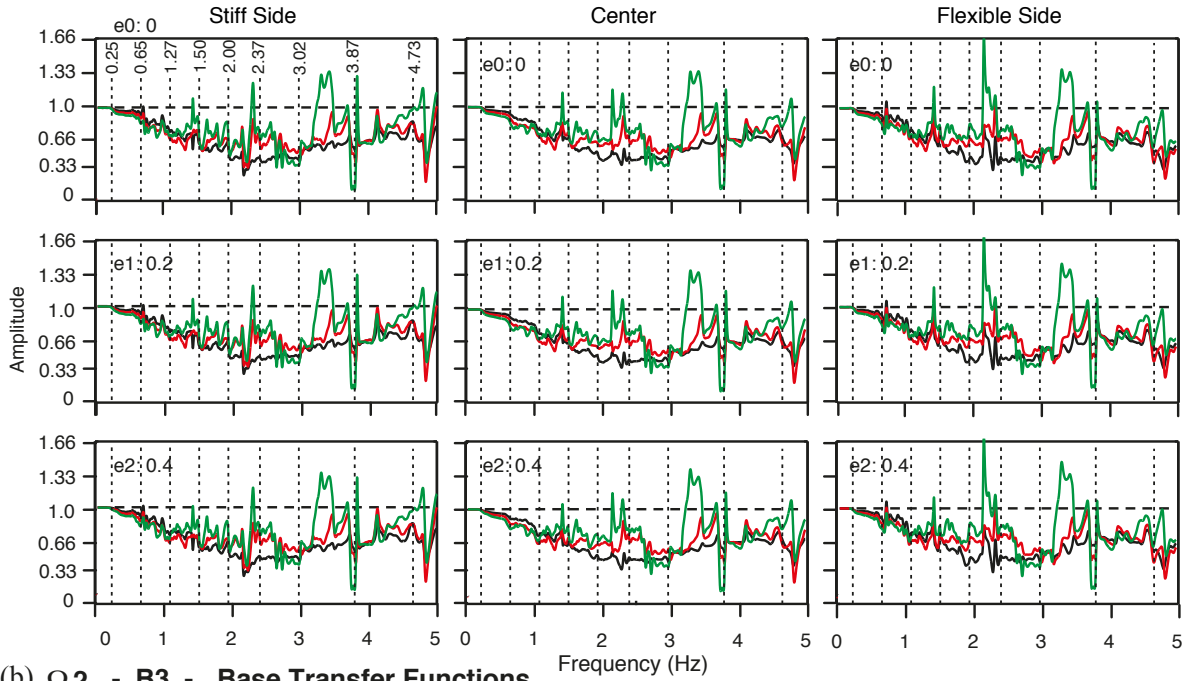


(b) $\Omega 2$ - B2 - Base Transfer Functions

Figure D.5: Comparisons between the base transfer function of the isolated control building (ICB) (black) and the various transfer functions corresponding to the same building at the center of each cluster (CB) for the arrangements C1 (red) and C2 (green) for the B2-S1 type of structures with different e and Ω values. The horizontal dashed line indicates no change with respect to the free-field motion. These results correspond to the motion in the EW direction and to the softened soil system and are given at three points in the structure located; on the stiff side (left), at the center (middle), on the flexible side (right). In each frame, the vertical dotted lines mark the uncoupled translational and torsional (bold lines) frequencies of vibration.

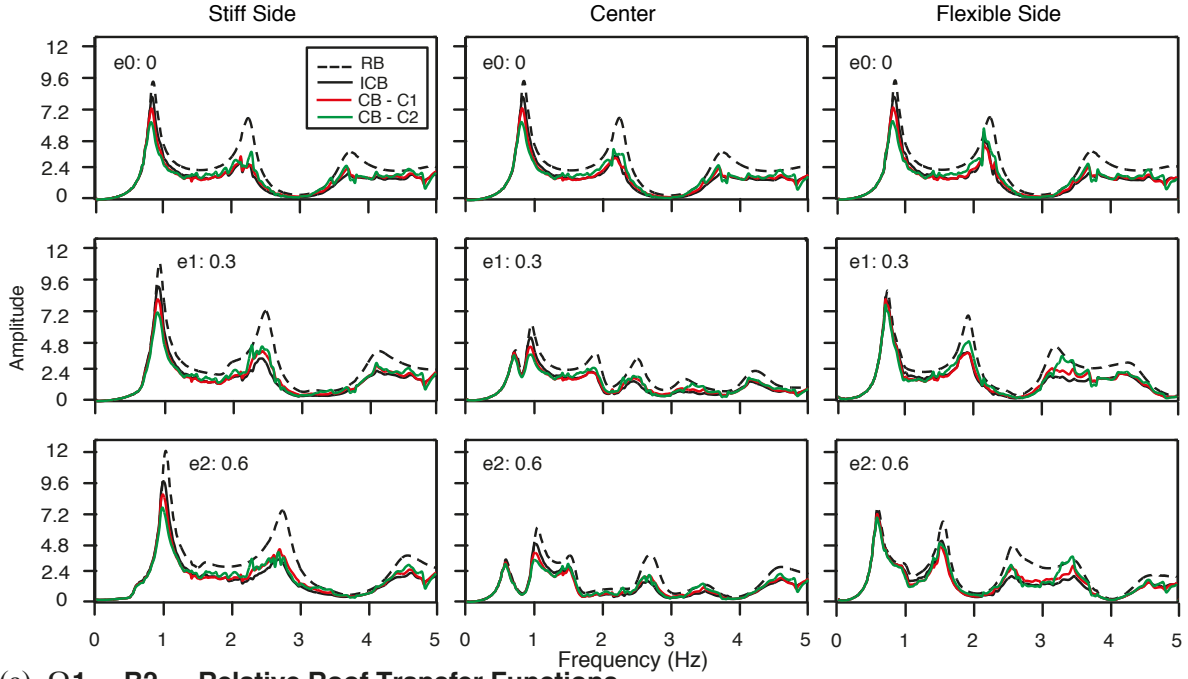


(a) $\Omega 1$ - B3 - Base Transfer Functions

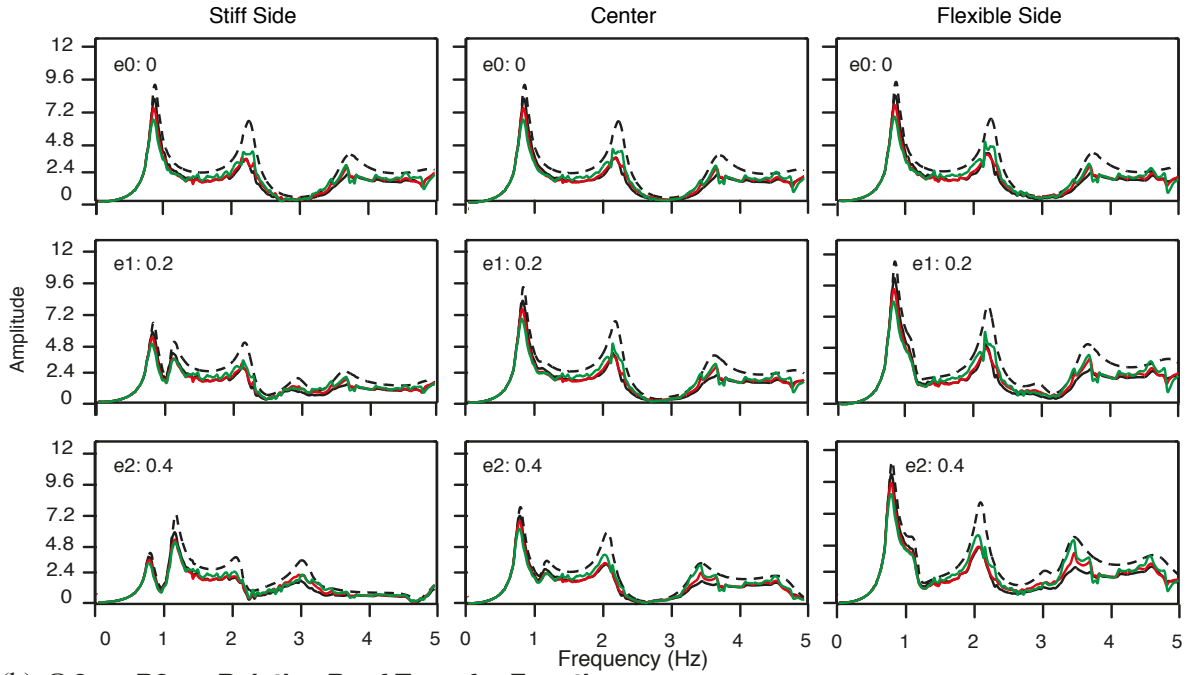


(b) $\Omega 2$ - B3 - Base Transfer Functions

Figure D.6: Comparisons between the base transfer function of the isolated control building (ICB) (black) and the various transfer functions corresponding to the same building at the center of each cluster (CB) for the arrangements C1 (red) and C2 (green) for the B3-S1 type of structures with different e and Ω values. The horizontal dashed line indicates no change with respect to the free-field motion. These results correspond to the motion in the EW direction and to the softened soil system and are given at three points in the structure located; on the stiff side (left), at the center (middle), on the flexible side (right). In each frame, the vertical dotted lines mark the uncoupled translational frequencies of vibration.

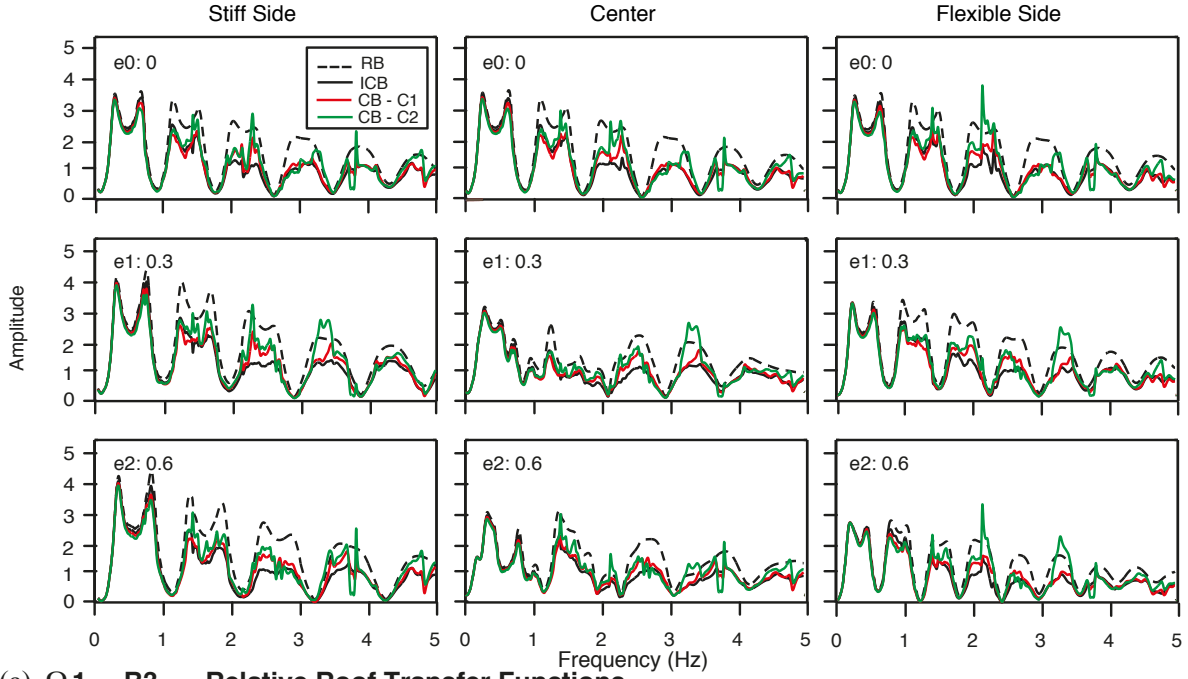


(a) Ω_1 - B2 - Relative Roof Transfer Functions

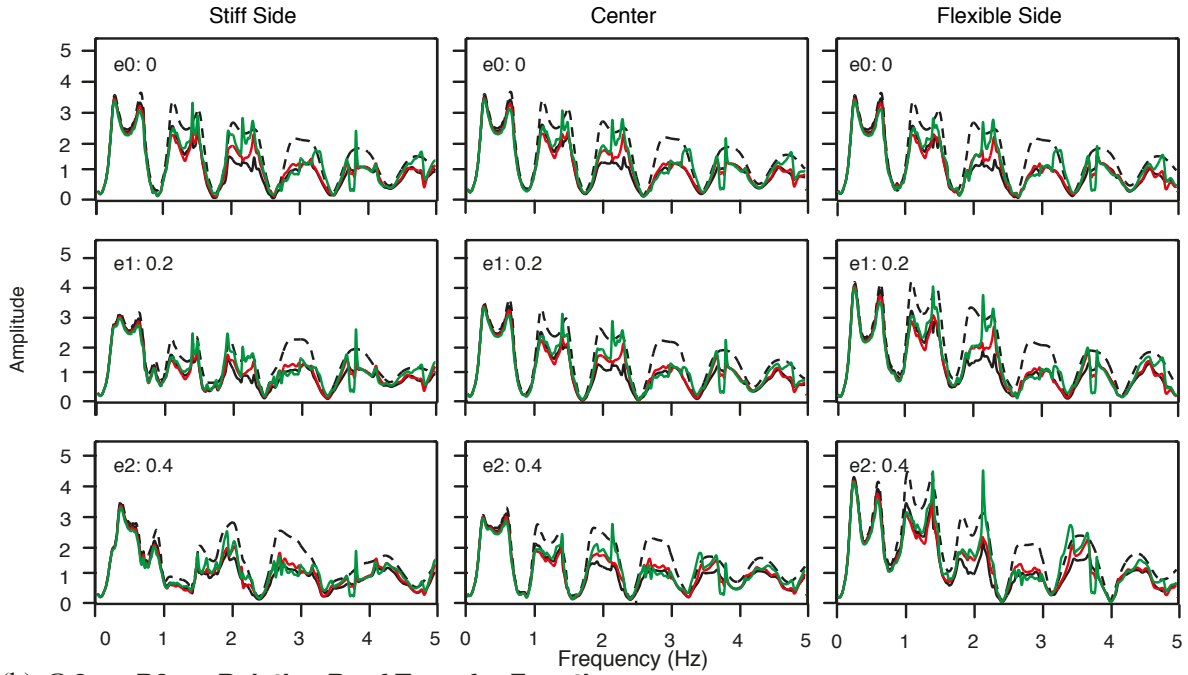


(b) Ω_2 - B2 - Relative Roof Transfer Functions

Figure D.7: Comparisons between the system's relative roof transfer function (with respect to the free-field) of the isolated control building (ICB) (black) and the various transfer functions corresponding to the same building at the center of each cluster (CB) for the arrangements, C1 (red) and C2 (green) or the B2-S1 type of structures with different e and Ω values. The dashed line corresponds to the relative roof transfer function of the rigid-base (RB) system. These results correspond to the motion in the EW direction and to the softened soil system and are given at three points in the structure located; on the stiff side (left), at the center (middle), on the flexible side (right).



(a) $\Omega 1$ - B3 - Relative Roof Transfer Functions



(b) $\Omega 2$ - B3 - Relative Roof Transfer Functions

Figure D.8: Comparisons between the system's relative roof transfer function (with respect to the free-field) of the isolated control building (ICB) (black) and the various transfer functions corresponding to the same building at the center of each cluster (CB) for the arrangements, C1 (red) and C2 (green) or the B3-S1 type of structures with different e and Ω values. The dashed line corresponds to the relative roof transfer function of the rigid-base (RB) system. These results correspond to the motion in the EW direction and to the softened soil system and are given at three points in the structure located; on the stiff side (left), at the center (middle), on the flexible side (right).